Mechanical properties and oxidation behavior of micro-alloyed iron aluminides

Zur Erlangung des akademischen Grades

Doktor der Ingenieurwissenschaften

der Fakultät für Maschinenbau

Karlsruher Institut für Technologie (KIT)

genehmigte

Dissertation

von

Dipl.-Ing. Daniel Janda

Tag der mündlichen Prüfung: 18.02.2015

Hauptreferent: Prof. Dr. Martin Heilmaier

Korreferent: Prof. Dr. Sharvan K. Kumar

Zusammenfassung

Die Arbeiten zu dieser Dissertation fanden im Rahmen eines durch das Bundesministerium für Wirtschaft und Technologie (BMWi) geförderten Verbundvorhabens statt, dessen Ziel es war abzuschätzen, ob Eisenaluminide als Konstruktionswerkstoffe im Hinblick auf Abgasturbolader mit variabler Turbinengeometrie in Ottomotoren eingesetzt werden können. Die hier gezeigten Untersuchungen beschäftigen sich mit den rein materialwissenschaftlichen Aspekten dieses Projektes. Eisenaluminid-Legierungen haben aufgrund ihrer hervorragenden Oxidationsbeständigkeit, niedrigen Rohmaterialkosten, geringen Dichte und für intermetallische Legierungen guten Verarbeitbarkeit ein hohes Potential, um aktuell verwendete Werkstoffe in Turboladern zu substituieren.

Es wurden drei mikrolegierte FeAl Guss-Legierungen mit 27, 33 und 39 at.% Aluminium bezüglich ihres Oxidationsverhaltens und ihrer mechanischen Eigenschaften untersucht. Um eine möglichst gute Vergleichbarkeit der jeweiligen Legierungen zu erreichen, wurden die Mikrolegierungselemente (Niob, Zirkon, Kohlenstoff und Bor) in identischen Konzentrationen hinzulegiert. Die Randbedingungen der jeweiligen Messungen (wie z.B. Oxidationstemperaturen) wurden weitgehend von den Projektpartnern vorgegeben. Es wurden zahlreiche Untersuchungen durchgeführt und Materialkennwerte ermittelt, die den Projektpartnern zur Verfügung gestellt wurden. Die aus wissenschaftlicher Sicht drei interessantesten Aspekte, die im Folgendem genannt werden, bilden neben der mikrostrukturellen Charakterisierung der Legierungen die Grundlage dieser Arbeit: Oxidationsverhalten, Plastizität bei Raumtemperatur als Funktion der Dehnrate und Kriechverhalten wurden detailliert untersucht. Das Oxidationsverhalten wurde unter zyklischer Belastung in einem Temperaturbereich von 750 – 1050 °C charakterisiert. Die mechanischen Eigenschaften wurden bei Raumtemperatur als Funktion der Dehnrate im Bereich von 10^{-4} – 10^{3} s^{-1} und in Kriechexperimenten in einem Temperaturbereich von 625 – 700 °C untersucht.

Die bereits bekannte hervorragende Oxidationsbeständigkeit von Eisenaluminiden konnte bestätigt und sogar weiter optimiert werden. Es zeigte sich, dass im FeAl-Mischkristall gelöstes Niob das Auftreten der besonders schützenden α-Al_2O_3 Deckschicht bei 900 °C hin zu niedrigen Oxidationstemperaturen von 750 °C stabilisieren konnte. Mikrolegierungselemente, die in Ausscheidungen im Gefüge vorlagen, verschlechterten hingegen die Oxidationsbeständigkeit, da hier die innere Oxidation katalytisch begünstigt wurde.

Das dehnratenabhängige Verformungsverhalten bei Raumtemperatur wurde insbesondere von der Kristallstruktur der FeAl Matrix bestimmt. Bei der $D0_3$ geordneten Fe-27Al Legierung kam es bei hohen Dehnraten ($\geq 10^3$ s^{-1}) zur Aktivierung von Verformungsmechanismen wie Zwillingsbildung und Scherlokalisation, deren Strukturen und Eigenschaften charakterisiert wurden. Bei niedrigen Dehnraten ($\leq 10^{-1}$ s^{-1}) war bei keiner der Legierungen ein Einfluss der Dehnrate auf die mechanischen Eigenschaften zu beobachten. Erst ab Dehnraten von $\leq 10^2$ s^{-1} war kam es zu einer signifikanten Erhöhung der Streckgrenze.

Das Kriechverhalten der Legierungen zeigte unerwartete Aspekte auf. Bevor sich eine stationäre Kriechrate einstellte, war ein ausgeprägter Bereich mit einer sehr viel geringeren Kriechrate zu beobachten. Der Übergang von dieser minimalen Kriechrate hin zur stationären Kriechrate war begleitet von einer Abnahme der Mischkristallhärtung der FeAl-Matrix. Dies ging einher mit der Ausscheidung von relativ großen und ungleichmäßig verteilten Ausscheidungen, deren Einfluss auf die Festigkeit allerdings vernachlässigbar war. Zusätzlich kam es bei der bei Raumtemperatur $D0_3$ geordneten Fe-27Al Legierung zu einer weiteren Entfestigung durch die Umwandlung von $D0_3$ in B2 geordnete Domänen.

Abschließend lässt sich zusammenfassen, dass die durchgeführten Untersuchungen nicht nur maßgeblich dazu beigetragen haben, das Potential von Eisenaluminiden hinsichtlich deren Einsatzes in Turboladern abzuschätzen, sondern auch gezielte Legierungszusammensetzungen für jeweilige Komponenten des Turboladers ermittelt werden konnten. Dies führte auch zu legierungsspezifischen Patentanträgen für Komponenten in Turboladern [242-244].

Hiermit erkläre ich, dass ich die vorliegende Arbeit selbständig angefertigt und keine anderen als die angegebenen Quellen und Hilfsmittel benutzt sowie die wörtlich und inhaltlich übernommenen Stellen als solche kenntlich gemacht und die Satzung der Universität Karlsruhe (TH) zur Sicherung guter wissenschaftlicher Praxis in der jeweils gültigen Fassung beachtet habe.

Daniel Janda Karlsruhe, den

Table of contents

Nomenclature

List of symbols

A	Surface area
a_M	Thermodynamic activity of metal
$a_{M_xO_y}$	Thermodynamic activity of oxide
B	Work hardening exponent
b	Burgers vector
c	Concentration
C_p	Specific heat
d	Grain size
d_G	Glide plane spacing
d_P	Spacing between diffracting planes
E_p	Peierls energy
ε	Strain
$\dot{\varepsilon}$	Strain rate
ε_I	Total amount of strain in stage I (creep)
$\dot{\varepsilon}_{ss}$	Steady-state creep rate
ΔG	Gibbs free energy
$\Delta G^*(\tau)$	Activation energy to overcome Peierls stress for a given shear stress
Δm	Mass gain
ΔS	Change in Entropy
$\Delta T_c^{D03\text{-}B2}$	Difference in the $D0_3$-B2 transition temperature
φ	Strengthening particle size
G	Shear modulus
H_V^F	Vacancy formation enthalpy
H_V^M	Vacancy migration enthalpy
h	Strain hardening rate
IOD	Internal oxidation depth
K	Equilibrium constant

k	Boltzmann constant
k_I	Internal oxidation related parabolic rate constant
k_l	Linear rate constant of oxidation
k_p	Mass gain related parabolic rate constant
k_p'	Oxide scale related parabolic rate constant
k_{HP}	Hall-Petch constant
L	Measuring length
l	Distance between dislocations
λ	Wavelength
λ_S	Inter-particle separation
M	Material parameter
m	Mass
m^{-1}	Measure for transition time between stage I and II (creep)
n	Stress exponent
n_D	Number of dendrites within the measuring length
P	Partial pressure
p	Grain size exponent
pH	Negative logarithmic value of the hydrogen ion (H^+) concentration
ρ	Density
ρ_L	Density of liquid
ρ_m	Mobile dislocation density
θ	Incident angle of beam
Q	Activation energy
Q_l	Activation energy for lattice self-diffusion
Q_{gb}	Activation energy for grain boundary diffusion
Q_p	Activation energy for pipe diffusion (along dislocation cores)
Q_i	Activation energy for inter-diffusion of solute atoms
R	Avogadro constant
r	Recovery rate
r_p	Rate for overcoming Peierls stress

S	Microstructural parameter
σ	Stress
σ_0	Friction stress
σ_{OR}	Orowan stress
σ_y	Yield stress
T	Temperature
t	Time
T_c	Transition temperature
T_C	Curie temperature
T_{C2}	Critical temperature beyond thermal activation of overcoming of Peierls stress is thermally assisted
T_H	Homologous temperature
τ_{AT}	Athermal component of flow stress
τ_F	Flow stress
τ_P	Peierls stress
τ_T	Thermal component of flow stress
V	Magnification of image
$\bar{v}$	Average dislocation velocity
υ	Poisson ratio
υ_D	Vibration frequency of dislocation
W_A	Weight of specimen in air
W_L	Weight of specimen in liquid
Ψ	Fraction of plastic work converted to heat
X	Oxide scale thickness
y_s	Yield strength at zero plastic strain

List of abbreviations

APB	Antiphase boundary
bcc	Body centered cubic

BDTT	Brittle to ductile transition temperature
BF	Bright field
BSE	Back-scattered electrons
DF	Dark field
dsb	Diffuse shear band
DSC	Differential scanning calorimetry
EBSD	Electron back-scattered diffraction
EDM	Electron discharge machining
EDX	Energy dispersive X-ray spectrometer
EPMA	Electron probe micro analysis
fcc	Face centered cubic
FIB	Focused ion beam
GD	Glow discharge
ICP	Inductively coupled plasma
LAADF	Low-angle annular dark field
MA	Mechanical alloying
KAM	Kernel Average Misorientation mapping
ODS	Oxide dispersion strengthening
OES	Optical emission spectrometry
OPS	Oxide polishing suspension
P92	Pearlitic-martensitic 9 wt.% Cr steel for steam turbine applications
PAS	Positron annihilation spectroscopy
SDAS	Secondary dendrite arm spacing
SE	Secondary electrons
SEM	Scanning electron microscope
SPD	Severe plastic deformation
ss	Steady-state
ta	Twinned area
TEM	Transmission electron microscope
VG	Variable geometry

VGT	Variable geometry turbocharger
XRD	X-ray diffraction

1. Introduction

Materials have always played an important role in human history. The knowledge of new materials and especially their processing was always a crucial factor in advancement of society. Nowadays we believe to be in the so-called “Information Age” that could not be achieved without continuous development of new materials. In contrast to former ages, where structural materials dominated history, functional materials (such as semiconductors) did herald our age today. However, as the world will always have a demand for structural applications, in particular in the transport business, the development of materials for structural applications is and will always be one of the keys to technological progress.

A closer look into the past decades reveals that scarcity of resources is a hot topic of today and the future. The evolution of oil price clearly demonstrates this relationship (see Figure 1.1).

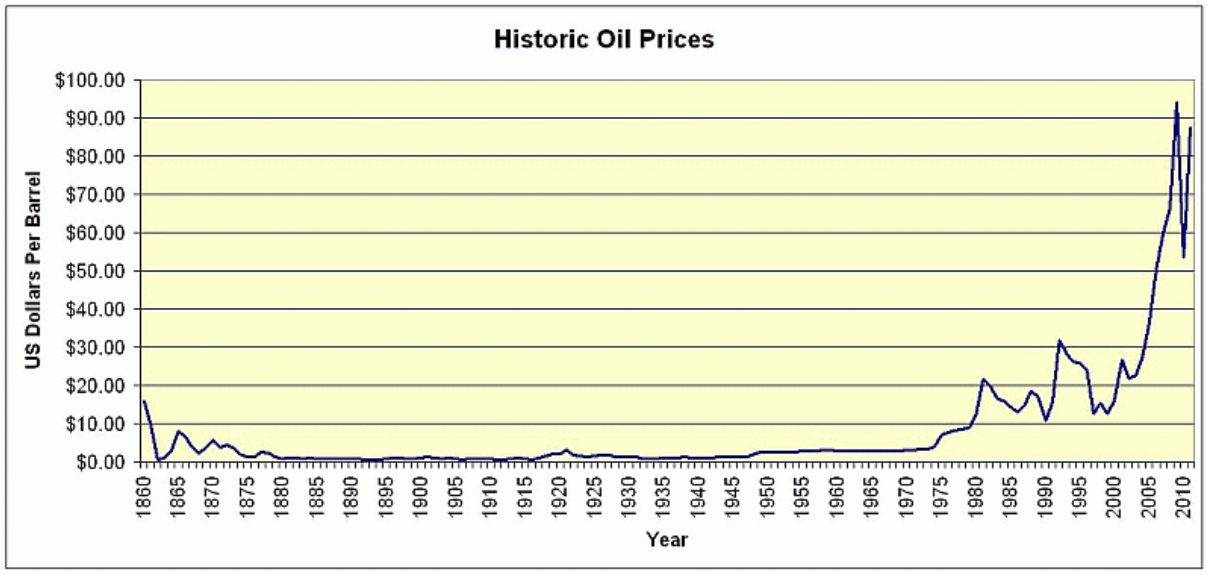

Figure 1.1: Historic evolution of oil prices [1].

Hence, energy efficiency is an important goal of developments in transportation sector in order to save resources and to protect the environment, which suffers from pollutants. Research in the field of “energy saving” becomes more and more popular as public funding is given by the governments all over the world for research on this topic. In this context also at KIT a program-oriented funding on energy efficiency, materials and resources (EMR) for restructuring energy supplies will start in 2015. Regarding the trend in Figure 1.1, it may even be reasonable that the approval rates for public funding dealing with “energy saving” will be higher in the future. One of the most influenced industrial sectors dealing with fossil energy

and emission saving technologies is the automotive industry. On the one hand, petroleum-based fuels are getting more and more expensive, on the other hand legal requirements towards cleaner exhaust gases are intensified periodically. Beyond alternative driving technologies (which are far away from large scale serial productions), downsizing of combustion engines by applying turbochargers is a common way to meet the requirements of fuel and emission savings.

The framework of investigations for the present thesis was given by a project funded by the "Bundesministerium für Wirtschaft und Technologie" (BMWi) in collaboration with several industrial partners from the automotive supply industry. The goal of our project was to investigate whether iron aluminides are possible candidates for substituting established materials in turbochargers with variable turbine geometry (VGT) for gasoline engines. The outstanding oxidation behavior of iron aluminides in hostile environments, their low cost in raw materials, low density, and ease of fabrication in contrast to nickel-based superalloys, titanium aluminides and high alloyed steels (such as P92) makes them attractive candidates [2-4]. The main task within the present thesis was to investigate important aspects of material science. This involves the choice of alloy composition, investigations of microstructure, oxidation behavior, and mechanical properties. The frame conditions for experiments (such as temperature for oxidation experiments and so on) were given by the industrial partners. Various material parameters were determined during the project to provide necessary information for the industrial partners. The three most challenging aspects from the scientific point of view provide the basis for the present thesis besides the characterization of the alloys in the as-cast state, namely: oxidation behavior, creep behavior, and plasticity at room temperature as a function of strain rate. The motivation for these investigations in context of the above mentioned turbocharger project is described in the following. A sketch of a VG-turbocharger is given in Figure 1.2.

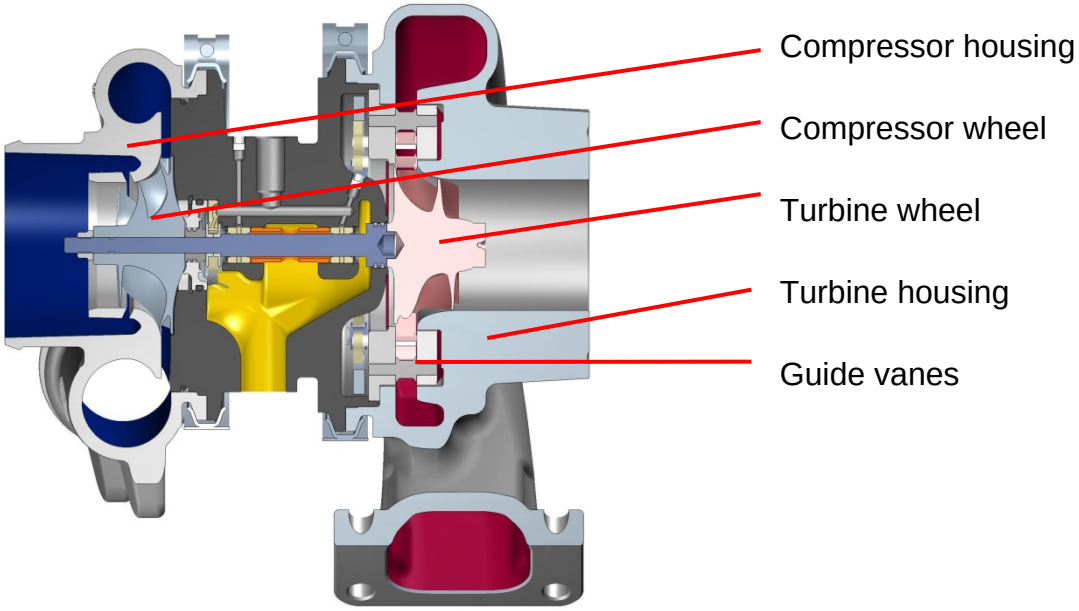

Figure 1.2: Sketch of VG-turbocharger [5].

The oxidation behavior is relevant inside the turbine housing, which is heated up to about 1050 °C by exhaust fumes. The turbine housing and guide vanes are exposed to temperatures in this regime, however without noticeable mechanical stresses. The operating conditions are more complex at the turbine wheel which suffers not only from oxidation but also from superimposed mechanical stresses as a result of the centrifugal forces during rotation (at maximum performance more than 100.000 revolutions per minute can be reached [6]). Therefore, for investigations of the high temperature plasticity, creep experiments were carried out. In literature an abundance of creep data is provided in the range of 600 - 650 °C, because steam turbines are sought to operate at those temperatures [7]. For the sake of comparison of the investigated alloys with other materials for high temperature applications, the creep experiments were also carried out in this temperature regime. Further, this temperature range is of importance, as it is about 0.5 of the homologous temperature[a] for the investigated alloys and, hence, may limit their applicability if mechanical stresses play a major role. The lack in strength of iron aluminides beyond 650 °C makes them unalluring for turbine wheels, whereas compressor wheels are exposed only to temperatures of about 380 °C [8]. Aluminum alloys cannot be used at temperatures of 380 °C, because of ongoing microstructural changes leading to severe material softening, thus, their applicability is restricted to about 220 °C [9]. Steels and nickel-based alloy are too heavy and titanium-based

[a] homologous temperature expresses the temperature of a material as a fraction of its melting point temperature using the Kelvin scale

alloys are expensive and difficult to machine. Therefore, iron aluminides may become a promising option compared to high-alloyed steels and nickel-based alloys which are currently installed in compressor wheels. If failure of the turbine or compressor wheel during operation occurs, this will result in a high-speed impact on the surrounding housings. In terms of containment issues it is, thus, important to know the amount of impact energy that can be consumed by plastic deformation of the housing. In a first order approximation whether the aforementioned iron aluminide alloys can meet the requirements, the mechanical response of the alloys were tested at various high strain rates (up to 2400 s^{-1}).

As an outcome of these considerations, the structure of the present thesis is as follows: After Chapter 2 which deals with the description of the experimental methods utilized, Chapter 3 presents an overview of the major findings on FeAl based alloys available in literature. Results and discussion on the above mentioned three major subjects from a scientific point of view will be given in the corresponding Chapters 4, 5, and 6, whereas considerations of the applicability of iron aluminides for assembling parts in turbochargers are given at the very end of the thesis in the Chapter 7 “summary and conclusions”.

2. Experimental & Methods

The experimental methods presented in this Chapter are the basis for the investigations. In a few cases slight modifications of the experimental procedure were done and mentioned explicitly where applicable.

2.1. Manufacturing & Processing

This Chapter gives a description of the methods, which are used to manufacture samples for many kind of investigation starting from high purity raw material.

2.1.1. Induction melting

The investigated alloys were produced by induction melting from high purity pellets and powders at Max-Planck-Institut für Eisenforschung GmbH (MPIE) in Düsseldorf. Each alloy was produced in a furnace with a capacity of 50 kg under vacuum conditions. For further processing the alloy were cut into smaller pieces by a water-cooled circular saw.

2.1.2. Centrifugal casting

The solid raw material is placed inside a crucible, which is centered on an engine-driven bogie. The chill mold is placed on the edge of the bogie and starts rotating around the center of the crucible when the raw material is melted. Then the crucible is tilted towards the chill mold and the melt is accelerated by the centrifugal force in the direction of the chill mold (see Figure 2.1).

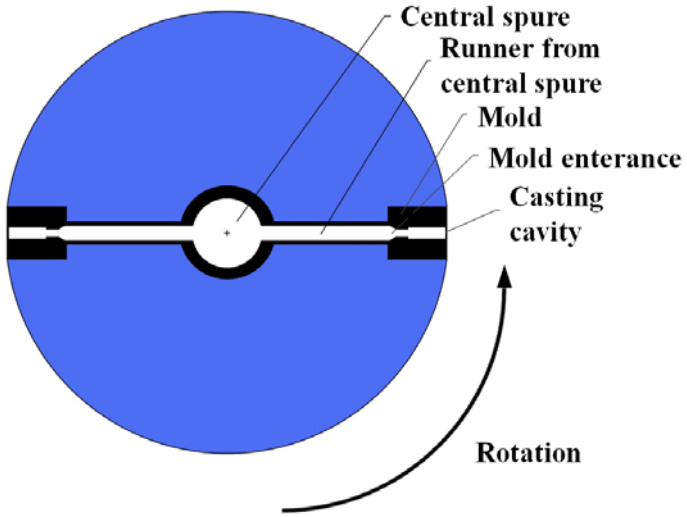

Figure 2.1: Schematic setup of a centrifugal casting mold entrance.

The casting was performed at Access e.V. in Aachen. Alloys were produced under vacuum conditions (0.1 mbar) to minimize the formation of cavities and contamination arising from gases. The melt was heated up to about 40°C above the liquidus temperature before it was cast into chill mold to reduce the viscosity of the melt. The chill mold was pre-heated to 1200 °C to reduce the thermal gradient inside the sample during cool-down to achieve a homogenous microstructure across the sample. The cluster of rods and a sketch of a rod are given in Figure 2.2.

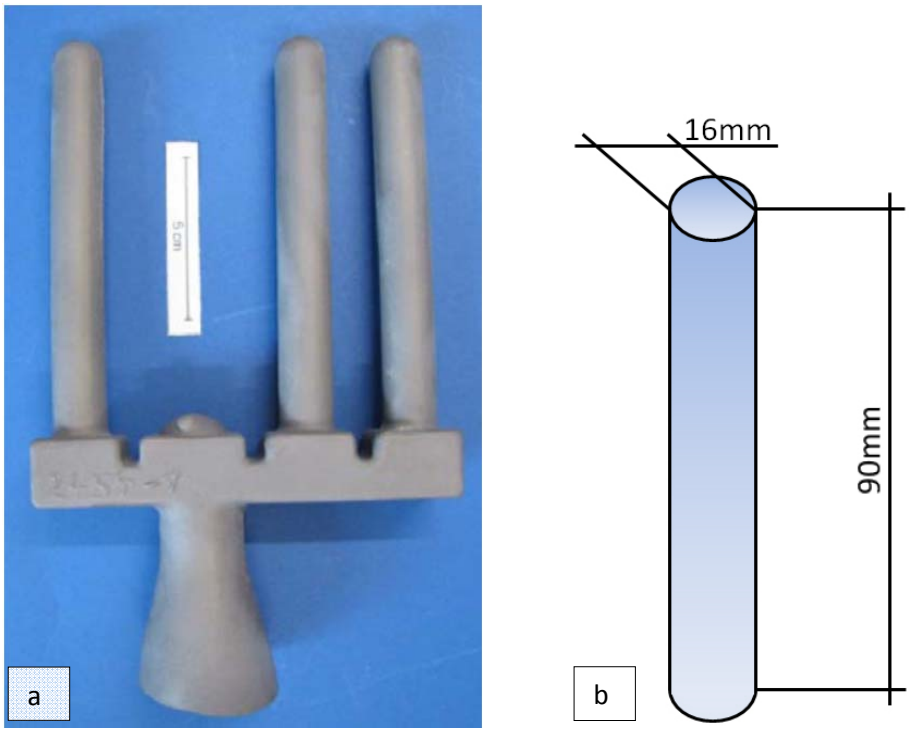

Figure 2.2: a) Cluster of delivered rods b) Sketch of a rod labeled with dimensions.

2.1.3. EDM

A final shape giving process was done by electro-discharge machining (EDM) at WMI GmbH in Irxleben. The rod is connected as anode whereas the cutting wire is the cathode. This setup is running in water and a voltage pulse is applied resulting in a spark that is electro-eroding the work piece. The cutting wire is running with a constant speed and applied voltage through the rod. Thereby, the cutting results in very accurate surfaces. The rod, which is shown in Figure 2.2b, was sectioned into various specimens, which are listed in Table 2.1.

Table 2.1: Different types of specimens machined by EDM.

Purpose of specimen	Geometry	Dimensions [mm]
mechanical testing	square prism	8 · 5 · 5
mechanical testing	cube	5 · 5 · 5
mechanical testing	cylinder	Ø5 · 5
thermophysical properties	square prism	3.5 · 3.5 · 2

The sample taking was performed in equidistant positions from the center of the rod to ensure comparable microstructures inside the specimens. Moreover, sample taking close to the cast skin was avoided due to other microstructures present there. This is exemplarily shown for cubic shaped specimens in Figure 2.3.

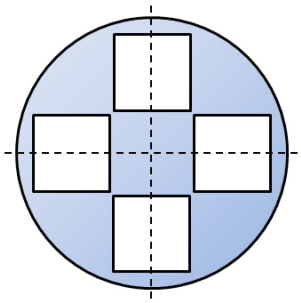

Figure 2.3: Top view of rod, specimen taking for cubes.

2.1.4. Grinding & polishing & etching

Grinding and polishing were done on various plate-mounted wheels with equipped water rinsing (for example Buehler EcoMet 300 Pro). Depending on surface conditions after cutting, wet emery papers were used with successively finer granulation. The final granulation used was 4000, with a mean grain size of 6 µm of abrasive particles, for imaging microstructures before subsequent polishing. First polishing step was performed on a shag-piled wheel with 3 and 1 µm diamond polishing paste, respectively, with ethanol-based lubrication. The final polishing step was done with alkaline OPS suspension (0.05 µm grain size and pH-value of 10) on a short-piled wheel with distilled water. Subsequent etching was necessary to reveal the microstructure. The used etching solution which showed the best results is called “Kroll” and contains the following ingredients:

100 ml distilled H_2O
2 ml HF
2 ml HNO_3

The surfaces were dipped for several seconds into the etching solution and subsequently rinsed with water to stop the etching. Afterwards the specimen is rinsed with ethanol and dried using a hot air blower. This procedure was repeated several times until the dendritic structure became visible in an optical microscope. Surface preparation of discs and cuboids for mechanical testing and oxidation test was utilized by grinding, until a 1000-grit finish, with a mean grain size of 18 μm of abrasive particles, without additional polishing. In addition, special focus was given to achieve coplanar surfaces for a homogeneous stress distribution inside the samples during compression testing. A uniquely designed grinding tool was used for this step of preparation. For cleaning between the preparation steps an ultrasonic bath filled with ethanol was used.

2.2. Microstructural investigations

In the following subchapters the methodologies are described for microstructural investigations from the macroscopic down to microscopic scale in terms of arrangement of phases, chemical composition, and the state of crystallographic order. One should notice that the alloys were not thermo-mechanically manufactured and hence exhibit a typical cast dendritic structure.

2.2.1. Archimedean and geometrical density

The Archimedean density is determined by weighing the sample in air and then in a liquid with a known density (distilled water in this case). In order to determine the density as accurate as possible, the samples were polished and the temperature of the water was measured prior testing to correct the temperature dependence of the water density. The densities were calculated as follows:

$$\rho = \frac{W_A \cdot \rho_L}{W_A - W_L} \tag{2.1}$$

ρ: *Density of the sample*

ρ_L: *Density of liquid*

W_A: *Weight of specimen in air*

W_L: *Weight of specimen in liquid*

Five different samples of each alloy were measured for statistical reasons. The geometrical density was determined by dividing the volume of sample (measuring the length of each side of a cuboid sample) by its weight. The results are presented in Table 3.2.

2.2.2. Optical Microscopy

The arrangement of microstructure on macroscopic scale was investigated by optical microscopy. Thereby the characteristics of the dendrites and micro-constituents were analyzed. The microstructure was revealed as described in Chapter 2.1.4. Several microscopes were used for these investigations (for example Zeiss Axiovert 200 MAT and Leica Leitz Aristomet).

2.2.3. SEM

The SEM analysis was performed with a Philips XL30 FEG (equipped with a field emission gun) where secondary electrons (SE) and back-scattered electron (BSE) were used for imaging. Further, an energy dispersive X-ray spectrometer (EDX) was coupled to analyze the characteristic X-ray emission of the elements constituting the alloys. For element mapping, a high resolution electron probe micro analysis (EPMA) was used at "DECHEMA: Gesellschaft für Chemische Technik und Biotechnologie e.V." in Frankfurt.

2.2.4. EBSD

The electron back-scattered diffraction (EBSD)-measurements were carried out in a FEI high resolution scanning electron microscope equipped with TSL OIM 4 software for orientation mapping of the matrix phase and the precipitates, respectively. For the FeAl matrix phase the structure database of ferrite and for the precipitates that of type NbC (both cubic structures) were used for indexing resulting in sufficient high confidence indices (up to 0.95). The working distance was 15 mm with step sizes of 35 - 100 nm.

2.2.5. FIB

The specimen preparation for TEM and micropillar investigations was done in a dual beam SEM-FIB (focused ion beam) (FEI, Helios Nanolab 600 dual beam FIB). For TEM analysis lamellae were prepared by lift-off technique. The surface facing the gallium ions was protected by prior deposition of platinum. The micropillars were milled to a cylindrical shape with 30 keV Ga ions using iteratively lower currents with a final milling current of 9.7 pA. The corresponding micropillars are presented in Figure 5.10.

2.2.6. TEM

For TEM analysis a Phillips CM20 and FEI Titan 80-300 equipped with an EDX system were used. For analysis of local crystallographic order diffraction images were recorded. For

imaging the arrangement of the phases bright field (BF), dark field (DF), and high-angle angular dark field (HAADF) modes were used in the TEM. The working scheme of a TEM is for example given in detail by Fultz and Howe [10].

2.2.7. ICP-OES

Chemical analysis of bulk material was done by inductively coupled plasma optical emission spectrometry (ICP-OES) for iron, aluminum, niobium, and zirconium. About 100 µg of a sample was transferred into aqueous solution by ammonium chloride. The dilute solution was sprayed into plasma and atomized and thus excited for emission characteristic electromagnetic radiation. The intensity of characteristic emissions was correlated with the concentration of each element.

2.2.8. GD-OES

Chemical analysis of bulk material was also carried out by glow discharge optical emission spectroscopy (GD-OES). The surface of a polished sample was used as cathode and exposed to argon plasma. The evaporated atoms from the sample, which are excited in the plasma, are analyzed by OES as described above.

2.2.9. DSC

Differential scanning calorimetry (DSC) utilizing a Netzsch DSC404 F1 instrument was used for the determination of phase transition temperatures. This is a thermo-analytical technique where the heat flow from a sample relative to a reference of known heat capacity is calculated during heating and cooling cycles. Thereby endothermic and exothermic reactions can be detected and correlated with the specific temperatures of those events. The corresponding data is presented in Figure 3.13 and Figure 3.14.

2.2.10. XRD

The crystal structures of the phases were analyzed by X-ray diffraction (XRD) (Bruker AXS, D8 series2) and a Lynxeye detector using a copper X-ray source and a step size 0.005°. Thereby the diffracted X-ray beam is analyzed in terms of angle and intensity by utilizing Bragg's law:

$$2d_P \cdot \sin\theta = n \cdot \lambda \qquad (2.2)$$

d_P: *Spacing between diffracting planes*

θ: *Incident angle of beam*

$n \cdot \lambda$: *Integer multiple of the wavelength*

The observed peaks in the diffractogram are then compared with established literature data to identify the specific crystal structures of phases.

2.3. Mechanical testing

Mechanical testing was performed under various conditions. For the evaluation of the effect of strain rate on the deformation response tests were carried out in compression using (i) a screw-driven load frame, (ii) a drop impact tester, and (iii) a split-Hopkinson pressure bar at quasi-static, intermediate and dynamic strain rates, respectively. This is described in more detail in subchapter 2.3.3 and following.

2.3.1. Hardness measurements

Hardness measurements were performed using the Vickers method with loads of 200 and 2000 g, respectively (Leco M 400 G2). Each measurement was repeated at least ten times for statistical reasons. The loads were applied for 10 s before final unloading.

2.3.2. Measurement of shear modulus

The measurement of shear modulus was done by using the resonance method at the "Bundesanstalt für Materialforschung" (BAM) in Berlin. Therefore, the resonance frequency of the torsional vibration was measured utilizing an ELASTRON 2000 (HTM Reetz Berlin) device at various temperatures. The samples had a length of 100 mm and 6 mm in diameter. They were attached to the piezoelectric transmitter-receiver system by carbon fibers inside the oven and resonance frequencies were measured. For each alloy four samples were tested for statistical reasons. The averaged results are presented in Figure 6.4.

2.3.3. Screw driven load frame

Deformation-controlled compression tests at room- and elevated temperatures for strain rates in the range of 10^{-4} – 10^{-1} s^{-1} were carried out in a screw-driven load frame (Instron 5569), which can be optionally equipped with a radiation furnace. Each measurement was repeated at least with two different samples to check reproducibility. Additional test were done if necessary to calculate mean values.

2.3.4. Drop impact

Compression tests at intermediate strain rates were carried out by drop impact testing at Chemnitz University of Technology, Institute of Materials Science and Engineering. The achieved strain rates were in the range of 120 s^{-1}. A weight was dropped on the top-surface of a sample and stopped after the first impact to avoid additional bouncing on the sample. The strain was recorded by strain gauges. Each measurement was repeated with two different samples to check reproducibility.

2.3.5. Split-Hopkinson pressure bar

Compression tests at high strain rates ($\geq 10^3$ s^{-1}) were performed with a split-Hopkinson pressure bar at Brown University, Providence, Rhode Island. The specimens were lubricated with grease and sandwiched between and incident and a transmission bar (see Figure 2.4).

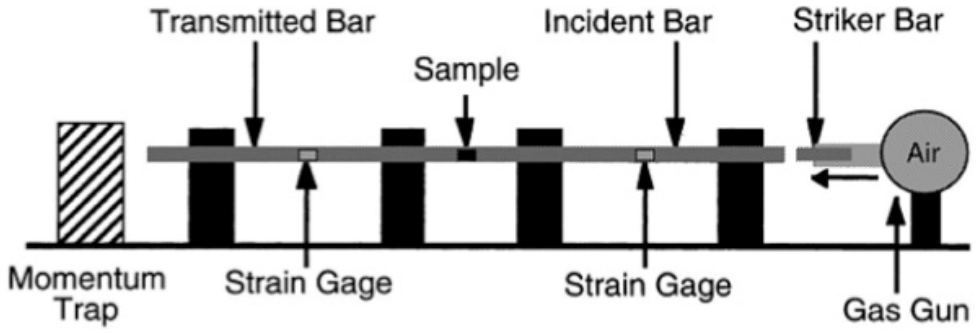

Figure 2.4: Schematic of a compression split-Hopkinson pressure bar [11].

The striker is hitting the incident bar and an elastic wave is propagating trough the incident and transmitted bar. The sandwiched sample in between is deformed plastically. The elastic waves are recorded by strain gauges on the bars and in turn used to determine stress-strain conditions at each end of the sample. The reflected wave at the end of the transmitted bar was trapped to avoid multiple loading of the sample. The strain rate is related to the velocity of the striker bar which was measured in front of the incident bar. The amount of strain within the sample was controlled by the mass of the striker bar, which is related to its kinetic energy. Each measurement was repeated at least twice to check reproducibility. Additional tests were done if necessary to average the resulting values. More details of this technique are given in Ref. [11].

2.3.6. Creep testing

Compressive creep experiments in the range of 625 to 700 °C were carried out on a screw-driven load frame (Zwick Z100 SW) attached with a high-temperature vacuum furnace (Maytec MSRA-81/P/RS-2). The vacuum condition inside the furnace was in the range of 10^{-7} mbar and temperature stability is within the range of ±1 K. The samples were lubricated prior testing with boron nitride aerosol spray to decrease the friction at the contact area machine/sample. To achieve a constant state of true stress inside the specimen, the load was continuously increased with strain in a computer controlled closed loop mode (assuming uniform deformation of the sample). The specimens showed almost no buckling or barreling after creep and hence the term "true" is valid for the calculated strains and stresses. In most of the experiments, either the applied stress or temperature was alternated during experiments after a steady-state creep rate was established. Additional creep test were carried out in a "Zwick 1478" load frame to evaluate the influence of air exposure instead of vacuum. The specimen was inductively heated by a copper coil and the temperature was measured and controlled by a thermocouple attached to the specimen surface. The applied force was constant during the measurements. Deviations of the creep behavior related to test-atmosphere could not be observed in the present thesis.

2.3.7. Micropillar testing

Micropillars were deformed with a Hysitron Triboscope nanoindenter equipped with a 10 µm diameter flat punch tip. The diameters of the micropillars were between 2.5 and 4 µm with an aspect ratio of about 2:1. Since these micropillars are frequently slightly vertically tapered, the diameter of the top and the bottom of each micropillar was measured and averaged for calculation of nominal stress. All micropillar compression tests were conducted at a nominal constant strain rate of 10^{-3} s^{-1}.

2.4. Cyclic oxidation

Cyclic oxidation was performed in a muffle furnace at 750, 900 and 1050 °C for durations of up to 550 h in laboratory air. Mass change with time was recorded in intervals weighing the samples outside the furnace after a 45 min cool down to room temperature. Test specimens had been cut out of 15 mm diameter rods using a low speed saw. The specimens were sectioned into disks with a height of 3 mm and 15 mm in diameter and polished to a 1000-grit finish.

3. FeAl alloys

In this Chapter an overview of alloying concepts as applied to iron aluminides from the past decades is presented. Special emphasis is given to the developments to determine promising candidate materials for structural application (at elevated temperatures). A more detailed insight into the fundamentals of oxidation, plasticity below creep temperatures, and creep behavior is presented in the beginning of Chapters 4, 5, and 6, respectively. The choice of alloy compositions for investigations based on the literature survey are discussed and characterized at the end of this Chapter.

3.1. Literature survey

3.1.1. The binary Fe-Al system

The phase diagram for binary iron aluminides were studied in detail by [12-16]. By alloying aluminum into iron the disordered body centered cubic (bcc) crystal structure (ferrite phase) is stabilized (see Figure 3.1).

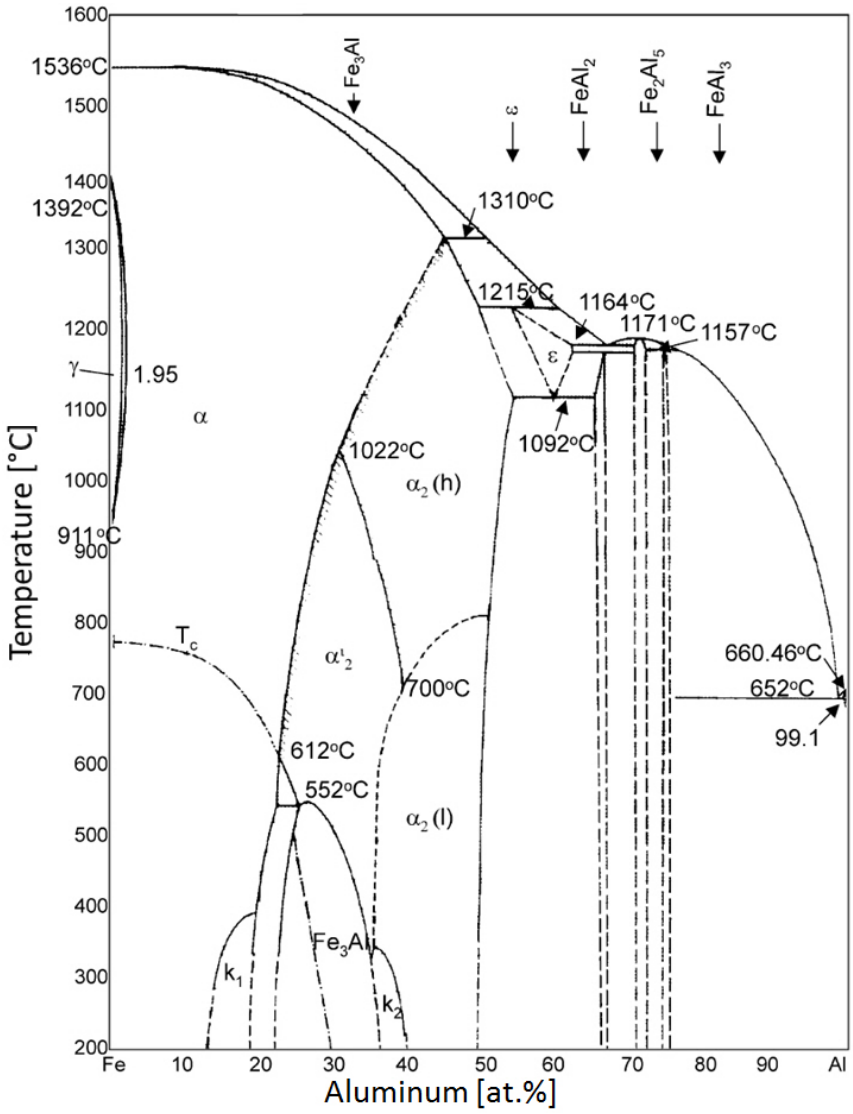

Figure 3.1: Fe-Al phase diagram [14].

At aluminum contents in the vicinity of 25 at.% aluminum and temperatures below 545 °C the intermetallic phase Fe_3Al is formed. This phase is also based on the bcc crystal structure such as the ferrite phase but forms the $D0_3$-ordered superlattice, which is shown in Figure 3.2a [17].

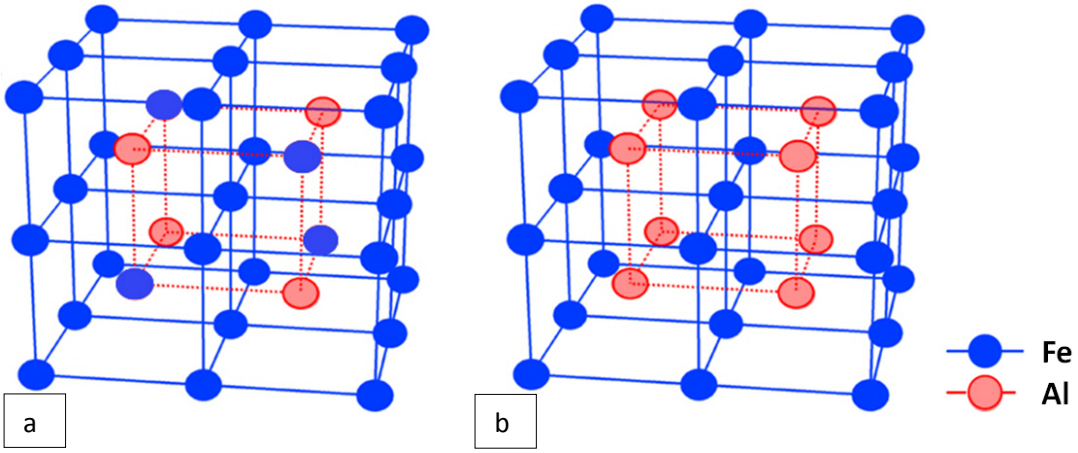

Figure 3.2: Unit cells of a) $D0_3$-ordered Fe_3Al and b) B2-ordered FeAl.

The unit cell of Fe_3Al is eight times larger than the disordered ferrite phase, because only every second body centered position is occupied by an aluminum atom. The next upcoming phase at increasing aluminum contents up to 50 at.% aluminum is FeAl which exhibits B2-order and is also based on the bcc crystal structure (see Figure 3.2b). The unit cell of FeAl has the same size as the disordered ferrite phase and can be seen as two primitive cubic lattices, which are nested within each other. However, in Figure 3.2b eight B2-ordered FeAl unit cells are shown for comparison with the larger unit cell of $D0_3$-ordered Fe_3Al (see Figure 3.2a).

Additional phase boundaries are drawn within the phase fields of Fe_3Al and FeAl (see Figure 3.1). Starting from low aluminum contents the transition from paramagnetic to ferromagnetic behavior is observed if the temperature falls below the Curie temperature (T_c). The two-phase fields k_1 and k_2 border the $D0_3$ phase field at higher and lower aluminum contents below 400 °C. The physical origin of these two-phase fields are still discussed in literature and so far not fully rationalized [12][14][16][18]. The B2 phase field is subdivided into the three-phase fields α'_2, $\alpha_2(h)$, and $\alpha_2(l)$ [16]. Measurements of Young's modulus and thermal expansion coefficients exhibit discontinuities and the subdivision of the phase field is based on these results. Later work by Hehenkamp et al. revealed by positron annihilation spectroscopy (PAS) that these discontinuities are the result of different defect structures in the B2 phase field [19]. In the area α'_2 below 35 at.% Al only single vacancies are present. In $\alpha_2(l)$ triple defects are stable and at higher temperatures in the $\alpha_2(h)$ area the formation of additional pairs of vacancies were observed [19]. More detailed information of these defect structures are summarized in a detailed review by Jordan and Deevi [20].

The main focus in literature is placed on the intermetallic phases Fe_3Al and FeAl in the Fe-Al system. Their high symmetry crystal structure is associated with the best potential for

plasticity in contrast to the other upcoming intermetallic phases at higher aluminum contents with lower crystal symmetry. In binary iron aluminides it was found that $D0_3$-ordered Fe_3Al in contrast to B2-ordered FeAl is in general more ductile at room temperature and stronger at elevated temperatures [21-24]. FeAl alloys beyond B2-ordered single-phase FeAl in the range of 60 at.% Al may have potential for high temperature structural applications. These alloys exhibit a fine lamellar microstructure (lamella spacing <100 nm) of B2-ordered FeAl and triclinic $FeAl_2$ by eutectoid decomposition of the high-temperature ε-phase (Fe_8Al_5) [25]. While low symmetry crystal structures such as triclinic $FeAl_2$ are known to be very brittle these alloys might have some potential for plastic deformability due to their fine scaled microstructure in a two-phase composite as already demonstrated for some γ-TiAl alloys [26]. These lamellar γ-TiAl alloys consist of two relatively brittle phases (Ti_3Al (α2) and TiAl (γ)) but exhibit a reproducible amount of ductility when tensile tested at room temperature [26]. Detailed analyses of fine-scaled in-situ Fe-Al composites are not published yet. At Al concentrations beyond ~68 at.% Al the intermetallic phase Fe_2Al_5 and Fe_4Al_{13} are present.

FeAl alloys, which are $D0_3$- or B2-ordered seem to have the best potential for structural applications but still do not meet industrial requirements for serial production. The main drawbacks, which still need to be overcome are the rather low tensile ductility at room temperature and the pronounced drop in strength above ~600 °C [3][21][27-30]. The reasons for low ductility at room temperature are (i) impeded dislocation motion due to the ordered lattice structure and (ii) the susceptibility towards moisture resulting in hydrogen embrittlement [31-33]. The detrimental effect of hydrogen has been explained by the reaction of a propagating crack tip with water vapor, whereby atomic hydrogen is injected into the alloy resulting in easier failure [32]. A good approach to increase ductility is, thus, the refinement of grain size [30][34-36]. In general terms it is well established that grain size refinement is a potent way to improve ductility [37]. This can be achieved by alloying and processing. For example, refinement of grain size by adding 0.05 at.% zirconium and 0.24 at.% boron increased the room temperature ductility of Fe-35.8Al from 2.2 to 10.7 % [38].

There are several processing techniques to establish a very fine grain size (<1 μm) such as mechanical alloying (MA), rapid solidification techniques, and severe plastic deformation (SPD). Mechanically alloyed FeAl alloys can exhibit a ductility of 5 – 10 % at reasonable levels of strength in tensile testing [39][40]. Also Gunther and Morris demonstrated the beneficial effect of a small grain size on the ductility by mechanical alloying of Fe-40Al [41].

Moreover a small grain size is also favorable for high strength below 0.5 of the homologous temperature as known from the Hall-Petch relationship:

$$\sigma_y = \sigma_0 + k_{HP} \frac{1}{\sqrt{d}} \quad (3.1)$$

σ_y: *Yield stress*

σ_0: *Friction stress (constant)*

k_{HP}: *Hall-Petch constant*

d: *Mean grain size*

σ_0 is a friction stress, which includes contributions from solutes and particles but not from dislocations [42]. Beyond homologous temperatures of 0.5, where creep deformation dominates plasticity (depending on strain rate) a small grain size can be detrimental due to the promotion of grain boundary slip. Hence, processing is important and has to be correlated to the desired field of application. In the past decades, a lot of progress was achieved to meet the requirements for structural applications [36][43][44] and some researchers believe that iron aluminides are almost ready for industrial applications, for example in fossil fuel technologies [34].

3.1.2. Fe-Al-X systems

Several concepts of alloying from the past decades are shown in the following that were considered to improve the mechanical properties of iron aluminides. These are: 1) solid-solution hardening, 2) stabilization of $D0_3$-order up to higher temperatures, 3) introduction of additional phases such as carbides, borides, Laves phases and oxides for dispersion (ODS) or precipitation strengthening. In discussing these concepts, attention should be given not only to the type and quantity of alloying element added but also how it partitions to the different phases, thereby influencing the properties of the individual phases and the alloy as a whole.

3.1.2.1. Solid-solution hardening

Elastic interactions (size and modulus effects) of the solutes and the matrix atoms of the crystal lattice are responsible for an increase in strength. The increase in yield strength is explained by either creation of strain within the lattice (atomic size effect) or by differences in the shear moduli between the lattice and the solute atoms. The effect of random solute distribution on strengthening of solid solutions is described by Fleischer [45][46]. However, the solid solution strengthening of intermetallics is more complicated than of solid solutions. The presence of a super-lattice results in additional factors responsible for strengthening [47]:

i) antisite atoms (the concentration depends on stoichiometry); ii) antiphase boundaries; iii) the position of the sub-lattice which an alloying element prefers. Hence, experimental results of solid solution hardened FeAl alloys with various ternary alloying elements exhibit no consistent trend in strengthening [44][47]. In general, tensile ductility is progressively lost by continuous alloying due to the increase in solid-solution hardening, which inhibits dislocation motion.

A remarkable amount of solid-solution hardening in FeAl (especially in B2-ordered FeAl) can be achieved by **vacancies**. A first phenomenological model was given by George and Baker in 1998 [48]. Its physical reason is based on the relatively low formation enthalpy of vacancies as compared to their unusually high migration enthalpy, which results in an anomalously high concentration of vacancies in the FeAl matrix [49]. For example, for binary Fe-39Al the vacancy formation enthalpy (H_V^F) is 0.98 eV and the migration enthalpy (H_V^M) is 1.7 eV [23]. During cooling (especially at quenching) high amounts of vacancies can retain in the FeAl matrix, which result in additional hardening of the FeAl matrix phase of up to 50 % due to "frozen in" thermal vacancies in contrast to FeAl containing the equilibrium concentration of vacancies [50-52]. More than 3.5 % of thermal vacancies are present in stoichiometric FeAl at the melting point [19][53] and 2.4 % can be retained at room temperature by quenching [54]. For comparison: the vacancy concentration in completely recovered stoichiometric FeAl is 0.5 % [55]. In general, the hardness was found to increase with the square root of vacancy concentration [56][57] and hence, fits qualitatively into the model of solid-solution hardening.

Systematic studies on solid-solution hardening were performed on Fe-Al-X (X=Cr, Mn, Mo, V, Ti) at various temperatures and alloy compositions.

Chromium is a promising alloying candidate as it increases the room temperature tensile ductility of binary Fe-28Al from 3.7 % up to 9 % by alloying with 2 – 6 % chromium due to the suppression of hydrogen embrittlement by moisture [58]. Also in Fe-40Al-5Cr an increase in tensile ductility is observed in comparison to Fe-45Al [59]. However, due to the small size misfit of chromium and iron a significant increase of solid solution hardening is neither observed at room temperature nor at higher temperatures. Even a reduction in yield strength was found in some cases [58][60-62]. An explanation for the reduction of strength in chromium containing Fe_3Al could be a reduction of the $D0_3$-order and stabilization of B2-order, which was found in TEM and XRD investigations [63][64]. Moreover, the anomalously

high concentration of vacancies, which results in solid-solution hardening of binary iron aluminides [48][65] was found to be reduced in Fe-40Al containing chromium [66].

Manganese increases the strength especially at higher temperatures, whereas at room temperature it is hardly changed [67]. Also the room temperature yield strength of B2-ordered Fe-45Al-5Mn-0.2B-0.1Zr in comparison with Fe-45Al-0.2B-0.1Zr (σ_y=325MPa) is only hardly affected [47]. An explanation for the poor room temperature strengthening in contrast to high temperature strengthening by manganese in solid solution is not addressed in Refs. [47][67]. Investigation of Fe-28Al-1.5Mn in comparison to Fe-28Al shows an increase in yield strength up to 250 MPa in the range of 500 - 700 °C and also slightly increasing tensile ductility up to 1.5 % [67]. The beneficial effect of manganese on ductility was found to be a result of the finer grain size in Fe-28Al-1.5Mn.

More promising candidates for strengthening are **cobalt and copper**. By replacing manganese with either cobalt or copper the room temperature yield strength is increased by about 250 MPa [47]. Even more beneficial are additions of **titanium and nickel** in Fe-45Al-5X-0.2B-0.1Zr (X=Ni, Ti). In contrast to manganese, the room temperature yield strength could be increased by about 350 MPa [47]. **Niobium** containing ternary Fe-25Al-2Nb exhibits a room temperature yield strength of 800 MPa, which drops only marginally up to 500 °C [68]. At 600 °C the yield strength is still about 400 MPa and, thus, the alloy is much stronger than binary Fe-30Al (σ_y=100 MPa at 600 °C). In the range of 700 – 750 °C the yield strength comes down to about 200 MPa and almost diminishes at temperatures beyond 800 °C [68]. A chemically akin Fe-25Al-2Nb alloy can exhibit precipitates of Fe_2Nb Laves phase by applying an appropriate heat treatment [68]. The yield stress does not differ considerably up to 500 °C, whereas at higher temperatures the precipitation hardened alloy exhibits lower strength due to a coarse distribution of the Laves phase and the accompanied loss in solid-solution hardening.

3.1.2.2. Stabilization of $L2_1$-order

As already mentioned in Chapter 3.1.1, in binary iron aluminides it was found that $D0_3$-ordered in contrast to B2-ordered FeAl is in general more ductile at room temperature and stronger at elevated temperatures [21-24]. Therefore investigations were started to analyze the ternary equivalent of $D0_3$-order, which is the $L2_1$-order [43] as both structures are structural isotypes (Pearson symbol cF16) [69] (see Figure 3.3).

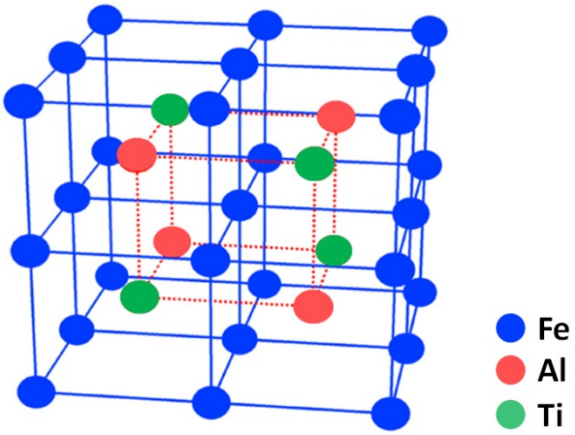

Figure 3.3: Unit cell of $L2_1$-ordered Fe_2AlTi.

The increases in $L2_1$/B2 phase transition temperatures T_C are related to increases in the ordering energies of the $L2_1$ super lattice caused by specific site substitutions by the solutes [70]. The impact of a ternary element on the stability of the $L2_1$-ordered phase was investigated by Stein et al. [71]. They showed that with increasing metallic atomic radii of the ternary element (starting point is the metallic radius of iron) the $L2_1$-B2 phase transition temperature is increased (see Figure 3.4).

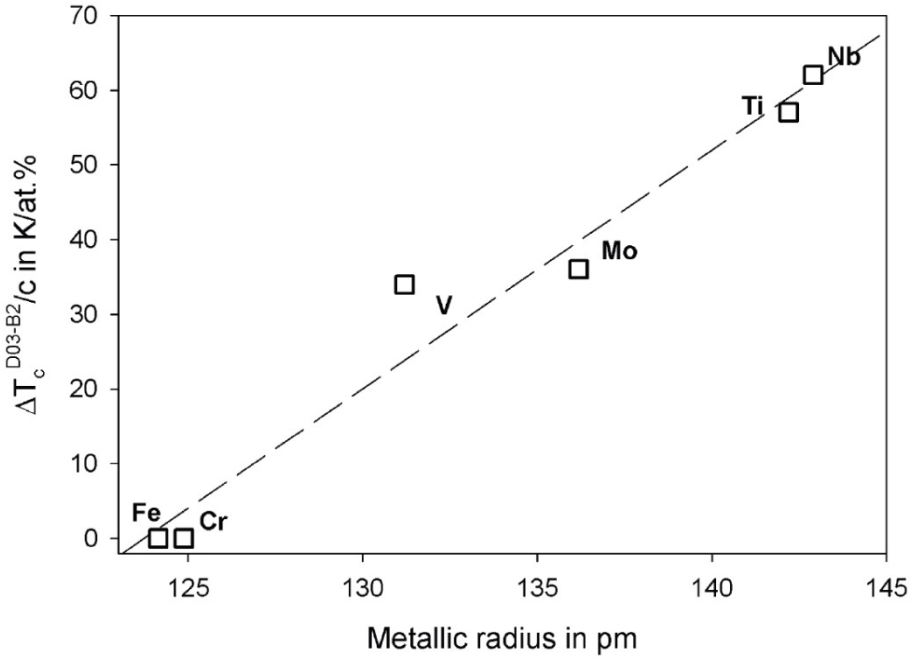

Figure 3.4: Efficiency $\Delta T_c^{D03-B2}/c$ (c being the concentration of solute atoms) of different alloying additions in increasing the $D0_3$-B2 phase transition temperature as a function of the metallic radius (metallic radii for a coordination number of eight, data based on [72][73]).

It should be noted that a sufficient amount of the ternary element must be soluble in the FeAl matrix phase to observe the increase of the $D0_3$-B2 phase transition temperature. It is difficult, thus, to distinguish whether an increase in strength can be attributed to the presence of $L2_1$-order or it is simply an effect of solid-solution hardening, which is always superimposed if $L2_1$-order is present. However, some data in literature give clear evidence of the beneficial effect of $L2_1$-order on strength of iron aluminides at elevated temperatures. The yield stress of three ternary solid-solution hardened Fe-26Al-X (with X = 4 at.% Ti, Mo, V) alloys is highest for the alloy with titanium at 700 °C where Fe-26Al-4Ti exhibits $L2_1$-order and the other alloys B2-order and lowest at 800 °C (all alloys exhibit B2-order at 800 °C) [43]. Hence, solid-solution hardening by alloying with titanium is less efficient at 800 °C than with molybdenum or vanadium, whereas at 700 °C alloying with titanium results in superior strength due to superimposed formation of $L2_1$-order. The substitution of iron by titanium increases the $D0_3$ ($L2_1$) - B2 phase transition temperature from 550 °C (binary Fe_3Al) up to a maximum of 1215 °C at about the stoichiometric composition of Fe_2AlTi [69][74]. In several publications it is also demonstrated that $L2_1$-ordered Fe-Al-Ti alloys exhibit excellent high temperature strength [75-82]. Nevertheless, for structural applications Fe-Al-Ti alloys with high titanium contents are not favorable due to the strong increase of the brittle to ductile transition temperature (BDTT) up to 900 °C [76][82]. Improvements in ductility were

achieved by additions of boron, reducing the BDTT by about 250 °C due to the refinement of grain size [82]. Thereby TiB_2 particles were found to act as heterogeneous nucleation sites for the FeAl matrix phase. By contrast, low amounts of titanium (1 – 2 at.%) were found to improve the room temperature ductility of the FeAl matrix phase by scavenging interstitial impurities such as carbon and eventually promote the formation of carbides [83]. Other favorable ternary Fe-Al-X alloys were so far not identified for a strengthening concept based on the stabilization of $L2_1$-order due to lacking solubility of the ternary element (for example niobium, which is only about 0.8 at.% in Fe_3Al [84]) or low efficiency of increasing the $L2_1$-B2 phase transition temperature (in the case of chromium) [71].

3.1.2.3. Multi-phase FeAl alloys

There are many different ways to establish multi-phase microstructures in iron aluminides. In binary FeAl heterogeneous microstructures can be achieved by excess alloying of aluminum (>50 at.%) as mentioned in Chapter 3.1.1. Also at lower Al contents microstructures composed of ordered-plus-disordered phase mixtures can be obtained in FeAl [85]. These microstructures resemble those of Ni-base γ-γ' superalloys in appearance but are less beneficial in improving the mechanical properties at high temperatures, since it is relatively easier to shear the ordered particles than to bow dislocations in-between them [86]. Alloys containing A2+$D0_3$ domains show an increased yield strength compared to alloys with single-phase A2 or $D0_3$-ordered FeAl [87]. The structural stability of these alloys could be improved by ternary additions of silicon, because of a decreased diffusivity and interface energy [85]. Since the lattice parameters of α-Fe (A2-disordered) and NiAl (B2-ordered) are very similar, coherent microstructures of A2-disordered α-Fe and B2-ordered NiAl precipitates can be generated, which are similar to the γ-γ' microstructures of the Ni-base superalloys [4]. These alloys show improved mechanical properties and very slow coarsening kinetics of the strengthening NiAl precipitates in contrast to binary FeAl alloys [88-90].

Structural and thermal properties of ternary iron aluminides containing carbon, boron, nitrogen, oxygen, and hydrogen compounds were studied by Kellou et al. [91]. They found out that the formation of carbides is most favorable for possible structural applications. The free energy of formation of various carbides, borides, nitrides, and oxides and their solubility in FeAl are given in [29][92]. Alloying with carbon and boron for introduction of carbides and borides has widely been utilized in literature and will be summarized here. The formation of carbides and the influence on mechanical properties was investigated in the ternary Fe-Al-C [91][93][94] and in the quaternary Fe-Al-M-C (with M=Ti, V, Nb, Ta, W, Cr, Mo)

[95-100] system. In general, a reduction in ductility is observed at room temperature, whereas the high temperature strength is improved. The lowered ductility can often be attributed to plate- or needle-shaped carbides that act as internal sites for crack formation, especially at low temperatures where the FeAl matrix is less ductile [3]. On the one hand the ductility of alloys decreases when the amount of the brittle phase increases [39][87]. On the other hand the high temperature strength can be increased significantly. The precipitates exhibit a much higher strength compared to the FeAl matrix. For example the zirconium containing $Zr(Fe,Al)_2$ phase exhibits a strength of 600 MPa at 1000 °C [87]. In ternary Fe-Al-C iron aluminides the increase in strength depends strongly on the carbon content. For example, an increase in strength is observed in Fe-38Al-1C due to the formation of carbides (Fe_3AlC_x), whereas excess alloying with carbon (>1 at.%) results in the precipitation of a soft carbide phase [101-103]. A major drawback of carbides formed in the ternary Fe-Al-C system is their fast coarsening kinetics at temperatures exceeding 500 °C [88]. In quaternary and higher component iron aluminides containing carbides the yield strength at 650 °C can be increased by a factor of two in Fe-26Al-(2-4)M-1C (M=Ti, V, Nb, Ta) in contrast to binary Fe-26Al (σ_y=125 MPa) [96]. Among them alloys containing niobium show the highest yield strength of 340 MPa in Fe-26Al-4Nb-1C at 650 °C. The introduction of molybdenum and tungsten containing carbides results in almost similar improvements of the yield strength at 650 °C [97]. The ternary Fe-25Al-2Nb was already discussed in Chapter “solid-solution hardening” and can be transformed by appropriate heat treatment into a two-phase microstructure (FeAl matrix and C14 Fe_2Nb Laves phase) [68][104]. The Fe_2Nb Laves phase shows much faster coarsening kinetics than carbides and the volume fraction of precipitates is smaller compared to Fe-26Al-4Nb-1C. Hence, the yield strength at 650 °C is on a lower level (σ_y=200 MPa) [68]. In the Fe-Al-Zr system the solubility of zirconium in the FeAl matrix is much smaller (<0.1 at.% [105]) than that of niobium (at least 0.8 at.% [84]). This results in higher volume fractions of Laves phase when substituting niobium with zirconium and also higher levels of strength at all temperatures [87]. In general, fine-scaled and evenly distributed precipitates are favorable for high strength and can be achieved for example through thermo-mechanical processing.

3.2. The choice of alloy compositions

The considerations, which were made to choose promising alloys that can substitute for established materials in turbochargers, are based on the following demands: The alloys shall have a low density to achieve a low weight of the whole turbocharger and if rotating structural

parts are considered the centrifugal forces are reduced at the same time. Hence, a high-strength / low-density ratio is beneficial. From this point of view the aluminum content should be as high as possible. An upper bound for the concentration of aluminum is given at 40 – 41 at.% Al where the brittle to ductile transition temperature (BDTT) increases sharply (see Figure 3.5).

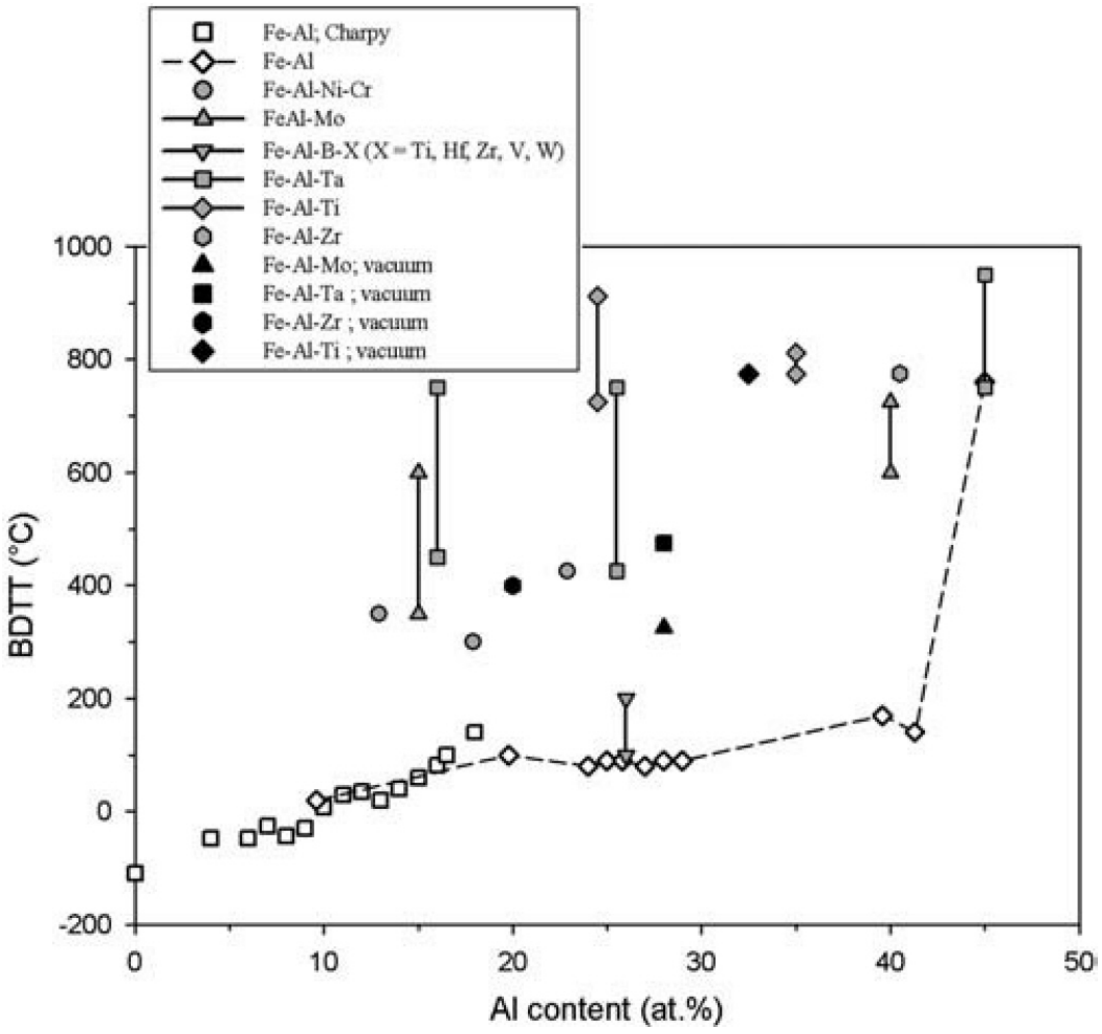

Figure 3.5: BDTT of binary and higher-order Fe–Al-based alloys [3].

Moreover the intrinsic ductility at room temperature decreases significantly beyond this aluminum concentration [106]. The lower bound of aluminum content is set at about 25 at.% aluminum, because the formation of the first intermetallic phase (Fe_3Al) in the binary phase diagram is given here. Due to the formation of an ordered lattice structure a higher strength is given in the intermetallic phase at elevated temperatures in contrast to the disordered solid-solution at lower aluminum contents [30]. This leads also to a reduced dislocation mobility, which results in brittleness of "ordered" intermetallics at room temperature. This relationship

is intrinsic for all intermetallics and exemplary shown in Figure 3.6 for binary iron aluminides.

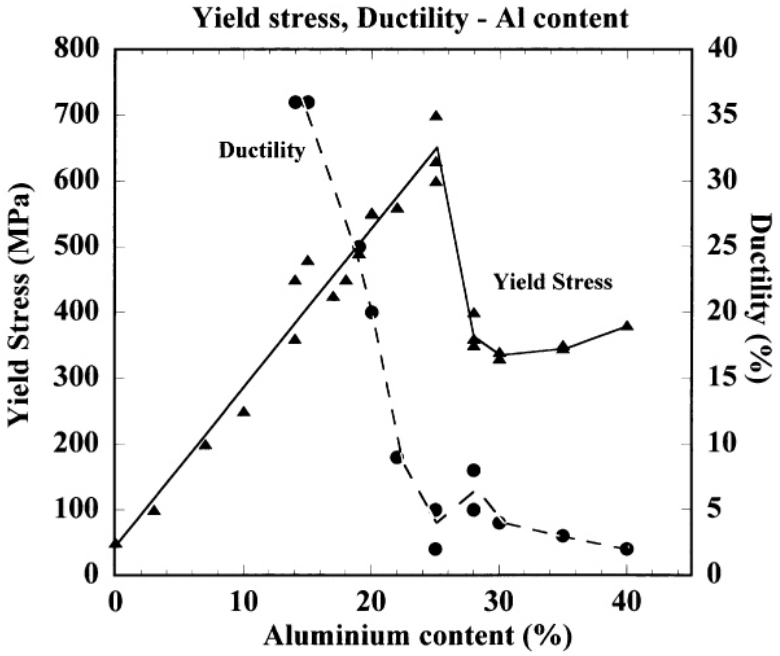

Figure 3.6: Variation of yield stress and ductility of polycrystalline, as-cast or annealed Fe–Al alloys as a function of aluminum content [107].

Consequently the alloys of interest are in the range of 25 – 40 at.% aluminum and three alloys containing 27, 33, and 39 at.% aluminum were fabricated for this work. Furthermore, it can be seen in Figure 3.5 that alloying with additional elements does not lower the BDTT. In general alloying rather results in an increase of the BDTT in FeAl. For this reason only micro-alloyed FeAl alloys were investigated in the present thesis. The chosen micro-alloying elements niobium, zirconium, carbon, and boron are mainly present in the precipitated state in interdendritic regions to keep the FeAl matrix as ductile as possible and to prevent grain coarsening at high temperatures. Alloying with carbon and boron was also found to be beneficial for improving impact toughness [108]. This concept of alloying was already successfully demonstrated on other micro-alloyed iron aluminides [109] and will be further discussed in Chapter 3.3. Beyond the mentioned mechanical properties also the oxidation behavior is an important issue that has to be considered. Depending on the structural parts of the turbocharger they can be exposed to hot air and exhaust fumes up to 1050 °C, for example turbine housing and guide vanes. Iron aluminides possess an intrinsically high oxidation resistance due to the formation of slow growing aluminum oxide which seems to make them a prime choice for such applications. Details on formation mechanisms will be discussed further in Chapter 4. From the industrial point of view it is also important to keep the raw material

and processing costs on a low level. The raw material prices for iron and aluminum are far below the cost for nickel based alloys, high alloyed steels (such as P92), and titanium aluminides which are established alloys in applications, where high strength at elevated temperatures is required. Also a near net shape fabrication in air or under an argon hood by investment or centrifugal casting seems to be feasible for iron aluminides in contrast to titanium aluminides and Ni-based super-alloys, as demonstrated by the project partners.

3.3. Characterization of the "as-cast" state

The initial condition of the FeAl alloys for all investigations is the as-cast state.. Additional heat treatments were carried out prior to some of the creep experiments and are described in detail in the corresponding Chapter 6. The chemical compositions of the alloys, which are manufactured as described in Chapter 2, are given in Table 3.1. The measurement accuracy relates to average conditions and is: Al ±0.2, B ±0.0009, C ±0.008, Nb ±0.005 and Zr ±0.002, all numbers are given in at.%.

Table 3.1: Chemical composition of alloys in at.%.

Alloy	Fe	Al	Nb	Zr	C	B
Fe-27Al	bal.	26.6	0.39	0.19	0.39	0.07
Fe-33Al	bal.	33.4	0.40	0.19	0.41	0.07
Fe-39Al	bal.	39.0	0.40	0.19	0.42	0.07

The amount of micro-alloying elements was chosen to be constant in all alloys for establishing almost the same amount of precipitates and to yield comparability of the FeAl matrix phases between the alloys. The Al content is in the desired range where the intermetallic phases appear and the Al content is steadily increased by about 6 at.% from alloy to alloy. Hence, the densities of the alloys are decreasing at higher aluminum contents (see Table 3.2).

Table 3.2: Averaged Archimedean densities of investigated alloys.

Alloy	Density [g/cm³]
Fe-27Al	6.58 ±0.03
Fe-33Al	6.30 ±0.04
Fe-39Al	6.04 ±0.03

In most micrographs no porosity or cavities were found. The iron aluminide alloys in the "as-cast" condition show a dendritic structure with a secondary dendrite arm spacing (SDAS) estimated to be essentially constant in all alloys (see Figure 3.7).

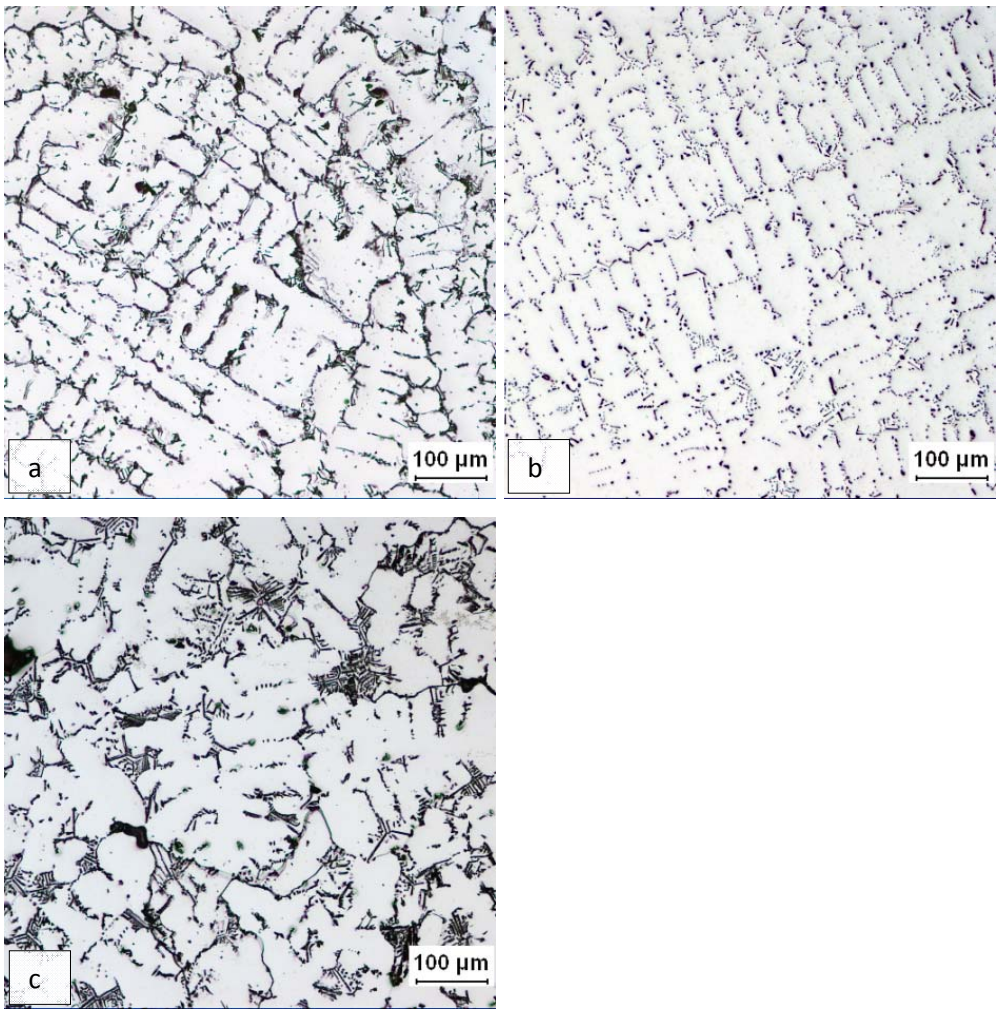

Figure 3.7: Microstructure of the „as-cast" state imaged by light microscopy after "Kroll" etching a) Fe-27Al b) Fe-33Al c) Fe-39Al.

The SDAS has been determined by using the linear intercepts of boundaries method, which is exemplarily shown in Figure 3.8.

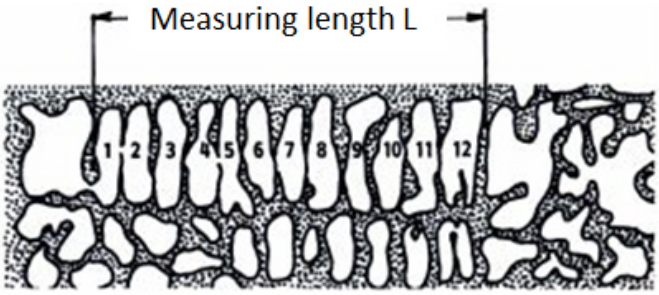

Figure 3.8: Determination of the SDAS from a cross-section (schematic) [110].

The SDAS is calculated as follows:

$$SDAS = \frac{L}{n_D \cdot V} \tag{3.2}$$

L: *Measuring length*

n_D: *Number of dendrites within the measuring length*

V: *Magnification of image*

The lengths of at least 100 dendrite arms were measured. The averaged SDAS are listed together with associated standard deviations in Table 3.3.

Table 3.3: Averaged SDAS of alloys.

Alloy	SDAS [µm]	Standard deviation [µm]
Fe-27Al	35	11
Fe-33Al	36	4
Fe-39Al	29	8

The averaged SDAS are on the same level for all alloys and almost invariant across the samples due to the use of pre-heated chill molds during casting. The main part of the micro-alloying elements forms a eutectic, which is mainly located between the dendrite arms. The characteristic plate like morphology of the eutectic is shown exemplarily in Figure 3.9 for Fe-33Al. The morphology was exposed by a selective etching of the FeAl matrix phase via electro polishing.

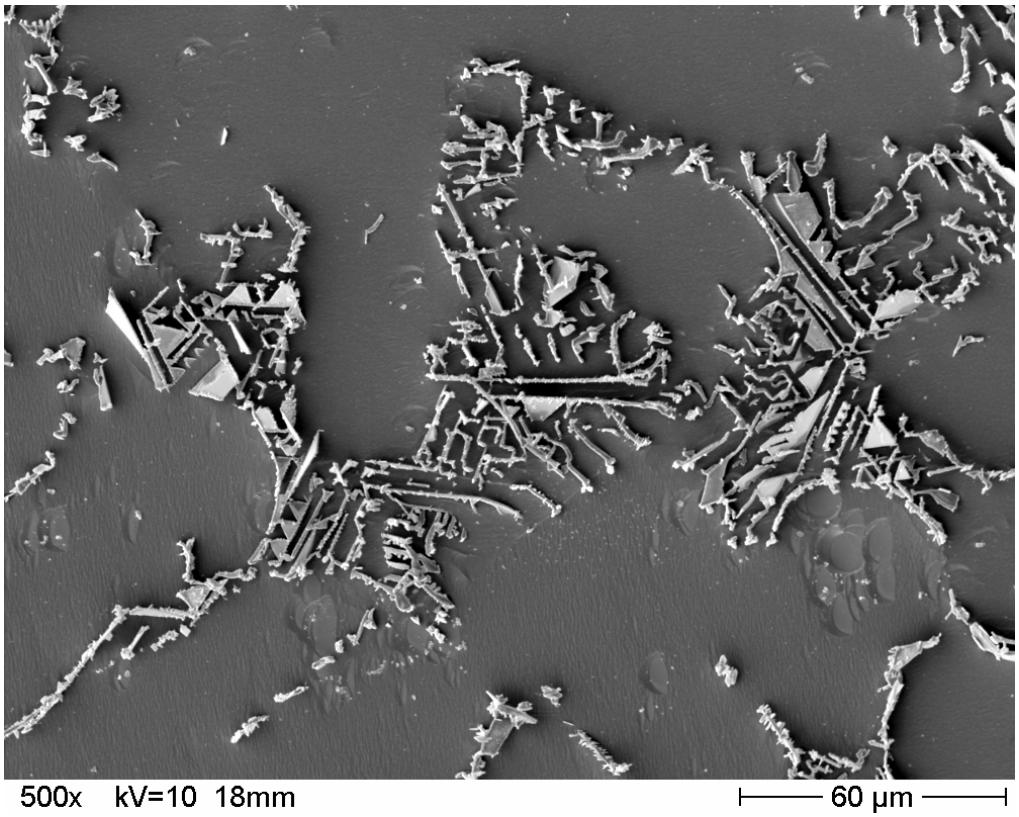

Figure 3.9: Fe-33Al, selective etching of the matrix phase (SEM-SE image).

The amount and shape of precipitates were quantitatively analyzed in cross-sections of identically polished and etched samples. In doing so, 30 randomly chosen pictures of each alloy were recorded at identical magnification (500x) in an optical microscope.

For digital analysis the matrix phase and precipitates were separated by setting a threshold value in levels of grey by analySIS software. In the following quantification, the areal fraction is set equal to the volume fraction (Delesse-principle) [111], because a preferred orientation of the precipitates is not given here. The averaged values with standard deviations are listed in Table 3.4.

Table 3.4: Volume fraction of precipitates in investigated alloys.

Alloy	Volume fraction of precipitates [%]
Fe-27Al	1.5 ±0.4
Fe-33Al	1.9 ±0.6
Fe-39Al	2.2 ±0.4

The volume fraction of precipitates increases with higher aluminum contents, at the same time the alloying elements in solid-solution have to decrease, since the absolute concentrations of alloying elements are on the same level in all alloys. Further, the shape (circumference to area

ratio) of the precipitates was analyzed, because deviations would result in different densities of phase boundaries (FeAl-matrix/precipitate), which can play an important role in further investigations. The precipitates were classified into ten categories from circular to disc-shaped morphologies and each category is labeled in its specific color (see Figure 3.10).

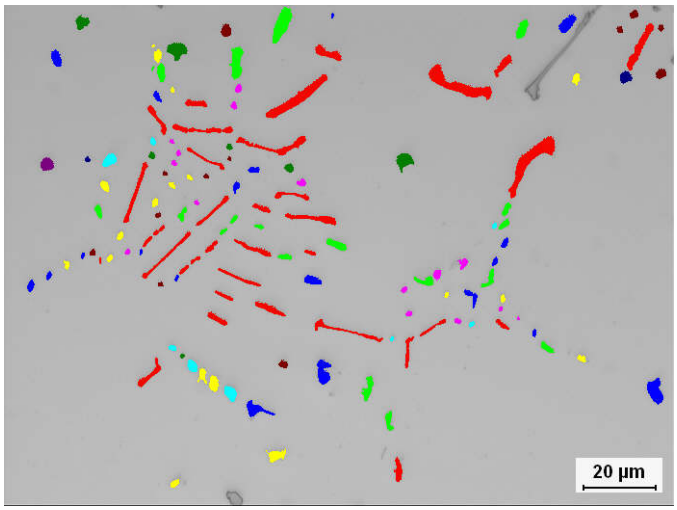

Figure 3.10: Cross-section of Fe-33Al imaged by light microscopy with superimposed particle analysis.

Precipitates, which are not completely within a picture, were not used for shape analysis. The circumference to area ratio of the precipitates was found to be on the same level in each alloy, thus the precipitates are assumed to have the same shape. Chemical analysis of the precipitates was done by TEM equipped with an EDX system. The EDX analysis clearly shows that all micro-alloying elements (niobium, zirconium, carbon, and boron) are present in the precipitates. An example is shown in Figure 3.11 for Fe-39Al.

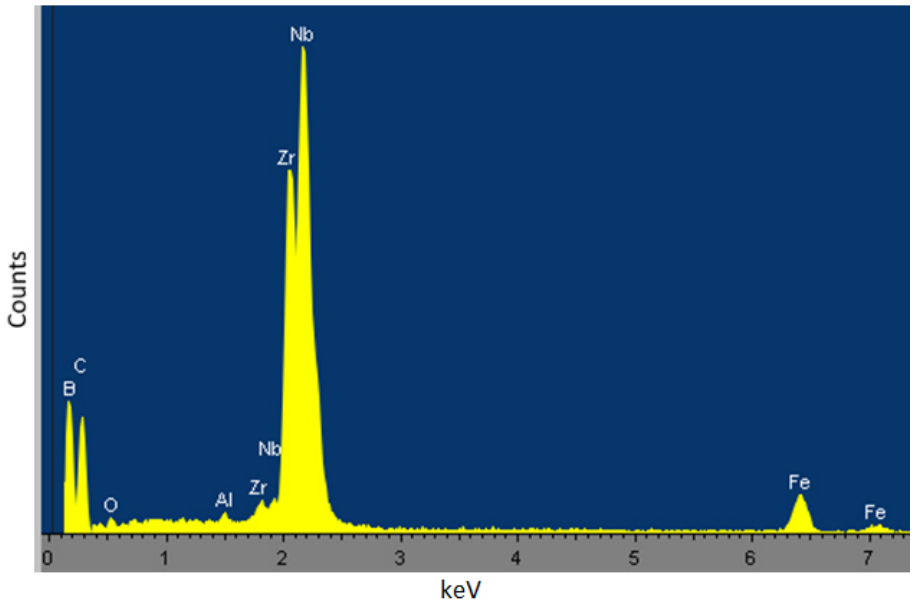

Figure 3.11: EDX analysis of a typical precipitate in Fe-39Al.

The residual amounts of iron and aluminum might stem from analyzing the surrounding matrix or may be also present in low concentrations in the precipitated state. The solubility of niobium at aluminum contents in the range of 27 – 39 % at.% is known to be at least 0.8 at.% in the ternary Fe-Al-Nb system [84], whereas the solubility of zirconium is constantly below 0.1 at.% in the ternary system Fe-Al-Zr [105]. Moreover, the high concentration of carbon and boron in the precipitates gives clear evidence of the formation of carbides and borides. In addition, the precipitates are thermodynamically very stable and did not show any coarsening effects after 550 h at 1000 °C in cross-sections investigated by SEM. This will be further discussed in Chapter 4. In order to investigate whether the precipitates form a contiguous network inside the FeAl matrix, EBSD orientation mappings were carried out. The mappings revealed that precipitates are arranged in colonies with same crystallographic orientation (see Figure 3.12).

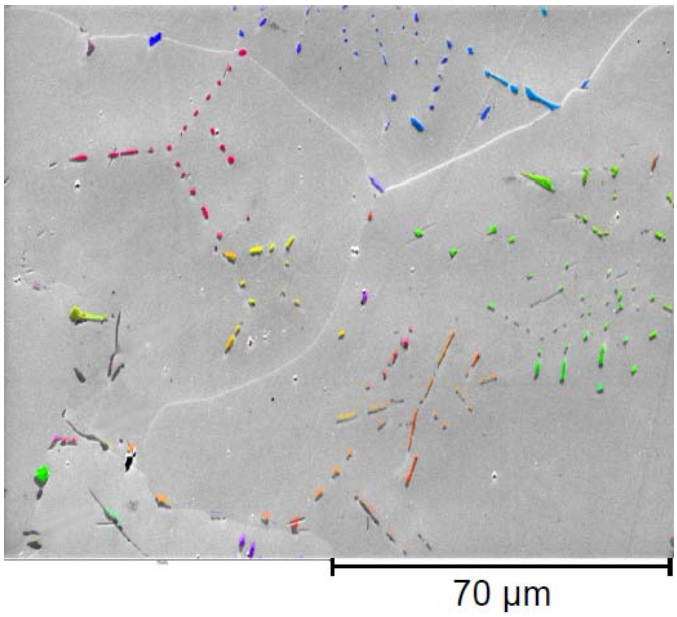

Figure 3.12: Fe-39Al (SEM-SE image) with superimposed orientation mapping of the precipitates (same color indicates same crystallographic orientation).

It can be concluded that each colony grew from the same nucleus and for Fe-39Al the precipitates are contiguous up to a range of about 100 µm. Consequently, the extent of the colonies is increased with increasing volume fraction of precipitates (see Table 3.4).

The order of the matrix phase can be different (for example, $D0_3$, B2 or disordered A2). The phase transition temperatures of the matrix phase were analyzed by DSC measurements. The $D0_3$-B2 and B2-α transitions are second-order phase transitions and the phase transition temperatures are estimated from peak maxima as usually done in literature [16]. The matrix phase at room temperature is B2 for Fe-39Al and Fe-33Al: the DSC traces in Figure 3.13 do not show any indication of phase transitions except the B2-α phase transition.

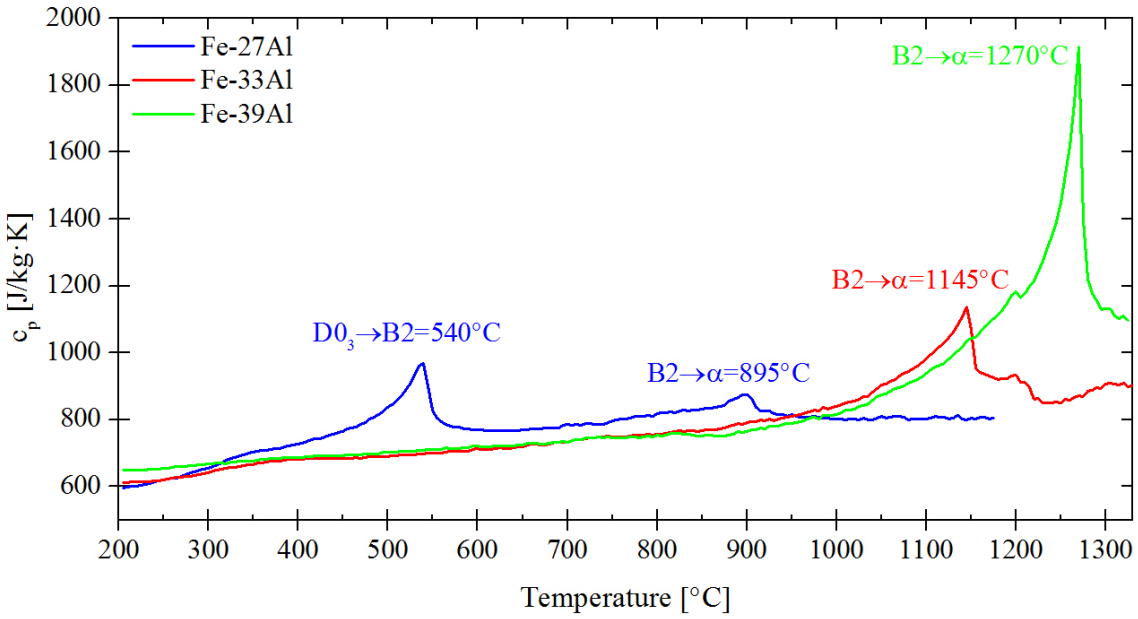

Figure 3.13: DSC traces of Fe-27Al, Fe-33Al, and Fe-39Al (cooling curve at a rate of 10 K/min).

The order in the B2 phase regime increases with aluminum content, whereas the highest amount of order is achieved at the stoichiometric composition of FeAl. The integral intensity of the B2-α phase transitions is increasing with Al content (see Figure 3.13). In contrast, in alloys with 27 at.% Al the crystal structure at room temperature may consist of the ordered phases $D0_3$, B2, or of a disordered solid-solution (A2) depending on prior cooling conditions [21]. In the present case, a strong endothermic reaction peak is observed in Fe-27Al at 540 °C in the cooling curve. A corresponding peak with nearly the same integral intensity, shifted to slightly higher temperatures, is visible in the heating curve indicating that a reversible phase transitions occurs (see Figure 3.14).

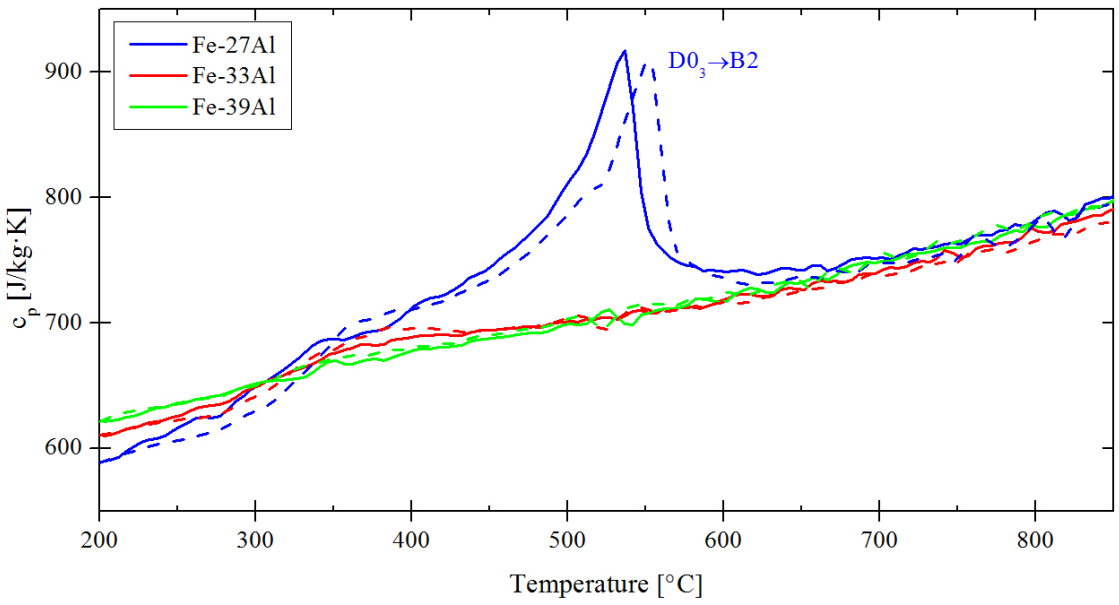

Figure 3.14: DSC traces of Fe-27Al, Fe-33Al, and Fe-39Al (cooling curve: straight line; heating curve: dashed line) at a rate of 10 K/min.

This suggests the presence of a nearly fully $D0_3$-ordered phase for the alloy containing 27 at.% Al at room temperature in the "as-cast" state. Also the electron diffraction patterns that were obtained from multiple zone axes (Figure 3.15a-c) for Fe-27Al showed the characteristic superlattice spots for $D0_3$-order $(\bar{1}1\bar{1})$, $(11\bar{1})$, (111), $(\bar{1}\bar{1}1)$ and can be observed in the pattern obtained from the [011] zone axis (Figure 3.15b) [112].

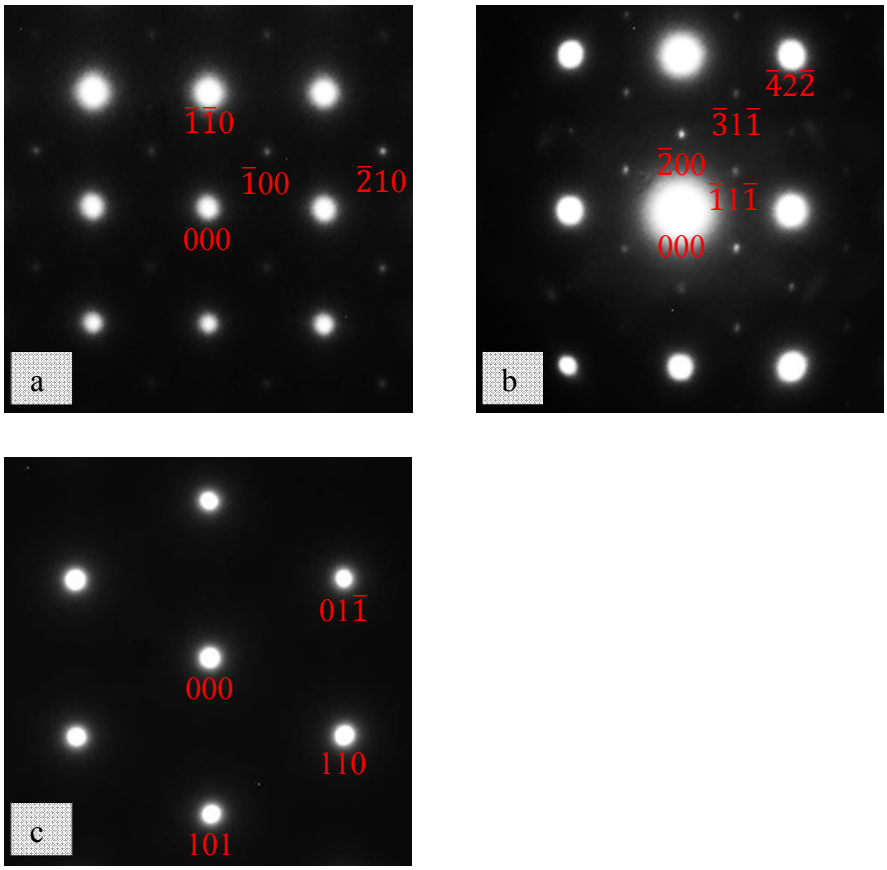

Figure 3.15: TEM diffraction patterns of Fe27Al a) Zone axis [001] *b) Zone axis* [011] *c) Zone axis* [$\bar{1}$11]. *The weak spots can be clearly indexed as superlattice peaks stemming from $D0_3$-order.*

The influence of the micro-alloying elements on the phase transition temperatures is compared to binary iron aluminides in Table 3.5.

*Table 3.5: Phase transition temperatures of investigated alloys and binary iron aluminides *[16].*

	Phase transition temperatures [°C]			
	DO_3 - B2		B2 - α	
Alloy	**Heating**	**Cooling**	**Heating**	**Cooling**
Fe-26.6Al-(Nb,Zr,C,B)	550	540	910	895
	555	540	910	895
Fe-26.0Al *	545		821	
Fe-27.0Al *	543		868	
Fe-33.4Al-(Nb,Zr,C,B)			1155	1145
			1150	1140
Fe-32.5Al *	440		1109	
Fe-34.2Al *			1156	
Fe-39.0Al-(Nb,Zr,C,B)			1275	1270
			1275	1270
Fe-38.4Al *			1258	
Fe-39.8Al *			1288	

The phase transition temperatures are shifted to higher temperatures in the heating curves in contrast to cooling curves because of the hysteresis behavior. The gap of phase transition temperatures between heating and cooling curves becomes smaller at lower cooling rates, due to a longer period of time available for a microstructure to approach thermodynamic equilibrium. The phase transition temperatures in alloys containing 39 at.% Al are in good agreement with binary iron aluminides and hence, an effect of micro-alloying elements is negligible. The phase transition temperatures of the B2-α transition of the investigated alloys are shifted towards higher temperatures in contrast to binary FeAl, which is most pronounced in Fe-27Al. The $D0_3$-B2 phase transition, which is only present in Fe-27Al of the investigated alloys, is also shifted slightly up to higher temperatures in contrast to binary Fe-27Al. In general, phase transition temperatures are influenced by alloying elements and their concentration within the matrix phase. The solubility of each alloying element is also influenced by the presence of other elements and cannot be quantified in the investigated alloys. However, from ternary phase diagrams Fe-Al-X (X=Nb, Zr, C, B) the following solubilities are known: carbon has a solubility of less than 50 wt. ppm in Fe-18Al [113] and hence, an influence of the phase transition temperature is assumed to be zero. The influence of boron is also negligible because of its low overall concentration of 0.07 at.% in the alloys and its high concentration in the precipitates (see Figure 3.11). Finally, the solubility of zirconium is similarly low (<0.1 at.% [105]) and its influence is assumed to be negligible, too. Hence, the potential candidate for raising the phase transition temperatures of the FeAl matrix phase in the investigated alloys is niobium. The solubility of niobium in FeAl is at least 0.8 at.% in alloys containing 27 up to 39 at.% Al [84] and 0.5 at.% niobium in Fe-26Al-0.5Nb increases the B2-α phase transition temperature by 45 K [71]. As discussed earlier in this Chapter the highest concentration of niobium in the FeAl matrix phase is present in Fe-27Al and hence, a stronger increase of the phase transition temperature can be found in this alloy.

4. Oxidation behavior

4.1. Fundamentals of oxidation

Oxidation is a special form of high temperature corrosion [114]. The alloys investigated here were exclusively oxidized in laboratory air and therefore other types of high-temperature corrosion, such as carbonization, nitridation, and sulfidation will not be treated here. In general, the term “oxidation” is used, if a material reacts with oxygen at higher temperatures (>500 °C) by forming an oxide [115]. Most high temperature applications operate in oxygen containing environments and, hence, oxidation is the most important form of high temperature corrosion. The reaction of a metal (M) with gaseous oxygen (O) is given by Equation 4.1:

$$x \cdot M + \frac{y}{2} \cdot O_2 \leftrightarrow M_x O_y \tag{4.1}$$

The equilibrium constant (K) for this reaction at a given reaction temperature is related the partial pressure of oxygen (law of mass action) [116]:

$$K = \frac{a_{M_x O_y}}{a_M^x \cdot P_{O_2}^{y/2}} \tag{4.2}$$

$a_{M_x O_y}$: *Thermodynamic activity of oxide*

a_M: *Thermodynamic activity of metal*

P_{O_2}: *Partial pressure of oxygen*

As the reactants metal (M) and oxide (M_xO_y) are solid, their thermodynamic activities can be assumed to be unity [117]. Values of K need to be determined for each reaction at a specific temperature experimentally. The equilibrium constant *K* is used to calculate the Gibbs free energy of the chemical reaction:

$$\Delta G = -\mathrm{R}T \cdot ln(K) \tag{4.3}$$

ΔG: *Gibbs free energy*

R: *Avogadro constant*

The second law of thermodynamics states that the Gibbs free energy change will have the following implications: $\Delta G < 0$, spontaneous reaction; $\Delta G = 0$, equilibrium; $\Delta G > 0$, impossible reaction. The free energy of formation for various oxides as a function of temperature is given in the Ellingham-Richardson diagram (see Figure 4.1).

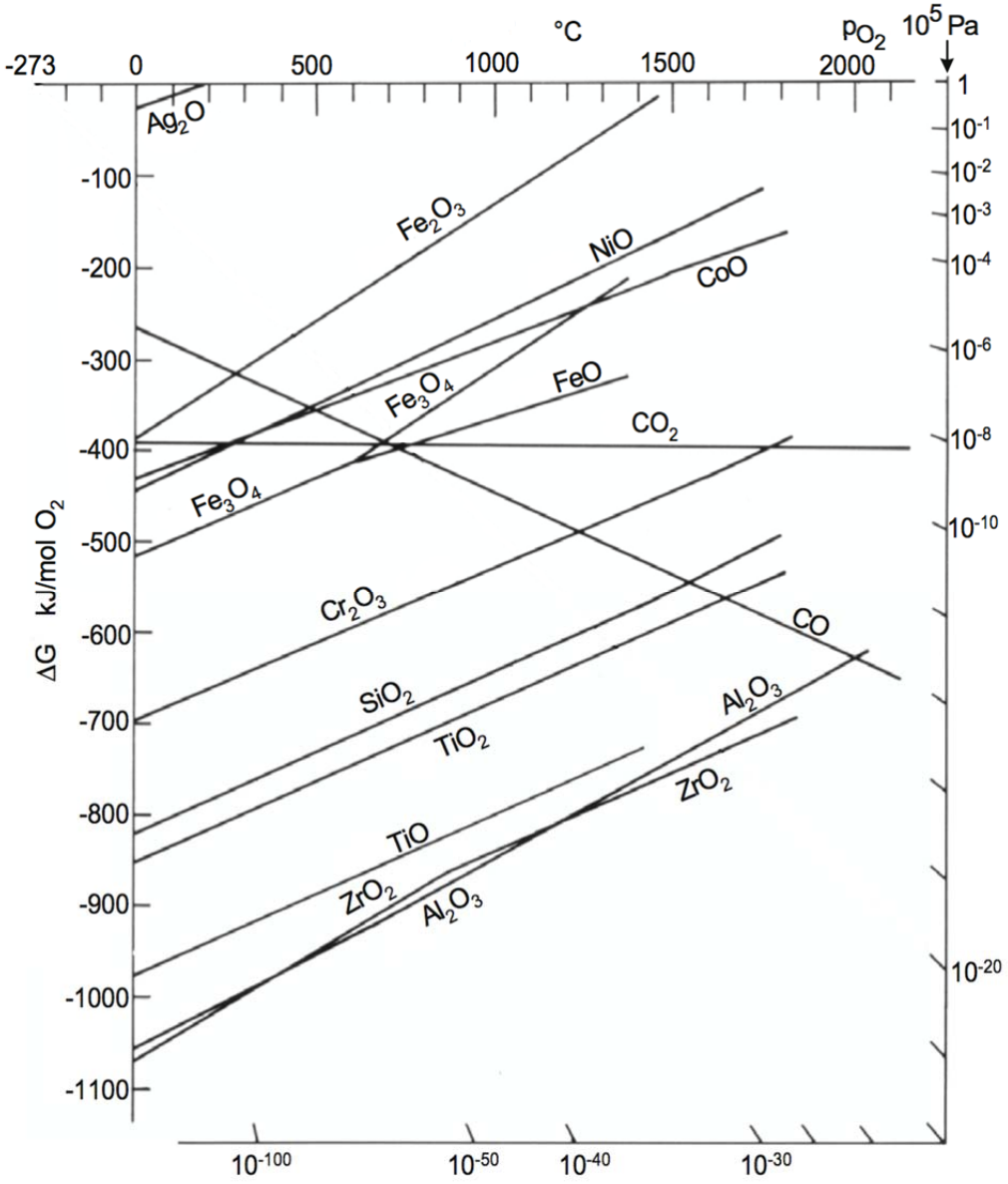

Figure 4.1: Ellingham-Richardson-diagram of several oxide reactions [114].

The lower the value of ΔG, the higher is the thermal stability of the oxide and the driving force for its formation. The first-order derivative of ΔG with respect to temperature in Figure 4.1 reflects the influence of change in entropy:

$$\frac{d(\Delta G)}{d(T)} = -\Delta S \tag{4.4}$$

This results in lower stability of oxides at higher temperatures.

Thermodynamic parameters only predict whether under certain conditions of temperature and partial pressure of oxygen, oxide formation is possible or not. Hence, thermodynamic aspects cannot predict the oxidation behavior alone; kinetic aspects also need to be considered. In

contrast to explosives, the kinetics should be as slow as possible to delay the consumption of the metal by oxygen resulting in oxides. The kinetics of oxidation can be analyzed by measuring the mass change of a specimen (normalized to the specimen surface) over time or by measuring the thickness of the growing oxide scale in time intervals. Since the analysis of scale thickness is experimentally complex, thermo-gravimetric analysis of weight change is preferred in general. Moreover oxidation kinetics, such as pesting, can only be quantified by thermo-gravimetric analysis (see Figure 4.2). The mass change of a specimen with time is related to its reaction with oxygen and does result in different behavior (see Figure 4.2), which are a result of the interaction of the metal/oxide interface and diffusion processes.

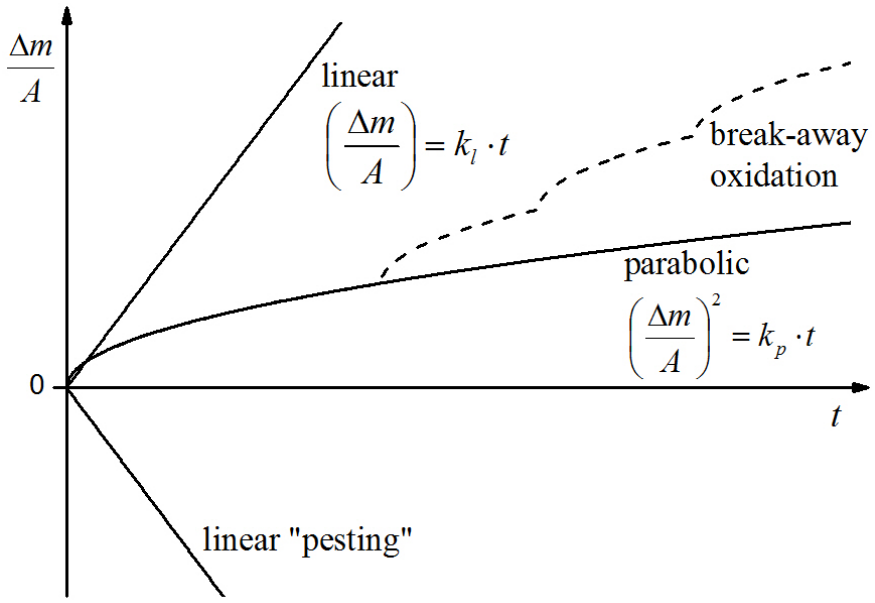

Figure 4.2: Idealized kinetic rules of mass change over time for various oxidation processes.

An optimal oxidation resistance is given by a parabolic mass gain over time, due to the slowest mass change during oxidation (see Figure 4.2). The theory of parabolic mass gain is based on C. Wagner [118] and on the following assumptions [119]:

- The oxide scale is dense and perfectly adherent
- Diffusion of ions through the oxide scale is the rate controlling process
- Thermodynamic equilibrium exists at both boundaries: metal/oxide and oxide/gas
- The oxide scale shows only small deviations from stoichiometry and hence, the diffusion fluxes are constant within in the scale
- Thermodynamic equilibrium is established locally throughout the scale

- The solubility of oxygen in the metal can be neglected

In the early stages of oxidation an oxide scale is formed on the metal surface and subsequent scale growth occurs either by diffusion of metal and/or oxygen ions through the oxide scale. This is of importance if the oxide scale grows at the interface metal/oxide (preferential oxygen-ion diffusion thorough the oxide scale) or if the oxide scale grows at the interface oxide/gas (preferential metal-ion diffusion thorough the oxide scale). The oxidation rate is decreasing with time as the oxide scale becomes thicker and hence, diffusion paths become longer (Tammann's law):

$$X^2 = k_p' \cdot t \tag{4.5}$$

X: *Oxide scale thickness*

k_p'*:* *Oxide scale related parabolic rate constant*

As mentioned above, the continuous measurement of the oxide scale thickness is experimentally difficult and the mass gain can be recorded more easily. The parabolic law from Equation 4.5 can also be related to mass gain by knowing the mass and the density of the formed oxide:

$$k_p = k_p' \left(\frac{X \cdot A}{\Delta m}\right)^{-2} = k_p' \left(\frac{m_{ox}}{\rho_{ox} \cdot \Delta m}\right)^{-2} \tag{4.6}$$

k_p*:* *Mass gain related parabolic rate constant*

A: *Surface of specimen*

Δm: *Mass gain*

m_{ox}*:* *Mass of oxide*

ρ_{ox}*:* *Density of oxide*

Using k_p, the parabolic mass gain can expressed in analogy to Equation (4.5):

$$\left(\frac{\Delta m}{A}\right)^2 = k_p \cdot t \tag{4.7}$$

The fact that oxidation is diffusion controlled and, hence, related to temperature, the temperature dependence of k_p can be expressed by an Arrhenius law:

$$k_p = k_{p0} \cdot e^{-\left(Q/RT\right)} \tag{4.8}$$

k_{p0}*:* *constant pre-factor*

Q: *Activation energy of rate determining diffusion process during scale growth*

Diffusion of ions through the oxide scale is the only way for metal or oxygen to react with each other and hence, Q can be usually related to activation energy for self-diffusion Q_{SD}. However, oxide growth rates cannot be calculated simply by self-diffusion rates because structural defects in the oxide scale (especially grain boundaries) provide faster diffusion paths for ions, which have to be considered. Some k_p values for metals which exhibit parabolic mass gain over time and their dependence on temperature are given in Figure 4.3.

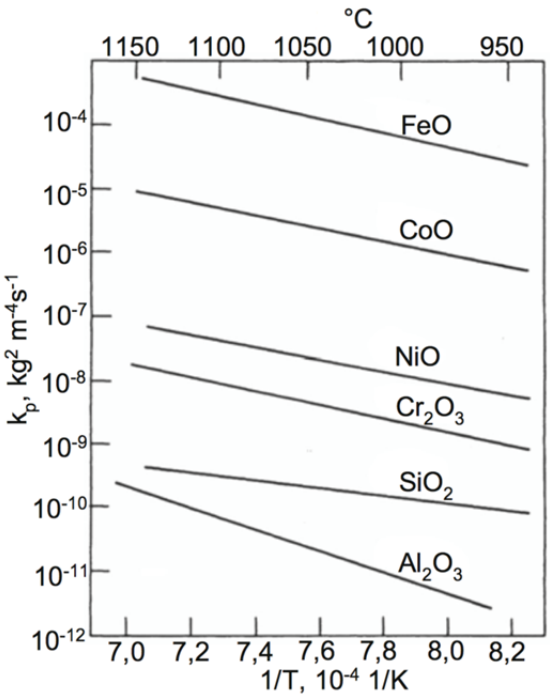

Figure 4.3: Temperature dependence of selected k_p-values of oxides (exhibiting nearly parabolic mass gain over time) [114].

From Figure 4.3 it now can be concluded that the formation of Al_2O_3 is desirable for high temperature applications because of the slow kinetics, and as already shown, Al_2O_3 has a very low evaporation rate at low oxygen partial pressures (see Figure 4.1).

The oxidation behavior of materials in practice is often more complex as it could be explained by only regarding thermodynamic and kinetic aspects. After an initial oxidation by the parabolic law, the mass gain can abruptly raise due to cracking and spallation of the former protective oxide scale. The tendency whether an oxide is susceptible to scale spallation during isothermal oxidation is related to the ratio between volume of an oxide and the volume of the metal that formed the oxide. This ratio is called Pilling-Bedworth ratio (PBR). Most oxides have PBR's > 1 (except alkaline and alkaline earth metals), which results in growth stresses parallel to the metal/oxide interface (compressive stress in the oxide and tensile stress in the

metal). Spallation of the oxide scale occurs when the stress conditions at the interface (metal/oxide) exceed a critical value. This process will be repeated continuously and is called "break-away oxidation" (see Figure 4.2). Here again Al_2O_3 scales are desirable because of their low PBR of 1.3 [120]. For comparison Fe_2O_3, Fe_3O_4, and Cr_2O_3 all exhibit higher PBR's of 2.1 [117]. When oxides exhibit even higher PBR's such as Ta_2O_5 and Nb_2O_5 (which exhibit PBR's of 2.6 and 2.5, respectively [121]), a parabolic mass gain is not given at any time. Oxygen then has a continuous access to bare metal and oxidation kinetics are much faster resulting in linear mass gain over time (see Figure 4.2). A linear loss of mass can be observed when volatile oxides are formed such as V_2O_5 and MoO_3. This phenomenon is called "pesting" and can often be observed at intermediate temperatures.

Interfacial stresses between metal and oxide resulting in spallation become an even more critical issue during cyclic exposure, which reflects in most cases the real circumstances of applications. The stress conditions at the interface metal/oxide are influenced during cyclic conditions by:

- Differences in coefficients of thermal expansion of oxide/metal
- Difference in temperature ΔT of furnace and cool-down temperature
- Cool-down rate during cool-down procedure
- Thickness of the oxide scale (heat flow is reduced with increasing thickness of the oxide scale)
- Oxide scale adherence (can be reduced by cavities or by depletion of the oxide forming metal in alloys)
- Lattice mismatch of metal/oxide

A reduction of stresses inside the oxide scale is only rarely possible by plasticity even at high temperatures. The Peierls stress for dislocation movement in oxides is very high due to their covalent and ionic bond character and the "von Mises-criterion" of 5 linear independent slip systems is rarely fulfilled. Thus, mechanical stresses result in cracking and spallation of the oxide scale. During cyclic oxidation experiments the specimens are put into a furnace heated to certain temperature, and after periods of time the oxidation is interrupted by removing the sample from the furnace and giving it a cool-down procedure. The mass gain is recorded after each cool-down and plotted the same way as mentioned for isothermal conditions.

Beyond the mass gain by the growth of an oxide scale on top of the metal surface the occurrence of internal oxidation is also possible in some cases. Diffusion of oxygen into the

bulk material and subsequent formation of oxides determines the mechanism of internal oxidation. Possible diffusion paths for oxygen are diffusion through the bulk (volume) of the sample and along grain and phase boundaries. These diffusion paths are basically akin to those responsible for oxide scale growth on the surface and, hence, a modified parabolic rate law to determine the depth of internal oxidation is applicable here, too.

$$IOD^2 = k_I \cdot t \tag{4.9}$$

IOD: *Internal oxidation depth*

k_I: *Internal oxidation related parabolic rate constant*

As it holds for the parabolic rate law for scale growth, this law is only applicable if diffusion through the oxide scale and the bulk material is the rate controlling process for oxidation.

4.2. Oxidation behavior of iron aluminides

Since the early 1930s iron aluminides are known to exhibit an excellent oxidation and corrosion resistance [122-128]. In [122], a threshold value of about 19 at.% aluminum was determined which led to comparable oxidation rates at 900 °C for binary iron aluminides containing 19 to 40 at.% aluminum due to the formation of a dense Al_2O_3 scale. This threshold concentration of Al depends on oxidation temperature. In [129] the Al threshold concentration was found to be 14 at.% at 800 °C. At even lower aluminum contents the partial formation of iron oxide nodules was observed [129]. For alumina formers, oxidation kinetics depends on the Al_2O_3 modifications formed on the surface during oxidation. These can be either metastable such as γ and θ or the slowest growing, thermodynamically stable α-Al_2O_3 [130]. For a given temperature a transient formation sequence is usually observed from metastable towards stable alumina, which is controlled by surface chemistry. For example, the decomposition sequence of bohemite (AlO(OH)) heated in dry air has been summarized by Newsome et al. [131]. The transition temperature from θ-Al_2O_3 to α-Al_2O_3 was found to be 1150 °C. Saalfeld gives a comparable temperature of 1100 °C [132]. The corresponding transition temperatures in iron- and nickel aluminides were found to be on a lower level of 900 – 1000 °C [133-135]. This is in good agreement with the drop of k_p-values at oxidation temperatures exceeding approximately 1000 °C for FeAl [123][135][136]. Other authors showed that the formation of another oxide scale that has a corundum-type crystal structure may act as a nucleation site for subsequent formation of α-Al_2O_3, hence suppressing θ-Al_2O_3 growth [137]. An effective way to improve the oxidation behavior in the range of 900 –

1000 °C and below would, thus, be to shift the θ-Al_2O_3 / α-Al_2O_3 transformation to lower transition temperatures.

Several authors demonstrated that small amounts of zirconium to FeAl are beneficial in reducing the k_p-values due to an improvement of the oxide scale adherence [87][138][139]. Along with the addition of 0.05 at.% Zr zirconium in Fe_3Al, also the transition temperature from θ-Al_2O_3 to α-Al_2O_3 decreased slightly from 950 °C to 900 °C [138]. However, the solid solubility of Zr in iron aluminides is very low (<0.1at.% [105]) and alloying beyond that limit was found to be detrimental due to internal oxidation of the Zr-rich Laves phase [87]. Therefore Nb (with a well-known higher solid solubility compared to Zr [84]) and Zr have been chosen together with C and B as micro-alloying additions. This judicious combination has been known to form borides and carbides which also act to improve the mechanical properties by (i) precipitation hardening and (ii) stabilizing a relatively fine grain size [3][21][27][96][109][140][141].

4.3. Results and Discussion

In this Chapter, the implications of the micro-alloying additions on the oxidation resistance of iron aluminide alloys at temperatures ranging from 750 to 1050 °C in ambient air under cyclic conditions are investigated and the oxidation mechanisms, including oxide scale formation and internal oxidation are discussed.

4.3.1. Mass gain

The mass gain during cyclic oxidation was recorded in intervals as described in Chapter 2. The resulting data points are indicated in Figure 4.4 by open and full squares at 750 and 900 °C, respectively.

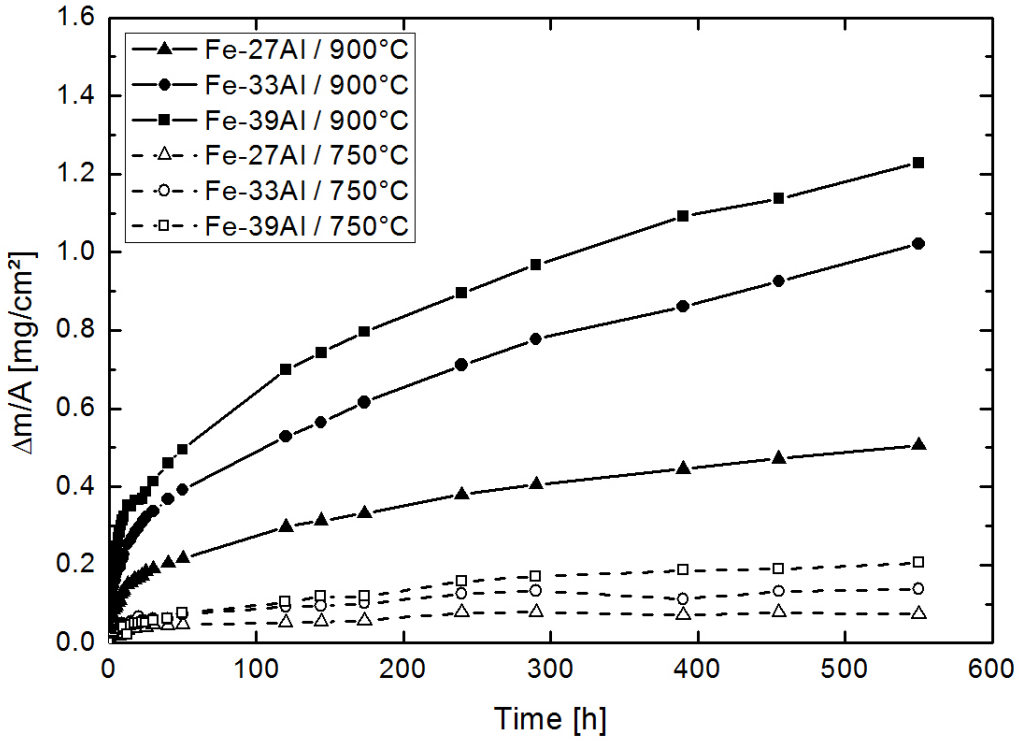

Figure 4.4: Cyclic mass gain vs. time plot, alloys and temperatures as listed in the inset. Data points are indicated by squares, the lines are to guide the eye.

Straight and dashed lines are added to guide the eyes. If the diffusion process in the oxide scale is rate determining for the oxidation, the kinetics can be described by the parabolic rate law (see Equation 4.7). Parabolic rate constants k_p were determined at 750 and 900 °C (see Table 4.1) from the mass gain vs. time plots in Figure 4.4 in the range of 50 to 550 h.

Table 4.1: Oxidation data from cyclic oxidation tests after 550 h of FeAl alloys.

oxidation temperature [°C]	750			900		
Al content of alloy [at.%]	27Al	33Al	39Al	27Al	33Al	39Al
k_p [$g^2 \cdot cm^{-4} \cdot s^{-1}$]	$2.1 \cdot 10^{-15}$	$6.9 \cdot 10^{-15}$	$2.1 \cdot 10^{-14}$	$1.1 \cdot 10^{-13}$	$5.0 \cdot 10^{-13}$	$6.9 \cdot 10^{-13}$
scale thickness [µm]	1.2	1.5	1.4	1.3	5.6	6.1
internal oxidation depth [µm]	13	31	40	48	123	184

At 1050 °C massive spallation occurred for all alloys in form of fragments up to 100 µm in diameter (see Figure 4.5), which is not unusual for iron aluminides in this temperature regime under cyclic conditions [125], so the parabolic rate law, Equation 4.7, is not applicable at these high temperatures.

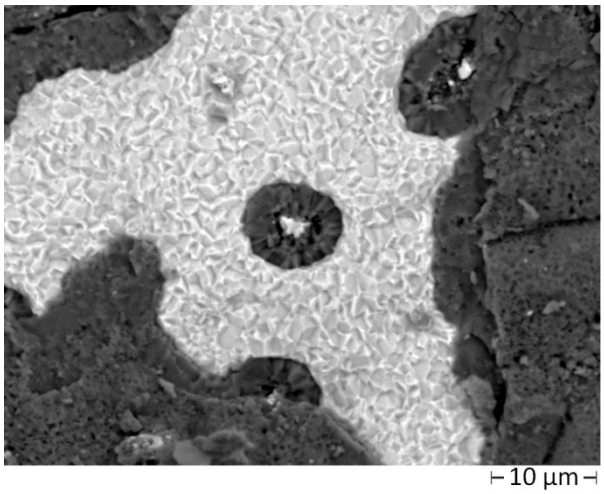

Figure 4.5: Surface of Fe-33Al after 550 h oxidation at 1050 °C (SEM-BSE image). Spallation occurred in the bright areas, there virgin material is visible.

At all exposure temperatures the mass gain is larger in alloys with higher aluminum content. By contrast, binary alloys in this compositional range show only a dependence on exposure temperature and not on aluminum content [122]. The deviations from the latter expected behavior will be discussed subsequently in terms of oxide scale formation and internal oxidation.

4.3.2. Oxide scales

All alloys exhibit a positive mass gain over time due to the formation of Al_2O_3 scales (see Figure 4.6).

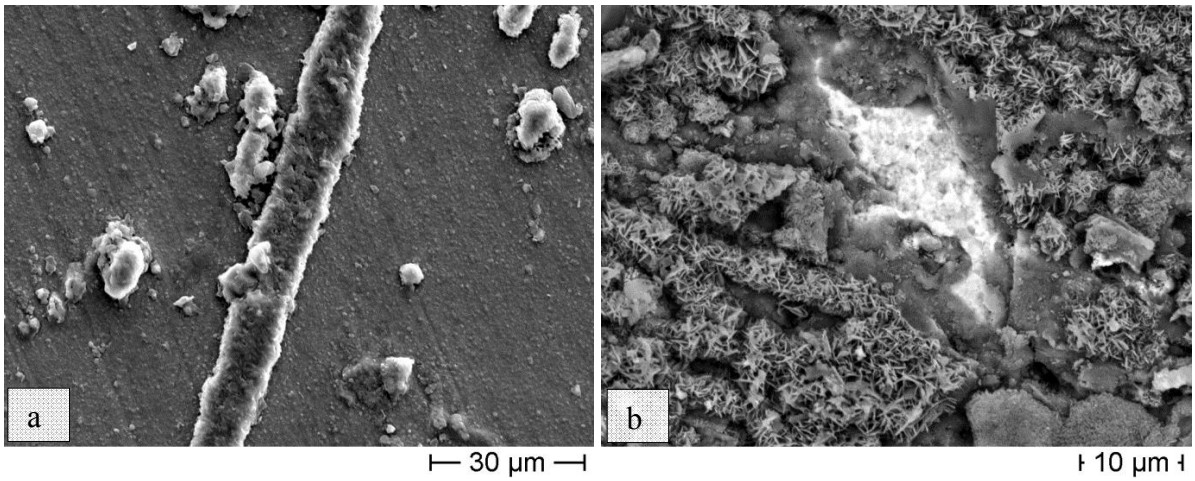

Figure 4.6: Surfaces after 550 h oxidation at 900 °C a) Fe-27Al (SEM-SE image), exhibiting α-Al_2O_3 (flat "epitaxial" growth) exclusively and elevated structures at precipitates b) Fe-39Al (SEM-BSE image), showing α- and θ-Al_2O_3 (whisker-type morphology). As in Figure 4.5, the bright area corresponds to spallation.

No indications for the formation of other oxides have been found. Fe-27Al shows a dense, thus, protective alumina scale at 750 and 900 °C. The scale morphology is shown exemplarily in Figure 4.6a. Locations where precipitates are present at the surface are visible as voluminous elevated structures, whereas the surface was planar prior to oxide scale formation. The flat "epitaxial" growth which covers most of the surface is typical for α-Al_2O_3 on FeAl alloys [123] and this scale morphology can be attributed to the presence of α-Al_2O_3 in this work, too (see Figure 4.7a).

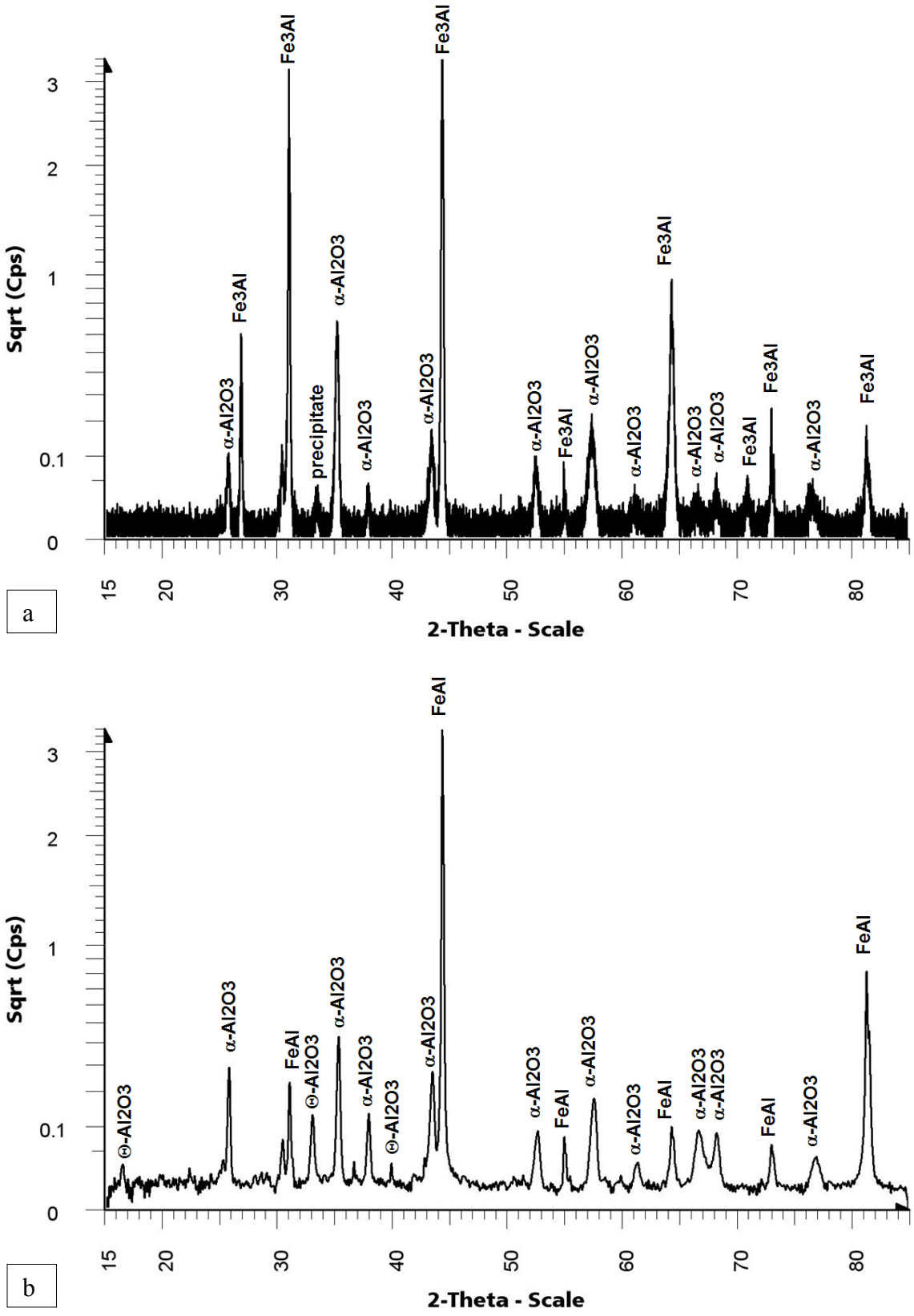

Figure 4.7: X-ray diffraction patterns from the surfaces of oxidized samples (550 h at 900 °C) corresponding to the SEM micrographs in Figure 4.6: a) Fe-27Al b) Fe-39Al.

Oxidation kinetics in binary iron aluminides can become even slower at temperatures higher than 900 °C due to the transition from metastable θ-Al_2O_3 to stable α-Al_2O_3 scales [133][136][142][143], if the higher tendency towards scale spallation can be prevented. Indications for meta-stable Al_2O_3 oxide phases were not found on Fe-27Al, neither at 900 °C nor at 750 °C. At higher aluminum contents (and thus, lower concentration of micro-alloying elements in solid solution, as described in Chapter 3) the partial formation of whisker-type Al_2O_3 needles was observed on top of the α-Al_2O_3 scale, Figure 4.6b. The highest amount of these whisker type Al_2O_3 needles typical for θ-Al_2O_3 [123][136][137][144-146] is present on Fe-39Al. The crystallographic structure of this oxide morphology was confirmed as θ-Al_2O_3 by XRD in this work, too (see Figure 4.7b). The oxide scale on Fe-39Al shows both, the characteristic XRD peaks of α- and θ-Al_2O_3, respectively. The presence of θ-Al_2O_3 results in partial spallation of the oxide scales in chips up to 20 µm in diameter (see Figure 4.6b). Nevertheless, the recorded mass gain over time still appears to follow the parabolic rate law, Equation 4.7, as shown in Figure 4.4. Oxide scales consisting of θ-Al_2O_3 are known to be more voluminous, more porous, and less protective compared to α-Al_2O_3 [133], thus the growth kinetics are increased due to additional faster surface diffusion as compared to solely grain boundary and volume diffusion in α-Al_2O_3 [147]. A reduction of the oxidation temperature to 750 °C strongly increases the amount of θ-Al_2O_3 on Fe-33Al and Fe-39Al (see Figure 4.8a), whereas Fe-27Al still exhibits the flat "epitaxial" growth of α-Al_2O_3 exclusively.

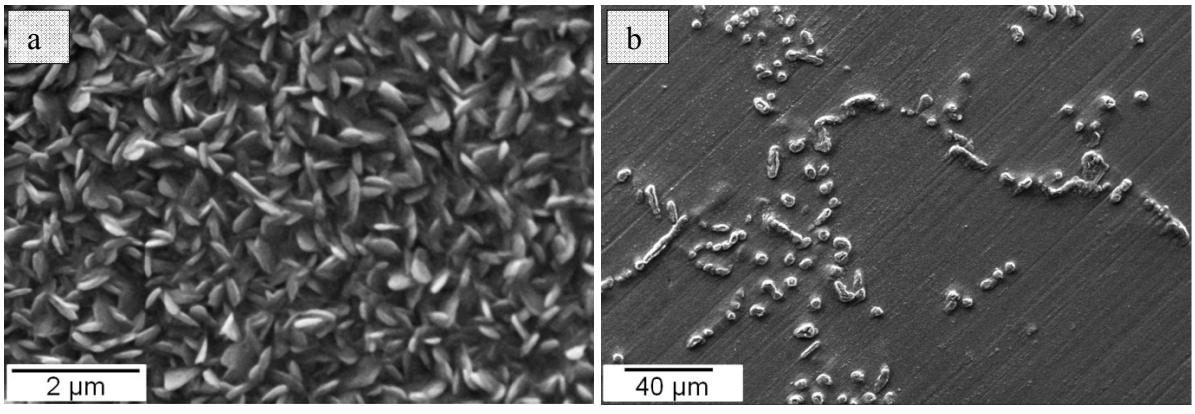

Figure 4.8: Surfaces after 550 h oxidation at 750 °C (SEM-SE image) a) Fe-39Al, exhibit θ-Al_2O_3 scale morphology b) Fe-27Al exhibit α-Al_2O_3 scale morphology exclusively and elevated structures at precipitates.

In order to identify the responsible alloying element for establishing α-Al_2O_3 at 750 °C, a ternary alloy Fe-27Al-0.8Nb was oxidized at 750 °C for 550 hThe resulting oxide scale is

shown in Figure 4.9 revealing the same flat epitaxial growth of α-Al_2O_3 as shown for the micro-alloyed Fe-27Al alloy, without the whisker type morphology that is typical for θ-Al_2O_3 visible in Figure 4.8a.

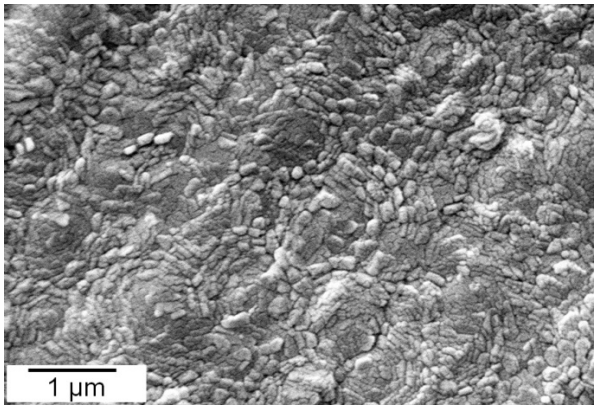

Figure 4.9: Fe-27Al-0.8Nb surface after 550 h oxidation at 750 °C, exhibit α-Al_2O_3 scale morphology exclusively (SEM-SE image).

The absence of θ-Al_2O_3 at 750 °C on iron aluminides has not been reported so far after oxidation in the range of several hundred hours [124][144][148]. It thus seems obvious, that the decrease of α-θ transition temperature on Fe-27Al in this work is related to the higher amount of alloying elements in solid solution as compared to Fe-33Al and Fe-39Al. A possible mechanism could be the primary formation of a niobium containing oxide scale that has a corundum structure such as $Nb_2Fe_4Al_9$ [149] that provides a nucleation site for subsequent growth of α-Al_2O_3. However, such a phase could not be detected by conventional XRD measurements as used in this work. The preferential formation of α-Al_2O_3 on oxides with a corundum structure has been demonstrated for pure metal coatings on Fe-50Al for Fe, Cr, and Ti [137]. A beneficial effect of Nb on oxidation resistance was also observed in other alumina forming alloys, for example in the TiAl system by lowering the threshold Al content for the formation of an alumina scale through a variation of the chemical activities of Ti and Al [150] and by impeding mass transfer into TiO_2 [151]. This effect is accompanied by the formation of a Nb_2Al layer in the metallic matrix at the oxide–metal interface [150]. Additionally, ^{18}O tracer experiments by Pint et al. showed that the presence of so-called reactive elements like Zr or Y inhibits the outward diffusion of aluminum through the oxide scale and promotes the inward diffusion of oxygen which thereby reduces the oxidation rate of NiAl and FeAl alloys [152]. This effect is attributed to the segregation of the reactive elements to grain boundaries in the oxide scale [152]. However, our EPMA-analysis showed neither any enrichment of Nb or Zr in the oxide scale nor at the interface substrate / oxide-

scale. Thus, in conclusion, up to now it is not clear by which mechanism(s) the alloying with Nb and Zr promotes the formation of α-Al_2O_3 scales at low oxidation temperatures. Hence, further investigations are necessary to shed light on this peculiar behavior.

4.3.3. Internal oxidation

An additional mass gain during oxidation can be attributed to internal oxidation processes. Cross-sections of oxidized samples revealed the formation of Al_2O_3 inside the specimens. Internal oxidation occurred in all alloys around precipitates starting at the interface precipitate / matrix (Figure 4.10).

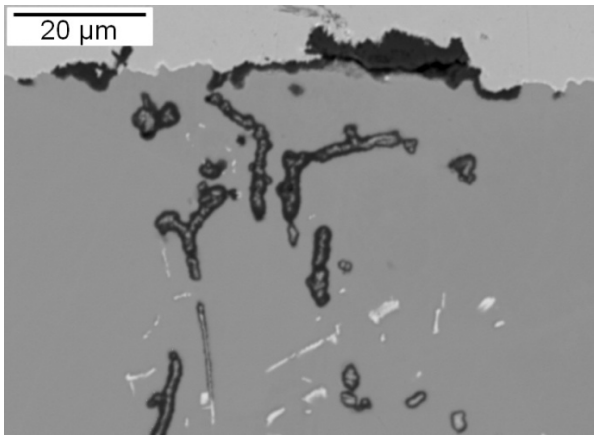

Figure 4.10: Cross-section of Fe-33Al after 550 h at 900 °C (SEM-BSE image). Internal oxidation is indicated by dark areas due to oxygen enrichment.

While the precipitates consist of thermodynamically stable carbides and borides it is aluminum oxide that forms a shell around the precipitates. This was proven by EPMA elemental mapping (Figure 4.11).

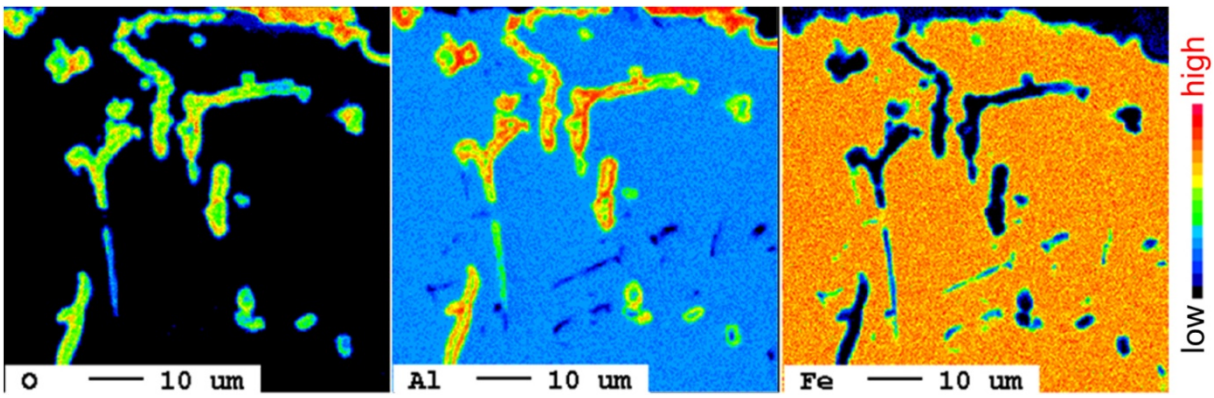

Figure 4.11: Element mapping of oxygen, aluminum, and iron by EPMA of Fe-33Al after 550 h at 900 °C (corresponding to Figure 4.10).

For each alloy and test condition a certain depth could be estimated to which internal oxidation occurred (see Table 4.1). One could assume that the shape of the precipitates, namely the circumference to area ratio resulting in variable wetting of the dendrite arms, might possibly determine the depth of internal oxidation. However, this ratio was found to be on the same level for all alloys. Hence, the interface density (precipitates / FeAl-matrix) depends only on the volume fraction of precipitates. The zone of internal oxidation increases also with increasing volume fraction of precipitates. However, not all precipitates within the estimated internal zone are oxidized, even if they are very close to the specimen surface as shown in Figure 4.10. Hence, fast diffusion paths for oxygen must be responsible for the selective oxidation of the FeAl matrix around precipitates. These could be either grain or phase boundaries. In order to investigate whether the precipitates form a contiguous network inside the FeAl matrices, EBSD orientation mappings were carried out. They revealed that precipitates are arranged in colonies with same crystallographic orientation (see Figure 3.12). It can be concluded that each colony grew from the same nucleus and the precipitates are contiguous up to a range of about 100 μm. Consequently the extent of the colonies is increased with increasing volume fraction of precipitates (see Table 4.1). These continuous networks of precipitates permit a fast diffusion path for oxygen into the material and also for aluminum outward diffusion resulting in the elevated and voluminous structures on the sample surface shown in Figure 4.6b.

4.3.4. Kinetics

The Arrhenius-plot (Figure 4.12) compiles the temperature dependence of parabolic rate constants for metastable θ-Al_2O_3 and stable α-Al_2O_3 scale growth on various NiAl and FeAl alloys [125][136][153].

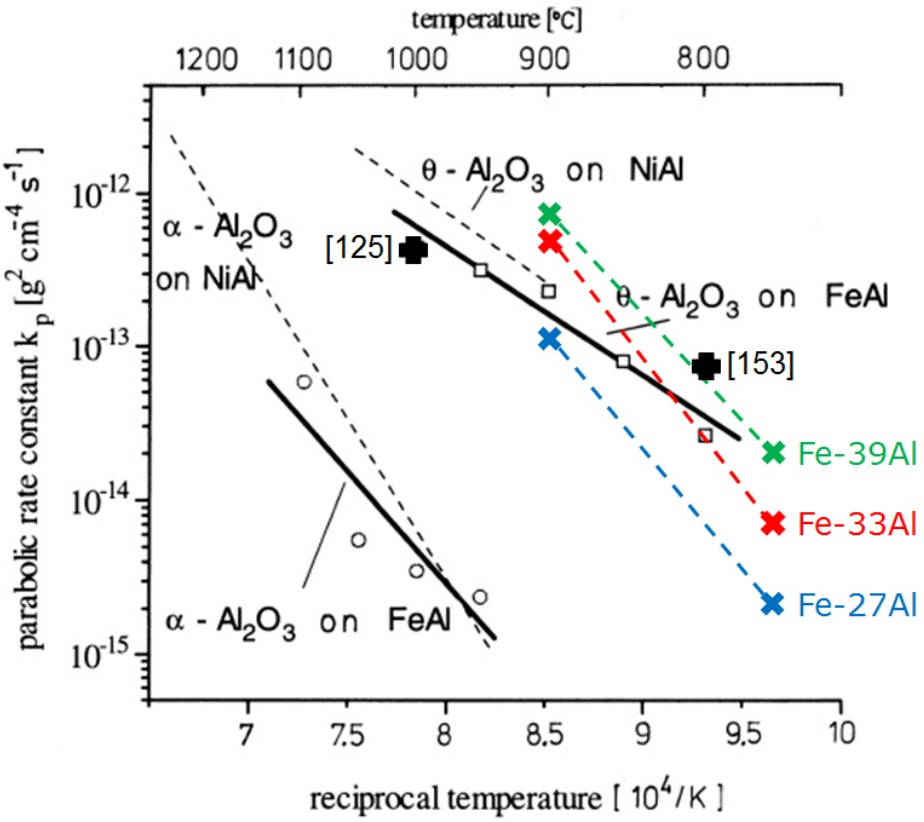

Figure 4.12: Arrhenius plot for the parabolic rate constants of FeAl and NiAl [136]. Own data are plotted in blue, red and green colors, respectively. Two additional data points at 1000 °C for Fe-37Al and at 800 °C for Fe-40Al were taken from Xu [125] and Martinez [153], respectively.

Accordingly both, binary iron- and nickel-aluminides preferentially form metastable θ-Al_2O_3 at temperatures below 900 °C, whereas above that temperature stable α-Al_2O_3 grows at a much lower rate [136]. Connected with that, lower activation energies for scale formation are found for θ-Al_2O_3, see the respective slopes of the curves. As the rate constants of the investigated alloys lie in the range of those found for metastable θ-Al_2O_3 but with a (steeper) slope corresponding to that observed for α-Al_2O_3 it can be concluded, that the alloying elements in solid solution (Zr, Nb) promote the formation of α-Al_2O_3 even below 900 °C. However, the same alloying elements in the precipitated state deteriorate the oxidation resistance in terms of internal oxidation. The total mass gain in the alloys investigated is composed of two effects: the oxide scale growth on the specimen surface and the amount of internally oxidized zone.

4.4. Summary and Conclusions

The oxidation behavior in air at 750, 900, and 1050 °C of micro-alloyed Fe-39Al, Fe-33Al, Fe-27Al, and ternary Fe-27Al-0.8Nb was investigated utilizing cyclic oxidation tests.

Parabolic oxidation rates are comparable to those of binary iron aluminides, nevertheless the oxidation behavior is substantially different. The following more specific results and conclusions were obtained:

- The investigated alloys exhibit a parabolic rate law at 750 and 900 °C up to 550 h, whereas massive spallation occurred at 1050 °C
- The increasing mass gain with increasing aluminum content is due i) to a larger amount of internally oxidized zones and, ii) thicker oxide scales due to the formation of metastable θ-Al_2O_3 (instead of α-Al_2O_3).
- The volume fraction of precipitates is increasing at higher aluminum contents, at the same time alloying elements in solid solution decrease, because the absolute concentrations of alloying elements in all alloys are on the same level.
- The θ-Al_2O_3 / α-Al_2O_3 transition temperature in Fe-27Al could be decreased to 750 °C, or by up to 0.8 at.% Niobium in solid solution in Fe-27Al-0.8Nb.

Alloying elements in the precipitated state deteriorate the oxidation behavior in terms of internal oxidation. The precipitate-matrix interfaces catalyze the formation of Al_2O_3 and act as starting points for internal oxidation. Moreover they are fast diffusion paths for oxygen inward and aluminum outward diffusion.

5. Plasticity at room temperature as a function of strain rate

5.1. The origin of strain rate sensitivity

Plastic deformation is carried by dislocations, when an applied stress is high enough for dislocation sources to become operative. In bcc metals the flow stress can substantially increase by increasing the strain rate. Therefore, a greater effect for impeding dislocation motion is given at high strain rates. In general, an increase in strain rate is analogous a decrease in temperature [11][154]. To rationalize this effect, barriers for dislocation are classified into two categories: athermal barriers (such as long-range interaction of dislocations) and thermal barriers (such as Peierls potential, solute atoms). Flow stress consists then of both contributions:

$$\tau_F = \tau_T + \tau_{At} \tag{5.1}$$

τ_F: *Flow stress*

τ_T: *Thermal component of flow stress*

τ_{AT}: *Athermal component of flow stress*

Athermal barriers need to be overcome by shear stress, whereas the overcome of thermal barriers can be assisted by temperature (thermal activation). The applied resolved shear stress required for dislocation glide in a perfect crystal without the assistance of thermal activation (at 0 K) is called Peierls stress [154]. It arises as a consequence of the periodic structure of the crystal lattice and depends on the force – distance relation of the interatomic bonding (see schematic Figure 5.1).

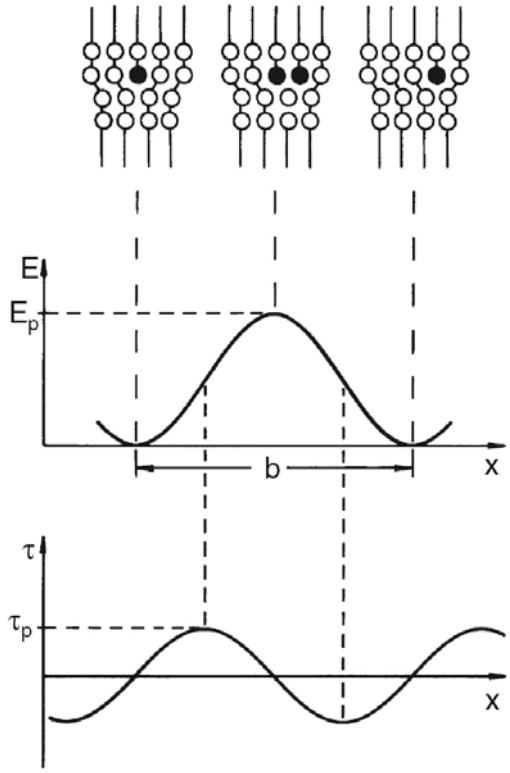

Figure 5.1: Course of Peierls stress τ_p and energy E_p for dislocation slip [155].

Peierls stress and energy are correlated by:

$$\tau_P = \frac{2\pi}{b^2} E_P = \frac{2G}{(1-\nu)} e^{\left(-\frac{2\pi d_G}{(1-\nu)b}\right)} \tag{5.2}$$

τ_P: *Peierls stress*

E_p: *Peierls energy*

G: *Shear modulus*

υ: *Poisson ratio*

d_G: *Glide plane spacing*

b: *Burgers vector*

The Peierls stress is decreasing with increasing d_G and decreasing b and hence, slip occurs most likely on closely "packed" planes and the shortest lattice point directions within these planes. The probability for dislocations to overcome the Peierls stress assisted by thermal fluctuations is given by the Boltzmann factor $exp\left(\frac{\Delta G^*(\tau)}{\mathrm{k}T}\right)$, where $\Delta G^*(\tau)$ is the activation energy to overcome Peierls stress for a given shear stress. In fcc metals which exhibit close packed slip planes $\Delta G^* \approx \mathrm{k}T$, the thermal activation energy for overcoming Peierls stress is given at all temperatures [154][155]. Hence, a thermal activation of overcoming Peierls potential is given at all temperatures. A small contribution of temperature on strength in fcc

metals is only given by the temperature dependency of the shear modulus. On the contrary, in bcc metals (and structures with lower crystal symmetry), which do not exhibit close packed slip planes $d_G(bcc) < d_G(fcc)$. This results in $\Delta G^* > kT$ so that thermal activation can significantly contribute to overcoming of Peierls stress beyond a critical temperature (T_{C2}) and the applied stress necessary for plastic flow is lowered (see Figure 5.2).

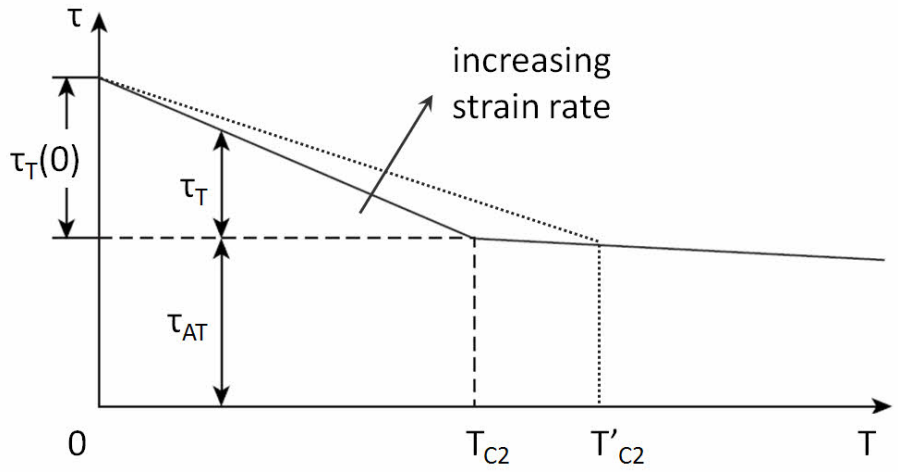

Figure 5.2: Variation of the flow stress with temperature and strain rate for bcc metals [154] (modified by the influence of strain rate).

Above T_{C2} conditions for plasticity are satisfied, whereas below T_{C2} dislocation motion is largely impeded. If $T > T_{C2}$, where thermal activation provides a major portion for dislocation motion, the rate for overcoming Peierls stress is given by:

$$r_p = \upsilon_D e^{-\left(\frac{\Delta G^*(\tau)}{kT}\right)} \tag{5.3}$$

r_p: *Rate for overcoming Peierls stress*

υ_D: *Vibration frequency of dislocation*

$\Delta G^*(\tau)$: *Activation energy to overcome Peierls stress for a given shear stress*

Regarding Equation 5.3, the effect of strain rate on dislocation motion can be rationalized by the vibration frequency of dislocations. As the strain rate is decreased there is an increasing probability that dislocation vibrations resulting from thermal energy may enable to bulge dislocation segments from one minimum to the next, because more attempts can be made for overcoming the Peierls barrier. Vice versa higher strain rates result in less attempts and consequently in an increase of yield strength. The averaged dislocation velocity is than related to the distance of two valley in the Peierls potential (see Figure 5.1), which is equal to the Burgers vector:

$$\bar{v} = b\upsilon_D e^{-\left(\frac{\Delta G^*(\tau)}{kT}\right)} \tag{5.4}$$

$\bar{v}$: *Average dislocation velocity*

Equation 5.4 describes how mainly "pinned" dislocations are responsible for plasticity by thermal activation which results in slip of the length of a Burgers vector. The strain rate is then given by the classical Orowan equation:

$$\dot{\varepsilon} = \frac{d\varepsilon}{dt} = \rho_m b\bar{v} = \rho_m b^2 \upsilon_D e^{-\left(\frac{\Delta G^*(\tau)}{kT}\right)} \tag{5.5}$$

$\dot{\varepsilon}$: *Strain rate*

ρ_m: *Mobile dislocation density*

Equation 5.5 implies that sufficiently high temperatures or low enough strain rates increase the probability for activating dislocation motion by thermal activation in the presence of an applied load. Contrary, low temperatures and high strain rates can lead to significant strengthening due to smaller contributions by thermal activation. The concept presented in this Chapter is also valid for the investigated alloys, which are ordered derivatives of the bcc crystal structure.

5.2. Plasticity of iron aluminides as a function of strain rate

Detailed studies of the mechanical behavior of iron aluminides started in the 1960's [156-158]. The influence of strain rate on the mechanical response of ordered iron-aluminides at elevated temperatures has been studied predominantly on B2-ordered FeAl alloys to verify the vacancy hardening model proposed by George and Baker [140]. They predicted that the peak in yield stress at high temperatures is shifted to higher stresses and temperatures with increasing strain rate due to the suppression of vacancy-assisted creep mechanisms and this has been since verified by subsequent investigations [159][160]. In contrast, information about the mechanical response of $D0_3$-ordered Fe_3Al at high strain rates is limited, both at ambient and elevated temperatures. Gray has reported on the high-strain rate behavior of an Fe-30Al alloy and shown it to be similar to that for B2-ordered Fe-40Al-0.1B at strain rates up to 3000 s^{-1} [160] although no information was given on the state of ordering in this Fe-30Al alloy.

5.3. Experimental Procedure

5.3.1. Sample production

The alloys examined in this study were produced as described in Chapter 2 with comparable cooling conditions. This is of major importance, since it is well known that the stress-strain behavior of iron aluminides at room temperature can vary substantially due to quenched-in vacancies [161]. At the extreme strain rates of 10^{-4} s^{-1} and 2400 s^{-1} mechanical testing was additionally performed with cylindrical specimens with a diameter and length of 5 mm to evaluate the influence of specimen geometry on the stress-strain response. However, this was found to be negligible.

5.3.2. Mechanical testing

Each test was performed at least twice and revealed satisfactory reproducibility in all cases. For all tests conducted in this study, the nominal strain rates were constant for plastic strains up to ~30 %. However, in the early stages of plastic deformation using the Kolsky / Hopkinson bar test setup, a non-uniform stress state is expected in the sample and therefore, values below 5 % plastic strain are not utilized for comparison purposes [162].

The plastic deformation was inhomogeneous within the samples under certain test conditions. Therefore micropillars were fabricated in special regions of interest inside deformed samples and subsequently mechanically tested to evaluate the interplay of microstructure and strength on a microscopic scale. The locations for micropillar fabrication were selected inside the dendrite arms avoiding precipitates or grain boundaries. The loading axes of the micropillars were identified by EBSD measurements on the specimen surface and subsequent micropillars were machined inside these similarly oriented dendrites so that direct comparison of micropillar response is possible. As the primary goal of the micropillar tests was to determine the stress for onset of plastic flow, the reported stress-strain curves were truncated at ~6 % strain although the tests themselves were taken to higher strains.

5.4. Results

It is the intent of this Chapter to systematically explore the deformation characteristics of iron aluminide alloys with the chemical compositions 27 and 39 at.% Al over a wide range of deformation rates to enable correlations between strain rate and material degradation. Emphasis is placed on identifying the operating deformation modes as a function of alloy composition (state of order) and applied strain rate. The Fe-33Al alloy was not investigated

here, because the microstructure is very similar to the Fe-39Al alloy and preliminary investigations revealed similar mechanical response.

5.4.1. Mechanical response

The results from uniaxial compression tests conducted over a range of strain rates at room temperature for the ($D0_3$-ordered) Fe-27Al alloy and the (B2-ordered) Fe-39Al are presented in Figure 5.3a and b respectively.

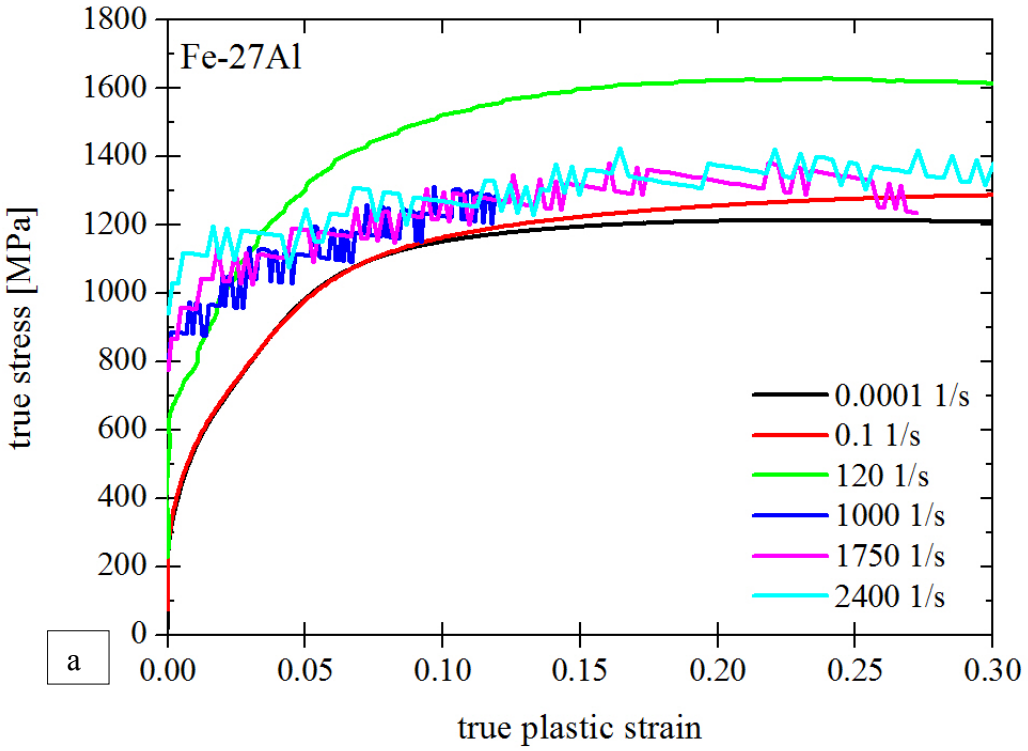

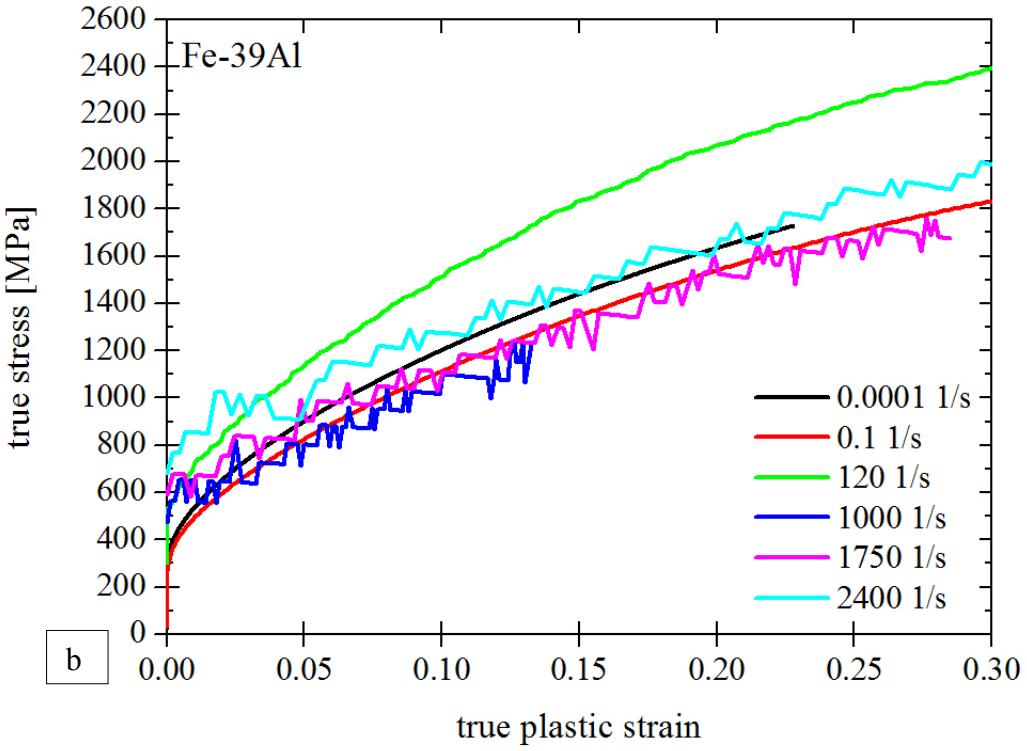

Figure 5.3: Plastic stress-strain response at various strain rates a) Fe-27Al b) Fe-39Al.

In these Figures, only the plastic portion of the true stress- true strain curves is included. These true stress – true strain curves were calculated assuming uniform deformation up to a maximum of 30 % plastic strain. Generally, the achievable maximum strains are limited by the measurement setups. Whereas the stress-strain curves at the lower strain rates are smooth, the "noise" in the measurement values of the Hopkinson bar can be attributed to limited resolution of the A/D converter; nevertheless the curves show the "true" material response. Whereas the $D0_3$-ordered Fe-27Al (Figure 5.3a) shows a decreasing work hardening response with increasing strain as usually observed for disordered (A2 phase) FeAl-alloys [163], the B2-ordered alloy Fe-39Al (Figure 5.3b) shows an almost linear work hardening behavior up to at least 30 % true strain. The curves for the $D0_3$-ordered Fe-27Al rise rather rapidly but then the hardening response diminishes and the curves plateau in stress and or even show softening (Figure 5.3a). Therefore, for further evaluation either the maximum stress was taken from the stress strain curves of Fe-27Al or the flow stress at a fixed strain of 20 % for Fe-39Al was used.

The onset of plastic flow, as read on the stress axis, for both alloys increases continuously with the applied strain rate (Figure 5.3a and b). However, there are noticeable differences in

strain hardening which lead to the finding that the overall flow stress level appears to be highest at the intermediate strain rate of 120 s^{-1} for both alloys (Figure 5.3a and b). In order to verify this unanticipated response, hardness measurements were carried out on the Fe-27Al specimens deformed at different strain rates, whose stress-strain curves are displayed in Figure 5.3a. The hardness values are provided in Figure 5.4 in the form of a bar graph for the different specimens tested at the various strain rates and compared with the maximum stress reached by each of these specimens noted above the bars.

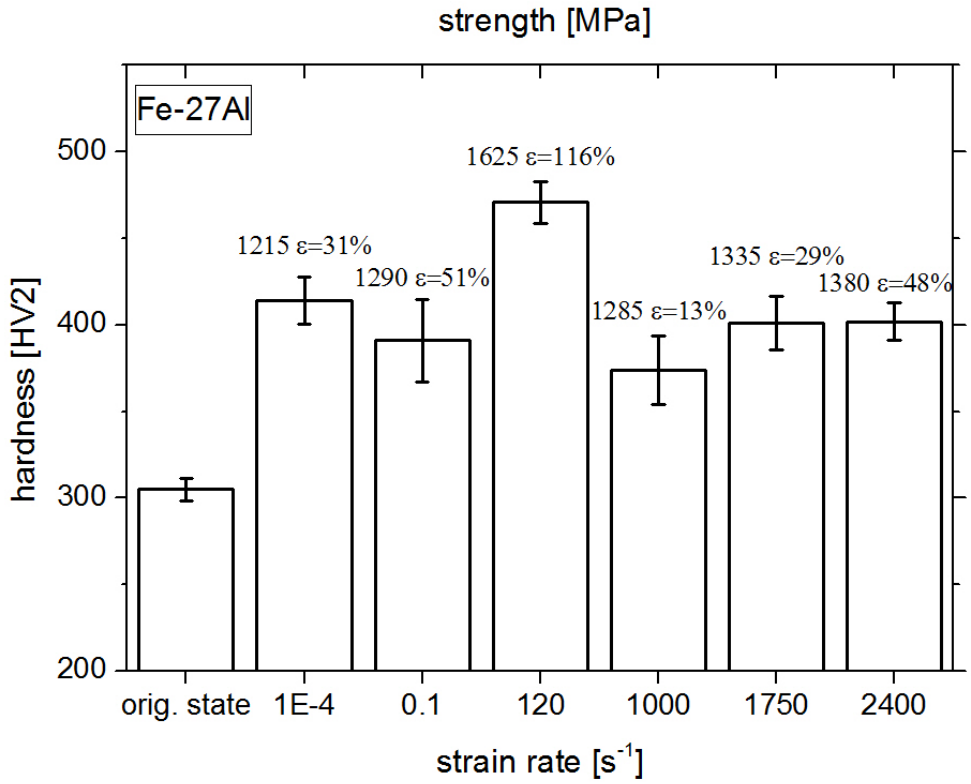

Figure 5.4: Comparison of hardness (bars), compression strength and total strain (numbers above bars) at various strain rates for Fe-27Al.

In addition the maximum strain experienced by each specimen is noted in the bar graph. A significantly higher hardness is noted for the sample tested at the intermediate strain rate (120 s^{-1}), beyond the scatter in hardness data, confirming the trend observed in the stress – strain curves in Figure 5.3a. Although the 120 s^{-1} specimen experiences significantly more total strain than do the other specimens (Figure 5.4), the stress-strain curves in Figure 5.3a confirm that all specimens plateau in stress level as early as after about ~10 % strain (i.e. zero or negligible work hardening beyond this strain level) with the 120 s^{-1} specimen work-hardening nearly same rapidly in this early strain regime, but exhibiting a higher yield

strength reaching a higher plateau stress level at ~0.1 – 0.15 strain. The remaining tests at other faster and slower strain rates more or less overlap with marginal differences. This is reflected in the hardness measurements of the deformed specimens in Figure 5.4 where within the margins of uncertainty, the specimen deformed at $\dot{\varepsilon} = 120\ s^{-1}$ is harder than all other specimens tested and further, the rest of them exhibit more-or-less the same hardness values.

Hardness was also measured for the Fe-39Al samples that had been deformed at various strain rates. In this case however, the stress-strain curves in Figure 5.3b confirm that all specimens exhibit continuous hardening and therefore, if the different specimens experience different total strains, it would be difficult to compare the hardness of the deformed specimens and draw meaningful correlations between hardness and strain rates. Nevertheless, specimens tested at 1750 s^{-1}, 0.1 s^{-1} and 0.0001 s^{-1} reached strength levels of 1750 MPa, 1650 MPa and 1550 MPa at corresponding final strains of 28 %, 31 % and 23 % respectively. These specimens exhibited hardness values of (HV_2) of 543, 522 and 497, which are not substantially different.

5.4.1.1. Shear localization and twinning

All specimens show cracking with increasing strain, but are still contiguous after testing. Crack deflection or branching was not observed. Twinning and locally sheared areas were observed at high strain rates (>10^3 s^{-1}) in Fe-27Al. Cracking was predominantly observed along the interface between the matrix and the shear zone, features that would be considered unfavorable for structural applications.

For Fe-27Al, additional deformation modes were observed at high strain rates that were not present at the lower strain rates whereas this was not the case for Fe-39Al. In Fe-27Al, at high strain rates and true strains exceeding about 0.15, the work-hardening rate passes through zero ($d\sigma/d\varepsilon = 0$). Beyond this level of strain, the work hardening remains flat at low strain rates and marginally decreases at higher strain rates. At high strains and strain rates, Fe-27Al reveals diffuse shear localization (Figure 5.5a), with the width of the shear bands being up to several hundred micrometers.

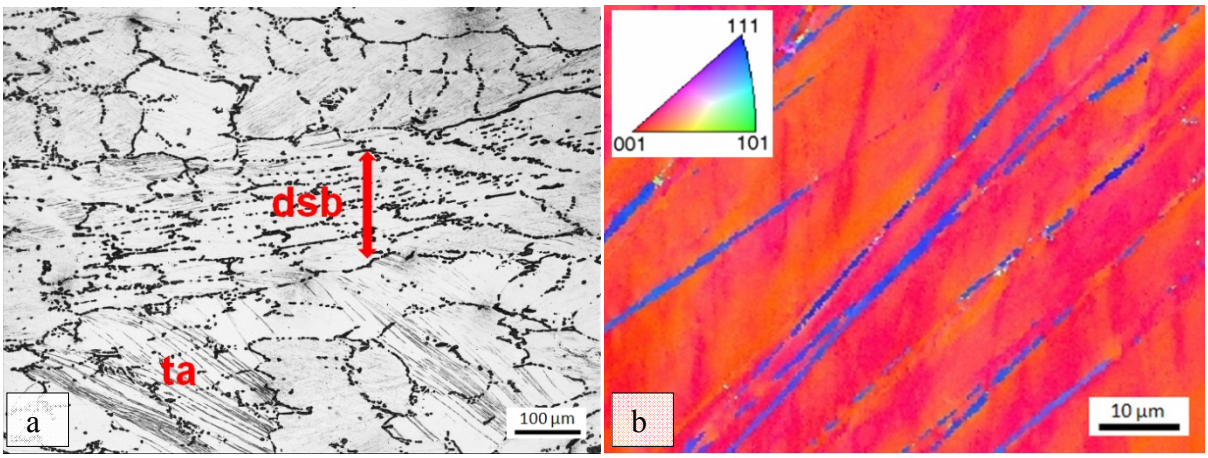

Figure 5.5: Cross-section of Fe-27Al after compression test at a strain rate of 2400 s^{-1} a) formation of a diffuse shear band (dsb) and twinned areas (ta) (imaged by light microscopy) b) Orientation mapping of a twinned area outside of, but adjacent to the dsb (imaged by EBSD), see text for further explanation.

In addition, twinning was prevalent at high strain rates (Figure 5.5a,b); further discussion of shear localization and twinning is presented in Chapter 5.5.2.1 and 5.5.2.2.

5.5. Discussion

Whereas Fe-39Al shows an almost linear work hardening behavior, the plastic portion of the experimental true stress – true strain curve for Fe-27Al can be fitted to a power law equation (for example, Ludwik's equation [164]) of the type

$$\sigma = y_s + \mathrm{C} \cdot \varepsilon^B \tag{5.6}$$

y_s: *Yield strength at zero plastic strain*

C: *Constant*

B: *Work hardening exponent.*

Work hardening rates (= $d\sigma/d\varepsilon$ in [GPa / unit strain]) for both alloys were determined at 0.01 and 0.05 true strain and the results are plotted versus strain rate in Figure 5.6.

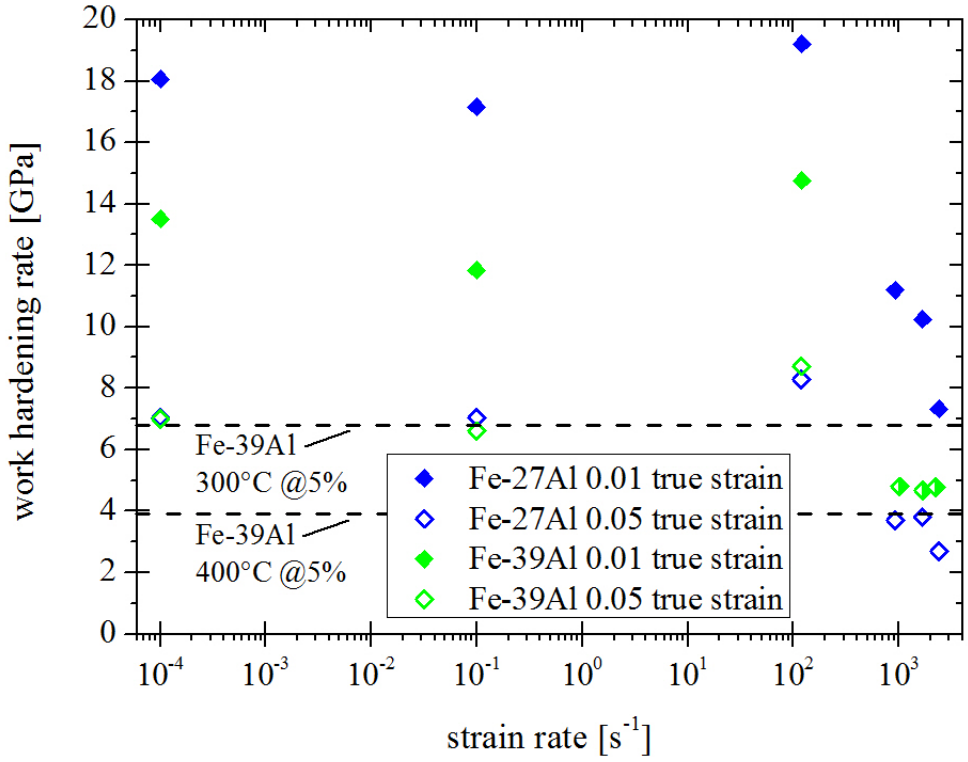

Figure 5.6: Work hardening rates, determined at 0.01 (full symbols), 0.05 (open symbols) true strain for Fe-27Al and Fe-39Al, vs. applied strain rates. Work hardening rates at elevated temperatures determined at a quasi-static strain rate of $3 \cdot 10^{-4}$ s^{-1} are plotted as dashed lines for comparison.

An examination of Figure 5.6 confirms three general features: (a) at strain rates exceeding 120 s^{-1}, a significant drop in work hardening rate occurs for both alloy compositions; (b) at all strain rates substantially higher work hardening rates are observed in the $D0_3$-ordered Fe-27Al at 0.01 strain. This observation is also supported by prior work [107], which showed that the work hardening rates of iron aluminides in the range of 25 – 32 % Al at 1 – 1.5 % strain are increased by the presence of $D0_3$-order; (c) at 0.05 plastic strain, the difference in work hardening rate between the two alloys essentially disappeared due to the power law shaped stress-strain curve for Fe-27Al in contrast to the almost linear work hardening response of Fe-39Al. The dependence of work hardening rates on aluminum content as determined in this work fits those of previous studies [107][163][165]. However, deviations with respect to the dependence of work hardening rates on applied strain rate must be noted. These findings are discussed in more detail in the following subchapters.

5.5.1. Fe-39Al

The observed pronounced (almost linear) work hardening response is known for quasi-static test conditions in B2-ordered iron aluminides [160][166-168]. Morris [107] has associated the high work hardening rates in iron aluminides to two factors: the presence of superdislocations which produce stronger dipole locks, and the increased tendency of dislocations to line in screw orientations. Data on strain rate dependence of work-hardening rates in B2-ordered iron aluminides are however less readily available. Gray measured the mechanical response of Fe-40Al-0.1B at low (≤0.1 s^{-1}) and high (≥2000 s^{-1}) strain rates [160]. At high strain rates he found the stress for the onset of plastic deformation to increase with increasing strain rates whereas the work hardening rate was not affected. Our results at high and low strain rates of a micro-alloyed Fe-39Al alloy also indicate a higher stress for the onset of plasticity at higher strain rates, a response typically reflected by body centered cubic alloys and their derivatives [169]. Likewise, the work-hardening rate at the highest rates (>10^{-3} s^{-1}) at a true strain of 0.05 were similar or marginally lower than those measured in the quasi-static regime (Figure 5.6). However, in this paper for the first time, measurements at an intermediate strain rate (120 s^{-1}) are reported and it is shown that the strength at this intermediate strain rate is higher than values obtained at higher and lower strain rates at comparable strains. In fact, as shown in Figure 5.3b, the stress-strain curves at high strain rates more or less overlap those obtained at quasi-static strain rates (even though the stress for the onset of plasticity is higher for the highest strain rates (≥1000 s^{-1}) as compared to the quasi static strain rates); shear localization, twinning and excessive micro-cracking were not observed in the specimens tested at the intermediate strain rate, leading to the question of why the work-hardening rate decreases beyond a nominal strain rate of 120 s^{-1}.

One possible explanation for the decrease in work-hardening in specimens tested above ≥1000 s^{-1} is quasi-adiabatic heating. In order to estimate the temperature increase resulting from quasi-adiabatic heating that is necessary to achieve the measured work hardening rates at high strain rates, isothermal compression tests at quasi-static strain rates were carried out at various temperatures. At 300 °C, an influence on the work hardening rate could not be observed (see dashed horizontal line in Figure 5.6) whereas, the work hardening rate at 400 °C was found to be comparatively lower and lie in the range measured in the high strain rate tests conducted at room temperature. If it is assumed that 100 % of the plastic work is converted to heat, the temperature increase can be estimated as follows [170]:

$$\Delta T = \frac{\Psi}{\rho \cdot C_p} \int \sigma(\varepsilon) d\varepsilon \quad (5.7)$$

Ψ: *Fraction of plastic work converted to heat*

C_p: *Specific heat*

The value used for ρ is 6.04 $\frac{\mathrm{g}}{\mathrm{cm}^3}$ (see Table 3.2) and C_p of 600 $\frac{\mathrm{J}}{\mathrm{kg \cdot K}}$ (see Figure 3.14), which is in good agreement to binary Fe-38Al in literature [171]. The integral yields $\int \sigma(\varepsilon) d\varepsilon = 249$ MPa for a deformation of $\varepsilon = 0.2$ and a strain rate of $\dot{\varepsilon} = 2400\ \mathrm{s}^{-1}$. The estimated temperature increase in the sample assuming uniform deformation is 69 K and hence, far below the temperature that would necessary to reduce the work hardening rate by adiabatic heating. Hence, the mechanisms responsible for the reduction of work hardening rates at strain rates ≥1000 s^{-1} are not clear yet and further investigations are necessary. A detailed analysis of dislocation structures at high and low strain rates might give an explanation for the observed trend.

5.5.2. Fe-27Al

The mechanical response of $D0_3$-ordered Fe-27Al differs considerably from the B2-ordered Fe-39Al alloy. The stress strain curves resemble those of disordered iron aluminides (at lower aluminum contents) in appearance [163] and are also characteristic of $D0_3$-ordered Fe_3Al [96][165]. The influence of strain rate in the range of 10^{-4} – 10^{-1} s^{-1} on the shape of the stress strain curve is negligible (see Figure 5.3a). At the intermediate strain rate of 120 s^{-1}, the stress-strain curve is simply shifted to higher stress levels due to the higher onset of plastic flow. As in Fe-39Al, quasi-adiabatic heating is considered negligible at intermediate strain rates. At strain rates ≥1000 s^{-1}, the onset of plastic flow is higher, but the work-hardening rates decrease significantly. This results in a crossover with the stress strain curve at 120 s^{-1} and a stress plateau that is similar in magnitude to those from the quasi-static tests. Investigation of the deformed microstructure revealed twinning as well as shear localization at high strain rates (≥1000 s^{-1}). Shear localization can lead to higher local temperatures within these regions if adiabatic conditions are assumed and this could explain the loss in work hardening rate at the high strain rates. Additional factors that need consideration in interpreting the onset of plastic flow and work-hardening behavior in the high strain rate tests include: i) the dependence of Peierls stress on strain rate for bcc metals [169] and ii) the observation of twinning as a relevant deformation mechanism contributing to plasticity. Thus, it has been shown previously in Cu single crystals and Hadfield steel that when deformation is dominated by primary twinning, the resulting work-hardening rate is low. It only increases

when secondary twins become operative and intersect primary twins [172]. Both, twinning and shear localization are discussed in more detail in the following subchapters 5.5.2.1 and 5.5.2.2.

The results reported by Gray [160] for the work hardening response for the Fe-30Al alloy in his study differs from the observations for Fe-27Al in this work. In [15], the response strongly resembles that of B2-ordered FeAl, in that work hardening rate decreases with decreasing aluminum content and the plastic stress-strain behavior is almost linear, as noted above for B2-ordered FeAl. Since the presence of the $D0_3$-ordered structure was not confirmed by Gray in [15], and the phases present at room temperature in Fe-Al alloys in this composition range are known to be related to prior cooling conditions, it is possible that partial B2-ordering may have been present in the Fe-30Al alloy investigated by Gray [15]. Lastly, Gray [15] found work hardening rates to be independent of the applied strain rate and aluminum content for both, Fe-30Al and Fe-40Al, which is different from our observations in this study.

5.5.2.1. Shear localization

The microstructure that had evolved in the shear localized zone and in regions adjacent to it as well as away from it was further investigated by SEM/EBSD and by TEM. The shear zone and the surrounding uniformly deformed matrix exhibit $D0_3$-order (Figure 3.15b) confirming that diffuse shear banding does not produce disorder. EBSD measurements were performed inside and outside the shear zone of the same sample (Fe-27Al, $\dot{\varepsilon}$=2400 s^{-1}) with the same measurement and evaluation procedure to enable valid comparison. The step size used was 35 nm to permit mapping of the microstructure on a microscopic scale. An orientation mapping inside the shear zone is shown in Figure 5.7a.

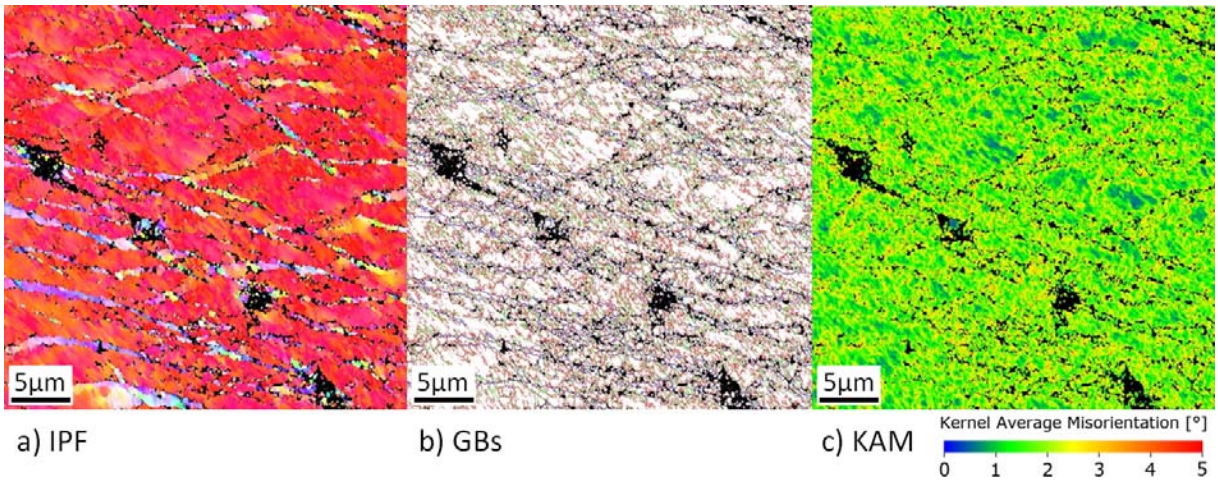

Figure 5.7: Fe-27Al post deformation at 2400 s^{-1} inside the shear zone imaged by EBSD. a) Inverse Pole Figure (see Figure 5.5b for color code). b) Grain Boundaries are imaged (red: 2-5°; green: 5-15°; blue: >15°). c) Kernel Average Misorientation plot, see text for further explanation.

The matrix primarily displays various shades of red, indicating an area with a single crystalline orientation prior to deformation that has likely developed regions of small misorientation during deformation. Average confidence index is 0.3 and minimum confidence index used for analysis is 0.1 (common threshold value) with marginal clean up procedure. The black dots in Figure 5.7a are precipitates and not indexed here. Some twins are also present (in shades of blue and purple) which appear to have formed prior to shear localization and subsequently extensively sheared (compare Figure 5.7a against Figure 5.5b where the twins are intact in a location outside but adjacent to the shear band). The twins are separated from the matrix by large angle grain boundaries (misorientation >15°) whereas all other interfaces are misoriented less than 15° (see Figure 5.7b). The local misorientation inside the shear zone is imaged by Kernel Average Misorientation mapping (KAM) in Figure 5.7c. The image can be read as follows: next nearest neighbors of 3 times step size are imaged (Kernel range = 3) which is ~105 nm to image microstructural features on the same scale. The threshold value for this analysis was set to 5° misorientation because (i) the misorientations between subgrains are typically of the order of 1 – 5° [173] and (ii) to exclude the influence from the high angle grain boundaries at the matrix/twin interfaces on the local misorientation. The average local misorientation inside the shear zone is 1.8°.

For comparison, see Figure 5.8a-c, which is representative of an area away from the shear zone.

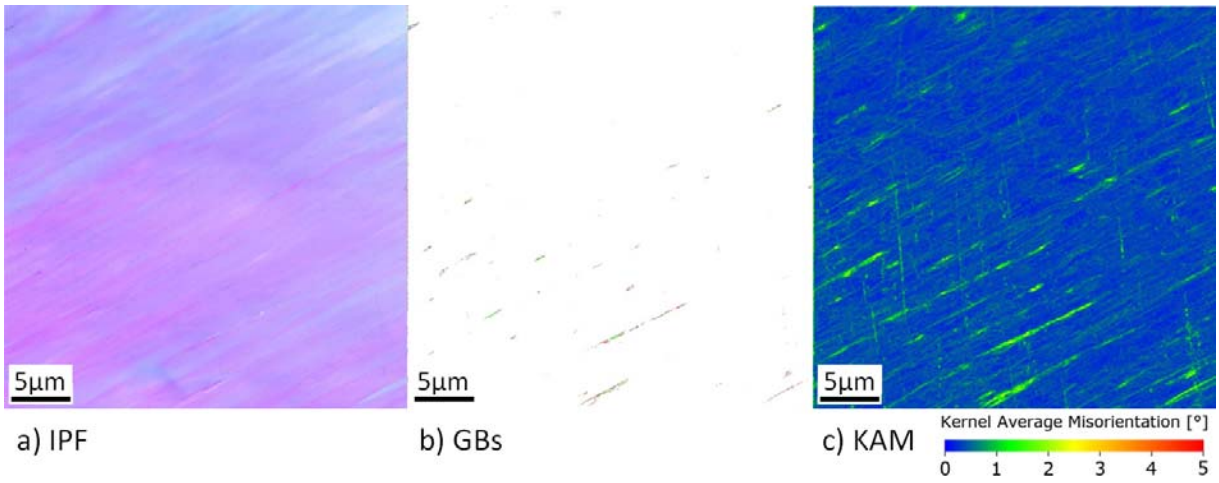

Figure 5.8: Fe-27Al post deformation at 2400 s^{-1} away from the shear zone imaged by EBSD. a) Inverse Pole Figure (see Figure 5.5b for color code). b) Grain Boundaries are imaged (red: 2-5°; green: 5-15°; blue: >15°). c) Kernel Average Misorientation plot, see text for further explanation.

Average confidence index is 0.95 and minimum confidence index used for analysis is 0.1 without any clean up procedure. The local misorientation is almost zero except for some straight lines, which may be related to sample preparation and/or deformation traces. The microstructures inside the shear zone (Figure 5.7a-c) and the surrounding uniformly deformed matrix (Figure 5.8a-c) are significantly different. The substructures found inside the shear zone are thought to have formed during plastic deformation by dynamic recovery.

To reveal the influence of these different microstructures on the mechanical properties, additional experiments were performed. The micro- and macro-hardness inside and outside the shear zone were measured and found to be about the same at 400 ±15 $HV_{0.2}$, even though more extensive plastic deformation is thought to occur within the shear zone. In addition, two micropillars were machined by focused ion-beam milling from (i) inside and (ii) outside the shear zone and (iii) from an undeformed sample as well, and these were all tested in compression using a flat punch nanoindenter. The loading axis was determined by EBSD to be close to [125] in all cases. In contrast to hardness measurements, the micropillar deformation experiments demonstrated that the onset of plastic flow, described as the first deviation from linearity in $d\sigma/d\varepsilon$ versus σ plots, was substantially higher for a micropillar extracted from inside the shear zone (1500 MPa) as compared to one extracted from the uniformly deformed matrix (1100 MPa); the onset of plastic flow of the micropillar obtained from an undeformed sample was much lower (700 MPa) due to the absence of prior work hardening (see Figure 5.9).

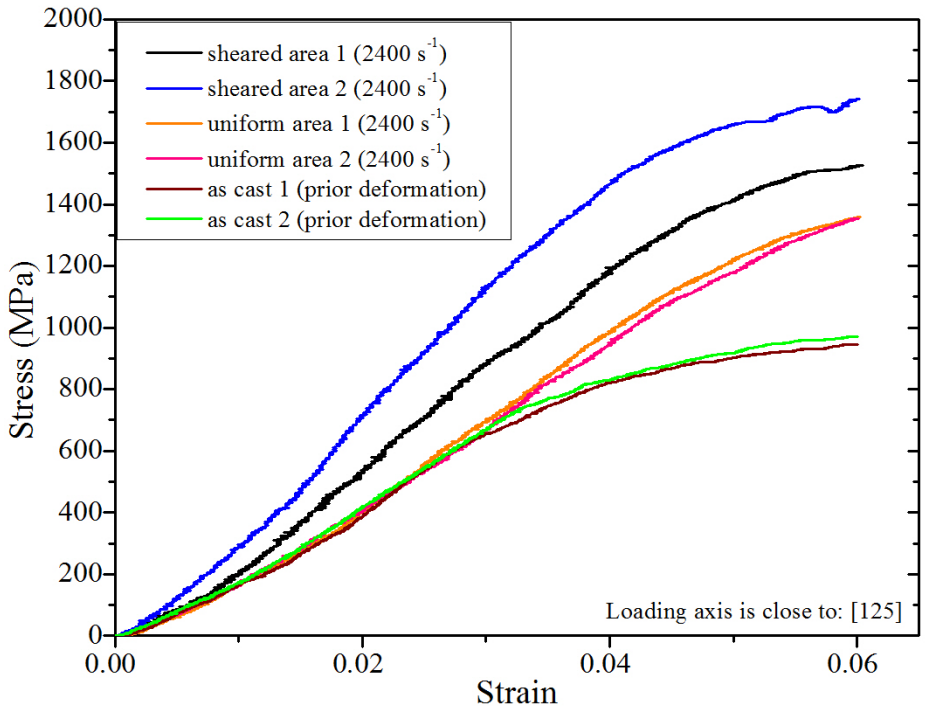

Figure 5.9: Fe-27Al stress-strain curves of micropillars up to 6 % total strain (raw data plotted).

The micropillars deformed primarily by single slip as shown in Figure 5.10.

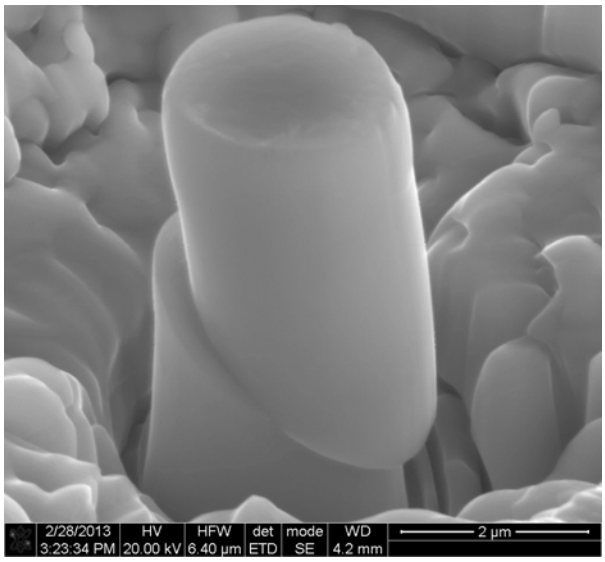

Figure 5.10: Micropillar (post deformation) inside the shear zone (Fe-27Al, $\dot{\varepsilon}$=2400 s^{-1}) (SEM-SE image).

For the [125] loading axis, the critical resolved shear stress (CRSS) was determined for the undeformed (i.e. as-cast) sample. It is known that slip in $D0_3$-ordered Fe_3Al occurs on the {110} <111> slip system in the low temperature regime [174][175]. Superdislocations may be composed of four partials b = ¼ <111> [176]. In the case of the [125] loading axis, the slip

system with the highest Schmidt factor is (101) <$\bar{1}$11> with a CRSS of 353 MPa for the onset of yielding determined as described above. This value serves as an upper bound for CRSS because it is known that some hardening may be introduced during FIB machining by Ga-ions [177]. Alternatively, this value could be attributed to a pillar size effect which is not well investigated for intermetallics.

5.5.2.2. Twinning

Following deformation at strain rates of 1750 s^{-1} and 2400 s^{-1}, twins were observed in Fe-27Al (Figure 5.5b) and are most pronounced at the highest strain rate. Mechanical twins are known to form under favorable conditions such as low temperature and high strain rate in bcc alloys and their derivatives [178]. Earlier work by Cahn and Coll [158] on Fe-23.5Al showed the appearance of mechanical twins when impacted by a hardened steel ball at liquid nitrogen temperature. Similar work has been done decades later by other authors [179][180] leading to the same results. However, this is the first time that high strain rate-induced-twinning has been observed in $D0_3$-ordered Fe_3Al at room temperature. In Figure 5.11a, the bright field image displays a twinned area.

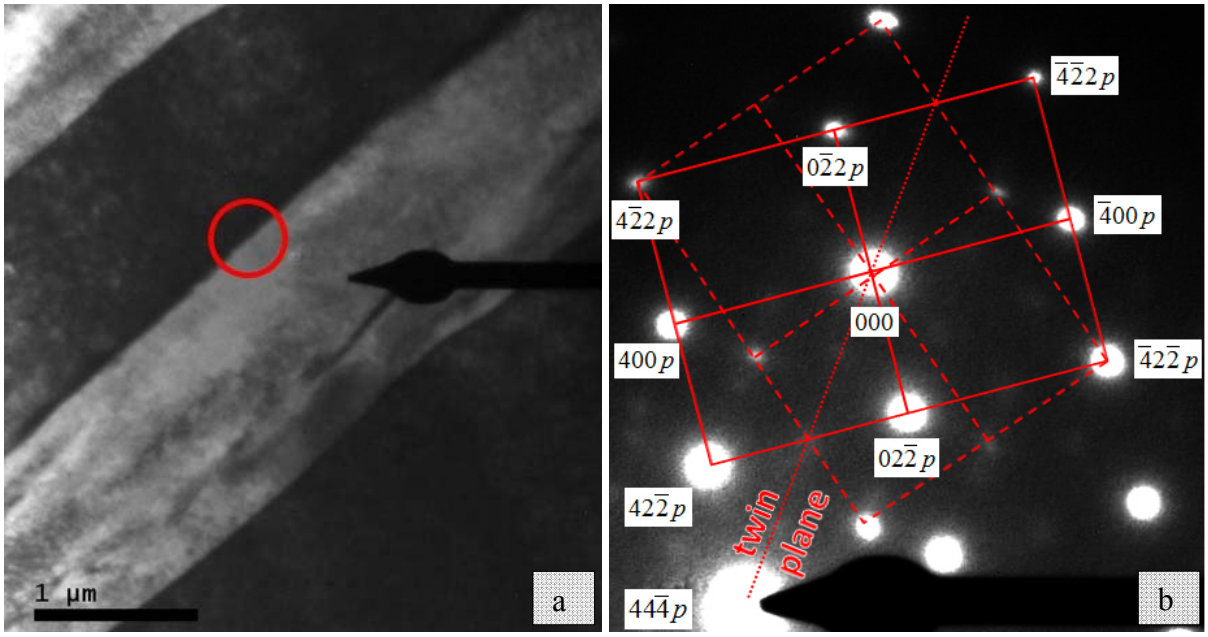

Figure 5.11: 2.2^T –type pseudo in twins in Fe-27Al post deformation at 2400 s^{-1} imaged by TEM. a) Bright field image of a twin (zone axis: [011]). Spot of diffraction is encircled in red. b) SAED pattern of interface matrix / twin.

A selected area electron diffraction pattern from a location that includes the twin and the matrix is shown in Figure 5.11b. The zone axis is (110) and red lines are added to highlight

the twin symmetry to the matrix including the twinning plane (dashed line). The operative twinning system is a $[11\bar{1}]$ shear direction with a $(2\bar{1}1)$ twinning plane. This is in agreement with the results of Park and Goo, who characterized twins in $D0_3$-ordered Fe-25Al [180] based on the work of [181-183], they identified possible twinning configurations in $D0_3$-ordered alloys. The average width of the twins in the present study was determined to be about 1 μm, which is also in good agreement with the findings of Park and Goo [180]. The same twinning system was found to be operative in other $D0_3$-ordered intermetallics including Fe_3Ga [184]. As a consequence of the large unit cell of $D0_3$-order and the mentioned twin symmetry, the formation of a pseudo twin is given here. A pseudo twin will have its atomic sites in a twin relation to those of its parent crystal but the occupancy of these sites will be incorrect [185]. The nomenclature based on Christian et al. of this twinning configuration is a 2.2^T pseudo twin [182]. As pointed out above, neither twinning nor shear localization could be observed in the B2-ordered alloy.

5.6. Summary and conclusions

The mechanical response at strain rates in the range of $10^{-4} – 10^3$ s^{-1} of micro-alloyed Fe-39Al (B2-ordered), and Fe-27Al ($D0_3$-ordered) in the as-cast condition was determined at room temperature. Important findings follow:

- It is shown for the first time that iron aluminides exhibit a peak in the level of maximum stress at strain rates in the range of 10^2 s^{-1}. Higher strain rates in the range of 10^3 s^{-1} were found to cause material degradation. This degradation in Fe-27Al is attributed to strain localization and associated heating, and primary twinning further aggravates this response. The reasons for material degradation in Fe-39Al are not clear yet.

- B2-ordered Fe-39Al exhibits a remarkable linear work-hardening behavior, which persists at true strains up to 30 %, whereas $D0_3$-ordered Fe-27Al shows a behavior with decreasing work hardening as usually observed for iron-rich (A2 phase) iron aluminum alloys [163].

- High strain rate induced twinning was observed for $D0_3$-ordered Fe-27Al for the first time at room temperature at a strain rates ≥1750 s^{-1}. Twinning occurs on the $(2\bar{1}1)$ twinning plane with a $[11\bar{1}]$ shear direction. This twinning configuration was also previously reported to be operative at low temperatures in Fe-25Al [180].

- In Fe-27Al, the formation of locally sheared areas is initiated at high strain rates and at least 0.15 true strain. The shear zone exhibits $D0_3$-order and mechanically driven dynamic recovery resulting in the formation of sub-grains with a size of ~100 nm in diameter and a local misorientation of ~1.8° in contrast to the surrounding uniformly deformed matrix. Although, hardness in this homogeneously deformed region is on the same level as inside the shear zone, micropillar compression studies confirmed a higher stress for onset of plastic deformation within the diffuse shear zone as compared to the region outside this zone; this is a consequence of the refined microstructure and the likely higher dislocation density in the diffuse shear zone where a much larger strain occurs due to localization.

6. Creep behavior

6.1. Fundamentals of creep

Creep deformation is a thermally activated process, which is usually observed at T_H beyond ≈0.4, where diffusional controlled processes are reasonably rapid. Thereby a constant applied mechanical stress below yield strength results in viscoplastic (or inelastic) deformation of a sample [186]. The plasticity at high temperatures is then a function of the following parameters [187]:

$$\Phi(\dot{\varepsilon}, \sigma, T, S, M) = 0 \tag{6.1}$$

σ: *Applied stress*

S: *Microstructural parameter*

M: *Material parameter*

The microstructural parameter *S* is related to the thermo-mechanical history of the material and can further be a function of ε and *t*. Influencing parameters are i) grain size and shape ii) volume fraction of phases and their properties iii) dislocation structure, iv) texture v) density of vacancies and so on. The contributing material parameters are the shear modulus *G*, diffusivities *D*, melting point T_m, and so on. In general a creep curve can be categorized into the regions of primary, secondary, and tertiary creep regime (see Figure 6.1a and b), which goes back to the work of Andrade, who first analyzed the process of creep in 1910; 1914 [188][189].

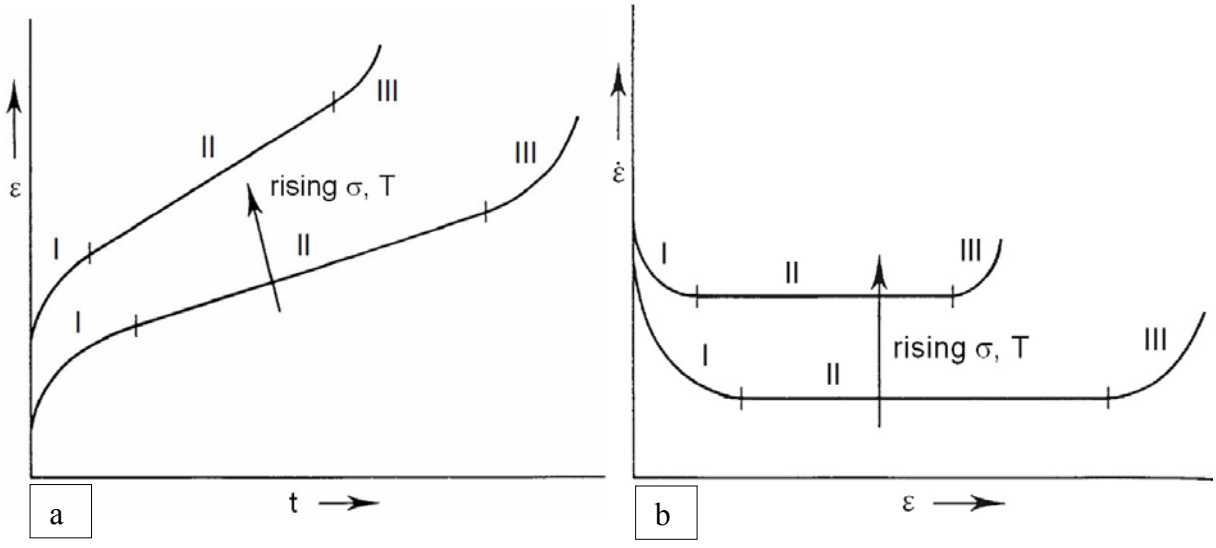

Figure 6.1: Schematic creep curve; a) $\varepsilon(t)$ b) $\dot{\varepsilon}(\varepsilon)$ [190].

After the instantaneous elastic deformation $\varepsilon_{el} = \sigma/E$ (for uniaxial loading, E: Young's modulus) at $\varepsilon \approx 0$, the dislocation density is increasing with strain (stage I), analogous to work hardening at low temperatures. Thereby the internal stress increases during deformation because the dislocation density increases resulting in a decelerating creep rate. The amount of strain required for the transient stage to become steady-state varies substantially from alloy to alloy [187]. For example, in ferritic and austenitic steels, strains of 5 – 10 % can be achieved during creep within stage I [187][191], whereas stage I in Re and WRe5 is almost absent [192][193]. The amount of strain required to achieve steady-state creep rates in the investigated alloys was estimated by the component for transient creep from the empirical Garofalo equation [187][194]:

$$\varepsilon = \varepsilon_I - e^{-mt} \tag{6.2}$$

ε_I: *Total amount of strain in stage I*

m^{-1}: *Measure for transition time between stage I and II*

The convergence towards a steady-state creep rate was then estimated by extrapolating the creep curve by knowing the exponential shape of it. The strain hardening rate h, which is decelerating in stage I can be written as follows [195]:

$$h = \frac{d\sigma}{d\varepsilon} = \frac{d\sigma}{d\rho} \cdot \frac{d\rho}{d\varepsilon} \tag{6.3}$$

ρ: *Dislocation density*

At high homologous temperatures recovery processes, due to dislocation annihilation supported by climb, limit the dislocation density. The recovery rate r can be similarly written to Equation (6.3), whereas it is a function of time instead of strain:

$$r = \frac{d\sigma}{dt} = \frac{d\sigma}{d\rho} \cdot \frac{d\rho}{dt} \tag{6.4}$$

The overall strain rate in terms of dislocations is then given by the Bailey-Orowan equation, which envisages high temperature deformation as a competition between hardening and recovery processes:

$$\dot{\varepsilon} = \frac{r}{h} \tag{6.5}$$

After a sufficient duration and strain, when the quotient of Equation 6.5 is constant, a steady-state creep rate is established, which is characterizing of stage II creep [155][196]. For

addressing a true steady-state creep rate, an appropriate amount of strain must be given in stage II [186], because work hardening is a function of strain. Therefore an amount of >1.5 % plastic strain is defined to use the expression of "steady-state creep rate" in this work. The shape of the curves in Figure 6.1a and b can have the same appearance in plots of the type $\dot{\varepsilon}$ vs. t, but it is recommended rather to plot $\dot{\varepsilon}$ vs. ε to determine "true" steady-state creep rates as "horizontal straight lines" in this plot [186]. In region III the creep rate accelerates again due to creep damage occurring in the sample. Since all creep tests carried out for this thesis are stopped within stage I or II, stage III is not further discussed here. Excellent overviews on the damage mechanisms in stage III are given by Poirier [195] and Nabarro & de Villiers [197].

Related to the three stages of creep, the flow mechanisms are of major interest in the steady-state creep rate regime where structural parts experience the longest period of their lifetime [198]. The steady-state creep rate of metals, which deform under creep conditions is commonly expressed by the "Dorn equation" (Mukherjee et al. [199]):

$$\dot{\varepsilon}_{ss} = \frac{CGb}{kT}\left(\frac{b}{d}\right)^{p}\left(\frac{\sigma}{G}\right)^{n} D_0 e^{\left(-\frac{Q}{RT}\right)} \tag{6.6}$$

C: *Dimensionless constant which includes microstructural features (except grain size)*
G: *Shear modulus*
b: *Burgers vector*
d: *Grain size*
p: *Grain size exponent*
n: *Stress exponent*
D_0: *Frequency factor*
Q: *Activation energy for the deformation process*

It is well established by several investigations of pure metals and solid solution alloys, that different creep mechanism have different values for the constants in Equation 6.6. The creep mechanisms related to the constants p, n, and Q are summarized in Table 6.1, where Q_l, Q_{gb}, Q_p, and Q_i are the activation energies for lattice self-diffusion, grain boundary diffusion, pipe diffusion (along dislocation cores), and the inter-diffusion of solute atoms, respectively.

Table 6.1: Creep mechanisms in metals [200]. HT is referring to "high temperature" and LT to "low temperature" (in the vicinity of 0.5 T_H).

Stress region	n	p	Q	Interpretation
Low	1	2	Q_l	Nabarro-Herring diffusion creep (HT)
		3	Q_{gb}	Coble diffusion creep (LT)
Intermediate	≈ 3-5	0	Q_l	Climb (HT), recovery
			Q_p	Climb (LT), recovery
			Q_i	Viscous glide
High	≈ exp(σ)	0	Q_l	Power-law breakdown

When more than one creep mechanism is operating at the same time, the rate controlling process, i.e. the one with the fastest creep rate, determines the overall creep rate. Hence, the three stress regions mentioned in Table 6.1 show distinct transitions, which are exemplarily shown for creep data collected for pure aluminum in Figure 6.2.

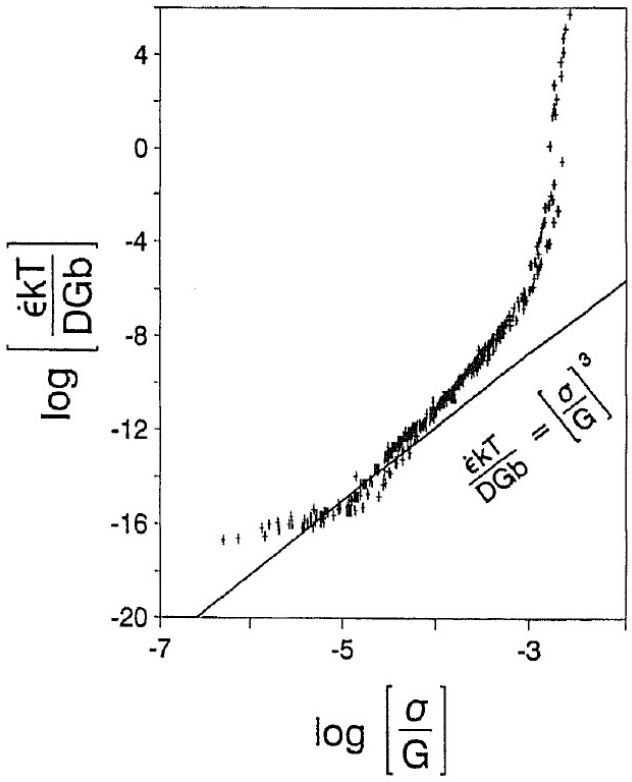

Figure 6.2: Double-logarithmic plot of the steady-state creep rate of pure aluminum, normalized by $\frac{DGb}{kT}$, versus stress normalized by the shear modulus. The straight line represents the natural creep law [201].

At high temperatures and low stresses creep processes controlled by atomic diffusion become dominant (n=1), whereas high stresses at intermediate temperatures promote dislocation

controlled creep mechanisms (n=3–5) [187][201][202]. A further increase in stress results in the power law breakdown, where the creep rate increases exponentially with the applied stress. In practice, the value of "n" is often used to quickly identify the rate controlling creep process. Diffusional creep is Newtonian viscous ($\dot{\varepsilon} \sim \sigma$) and viscosity is grain-size dependent as summarized in Table 6.1. The so-called natural creep law yields a relation of $\dot{\varepsilon} \sim \sigma^3$ for any climb controlled recovery creep, which can be derived from the Orowan equation, see Equation 5.5 in Chapter 5. The value of n=3 is composed of the climb velocity and the dislocation density [186]: the climb velocity depends linearly on the stress: $v \sim \sigma$. The dislocation density is related to the dislocation spacing (mesh size for a three-dimensional network) $\rho \sim \frac{1}{l^2}$ and the stress field of dislocations varies with the inverse of their distance $l \sim \frac{1}{\sigma}$ which leads to $\rho \sim \sigma^2$. In experiments it often observed that n has higher values in the range of $n \approx 5$ (see Figure 6.2). There are theories in literature, which might explain the deviations from the natural creep law towards n>3, for example by Weertman [203]. Other authors like Blum suggest that the natural creep law holds for low stresses $<10^{-4}$ G and deviations towards larger values of n>3 in literature were interpreted as a result of the fact that there is an increasing deviation from the natural creep law with increasing stress towards the power law breakdown regime [201][204].

6.2. Creep behavior of iron aluminides

The low densities of iron aluminides compared to steels and their superior oxidation resistance by forming alumina as a protecting surface scale are the main benefits of these intermetallics, but a drop in strength at higher temperatures and low room temperature ductility are challenges that still need to be overcome. The creep properties of binary iron aluminides are fairly thoroughly investigated by several authors [3][156][205-208] and also some data is available for the creep of $D0_3$-ordered iron aluminides at low temperatures [156]. In order to improve creep strength of iron aluminides several ternary and multicomponent alloys have been developed in the past decades [4][109][209-211]. The aim of these alloy developments is not only to deepen the understanding from a scientific point of view but also to make iron aluminides promising candidates for structural applications at elevated temperatures up to about 650 °C. As mentioned in Chapter 3, several concepts were considered to improve the creep strength such as solid solution hardening, precipitation hardening, stabilizing $L2_1$-order up to higher temperatures [76][212-214], directional solidification with Laves phases [215], oxide dispersion strengthening [216][217] and so on.

Some of these alloys show superior creep resistance in contrast to binary iron aluminides, but at the same time the room temperature ductility always decreases significantly.

In general, an annealing procedure is recommended before the creep properties of alloys is determined to establish a microstructure which is close to thermodynamic equilibrium to achieve steady-state creep rates as quickly as possible. The aim of the work in this Chapter is further to identify the influence of microstructural evolution on the creep deformation beginning from the "as-cast" state (rapidly cooled down from the melt) for the investigated iron aluminides. This gives insight into the kinetics of precipitation and ordering processes and their specific influence on creep until steady-state creep rate is achieved.

6.3. Experimental

6.3.1. Sample production

Test specimens for compression creep were excised out of 15 mm diameter rods by electro-discharge machining (EDM). The specimens were sectioned into cuboids with a squared base of 5 mm and a side of 8 mm length and polished to a 1000-grit finish.

6.3.2. Mechanical testing

Each creep sample was subjected to various stresses or temperatures with a final test condition that matches the start conditions to check that the steady-state creep rates obtained are constant and hence can be considered "true steady-state" creep rates. The term steady-state (ss) creep is used, if the creep rate does not vary for a least 1.5 percent in plastic strain. Otherwise the term "minimum creep rate" (min. creep rate) is used. Creep rates obtained from samples subjected to alternating stresses or temperatures were used for Norton and Arrhenius plots, respectively.

6.4. Results and Discussion

The focus of the creep experiments was put on the alloys Fe-27Al and Fe-39Al. The experiments were performed in a temperature range of 625 – 700 °C and, hence, all alloys are within the B2 single-phase field, if an equilibrium state of microstructures is assumed (see Figure 3.13). Only a few experiments were performed on Fe-33Al, because the creep experiments were very time consuming with overall several thousands of hours acquisition time. For this purpose, some steady-state creep rates (especially at low creep rates) were estimated at lower amounts of strain (<1.5 %), if a convergence towards a steady-state creep

rate could be estimated. The additional measurements performed on Fe-33Al were done to verify certain trends related to alloy composition. In the following two subchapters (effect of stress 6.4.1) and (effect of temperature 6.4.2) the creep curves are discussed mainly in the steady-state regimes (stage II). The early stages of creep, where a steady-state creep rate is not established, are discussed in subchapter 6.4.3 (kinetics of the as-cast state) combined with microstructural investigations. The explanation for imperative time consuming creep experiments will be made clear in this Chapter, too. Material degradation indicating stage III creep was not observed in any experiments, because the total achieved strains (always less than 13 %) during creep were too low.

6.4.1. Effect of stress

The jumps to different stress levels were performed during creep experiments at isothermal test conditions without stopping the experiments. Typical log $\dot{\varepsilon}$ - ε plots for Fe-27Al and Fe-39Al are shown in Figure 6.3a and b, respectively.

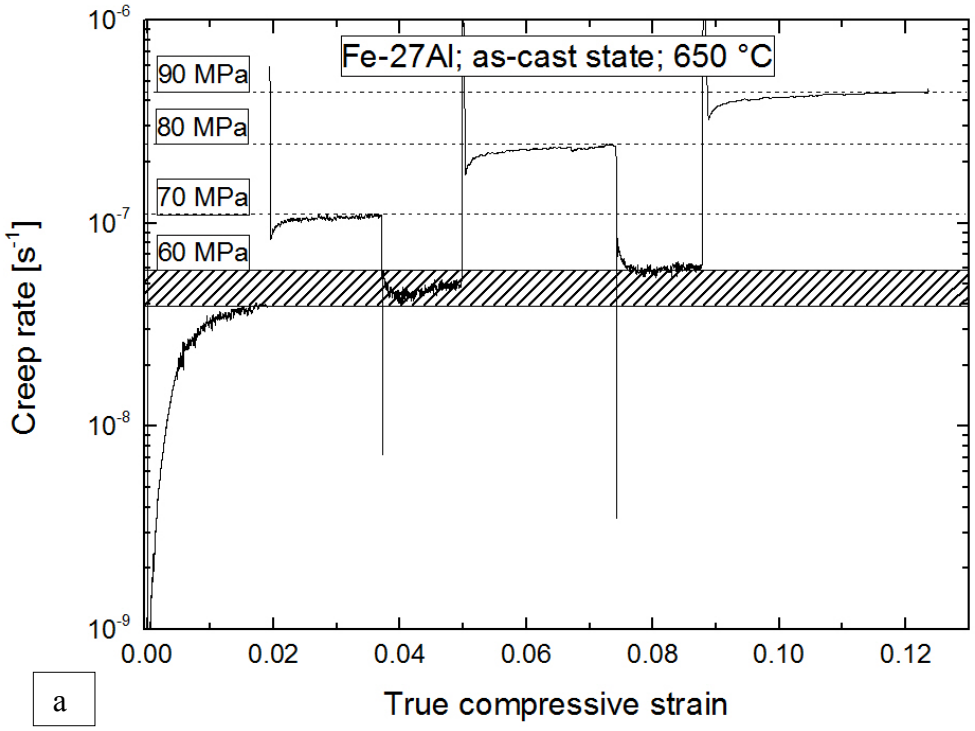

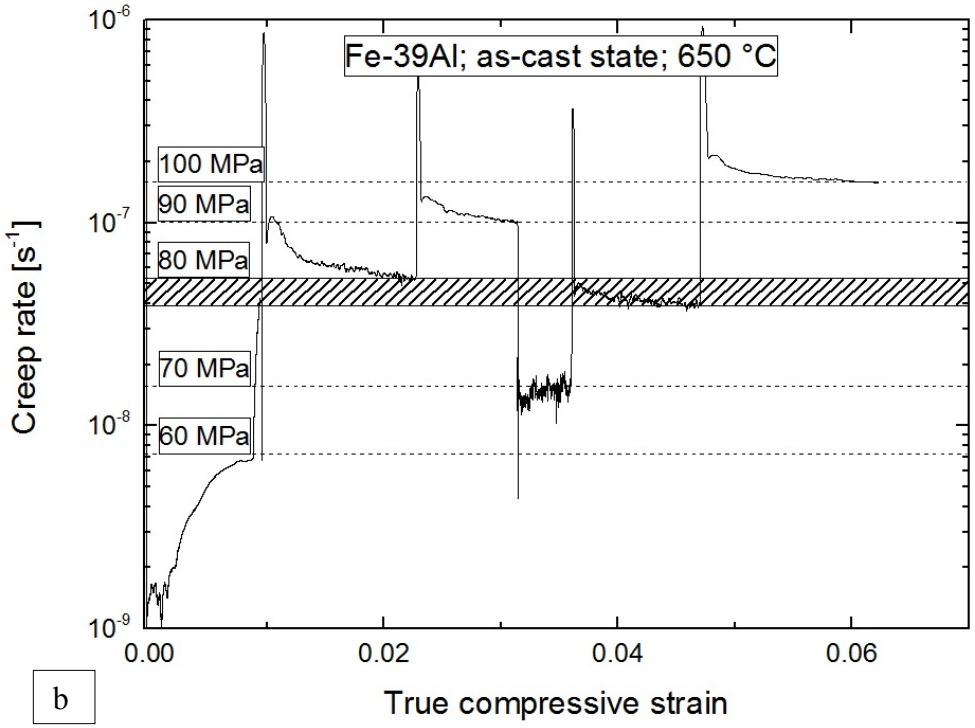

Figure 6.3: Half-logarithmic plot of creep rates as a function of strain at 650 °C for alternating stresses a) Fe-27Al b) Fe-39Al.

Steady-state creep rates are marked by dashed lines for each stress level. Thereby the creep rates just before a jump to the next stress level are used for evaluation as they are most closely to the steady-state creep rate, because they experienced the highest amount of strain. Some levels of stress were established multiple times to estimate whether the assumption of a constant microstructure including the dynamic equilibrium between strain hardening and recovery is fulfilled in this so-called steady-state creep rate regime. These levels of stress and corresponding creep rates are marked by striped rectangles in Figure 6.3a and b. In doing so, the deviations in the steady-state creep rate for a given stress are minor being in the range of $1 - 2 \cdot 10^{-8}$ s^{-1} and therefore, "true" steady-state conditions may have been achieved.

After a steady-state creep rate is established for a given applied stress, a jump from one stress level to another does not result in an instantaneous new steady-state creep rate, because $\rho_d \sim \sigma^2$ and a certain amount of strain is required to establish the new constant dislocation density again. Thereby smaller jumps in stress levels establish steady-state creep rates after lower strains, because dislocation densities of the two stress levels lie closer together. These stages of transient creep are considerably different for Fe-27Al and Fe-39Al (see Figure 6.3a and b).

An increase in stress is followed by an immediate jump in the strain rate in Fe-39Al, which then decreases continuously until the dislocation substructure has adapted to the new steady-state. This behavior is called normal transient creep, class M ((pure) metal type) creep, in literature [197][218]. By contrast, a stress increase in Fe-27Al causes the strain rate to increase continuously until the new steady-state level is achieved. Consequently, we call this behavior inverse transient creep, class A (alloy type) creep [219-221]. This fundamentally different behavior will now be rationalized as follows. There are two competing mechanisms over this stress and temperature range, dislocation climb and glide, which determine the rate of plastic deformation [218]. In class A alloys the dislocations interact in several possible ways with the solute atoms, and their movement is impeded, so that the rate of glide is slower than the rate of climb [202][222]. Inverse transient creep is typically observed in class A alloys and thus viscous glide of dislocations is rate controlling [220][221]. The large difference in dislocation speed between dislocations with and without solute clouds has been verified experimentally [223]. Cottrell et al. proposed a commonly used model that the drag process is caused by segregation of solute atmospheres to moving dislocations [224]. The velocity of dislocation moving by viscous glide is then of the form:

$$v = \frac{\sigma \cdot b}{\Gamma} \tag{6.7}$$

where Γ is a constant depending on temperature. In case of drag of the Cottrell atmosphere, Γ is quantified for an edge dislocation by [224]:

$$\Gamma = \frac{\mathrm{B}e^2 c}{D_i} \tag{6.8}$$

B*:* *Constant*

e: *Solute-solvent size difference*

c: *Concentration of solute atoms*

D_i*:* *Inter-diffusion coefficient for solute atoms*

Equation 6.7 shows that the stress necessary for dislocation motion at a given velocity increases with Γ. Other viscous drag processes such as Suzuki effect, Fisher's mechanism, and Snoek mechanisms are summarized in [195][218]. Detailed analysis of more than twenty class A alloys by Langdon et al. led to an approximation for the criterion for deformation by viscous glide [225]:

$$\frac{C\sigma^2}{\mathrm{k}^2(1-\vartheta)}\left(\frac{\gamma}{Gb}\right)^3 > \frac{T^2}{e^2 c b^6} \tag{6.9}$$

C: *constant* $\approx 8 \cdot 10^{12}$

ϑ*:* *Poisson's ratio*

γ*:* *Stacking fault energy*

Equation 6.9 was mainly derived for fcc alloys. Regarding B2-order in the present alloys one has to take into consideration to substitute the stacking fault energy by the APB energy since dislocations (110) <111> dissociate into ½ a<111> + APB + ½ a<111> at low temperatures and transitions to the slip direction from <111> to <001> beyond T_H=0.44 [197][226]. In class M alloys, which exhibit normal transient creep as in the case Fe-39Al, the rate of climb is faster than the rate of glide and thus rate controlling [218]. Hence, the activation energy for creep has been found often to be about that of lattice self-diffusion [197].

Regarding only the chemical composition of the alloys investigated in this work an answer whether an alloy is class M or A cannot be given easily. Therefore, further considerations have to be taken into account: i) as the investigated alloys are both within the B2 phase field during creep conditions, the degree of order of Fe-27Al has to be lower as it is further away from the stoichiometric composition of FeAl. The higher degree of B2-ordering at higher aluminum contents is also supported by the higher integral intensity of the B2-α transition in the corresponding DSC curves (see Figure 3.13). Hence, the lattice positions of iron and aluminum in Fe-27Al are more randomly occupied, resulting in more solid-solution characteristic behavior as compared to Fe-39Al. This should result in a higher value of *c* for Fe-27Al in Equation 6.9 ii) the solubility of micro-alloying elements in the matrix of Fe-27Al is higher than in Fe-39Al (see Table 3.4). This further increases the value of *c*. iii) the fraction of unlike atom bonding is lower in Fe-27Al compared to Fe-39Al, which decreases the value of shear modulus by 20 % at 650 °C (see Figure 6.4).

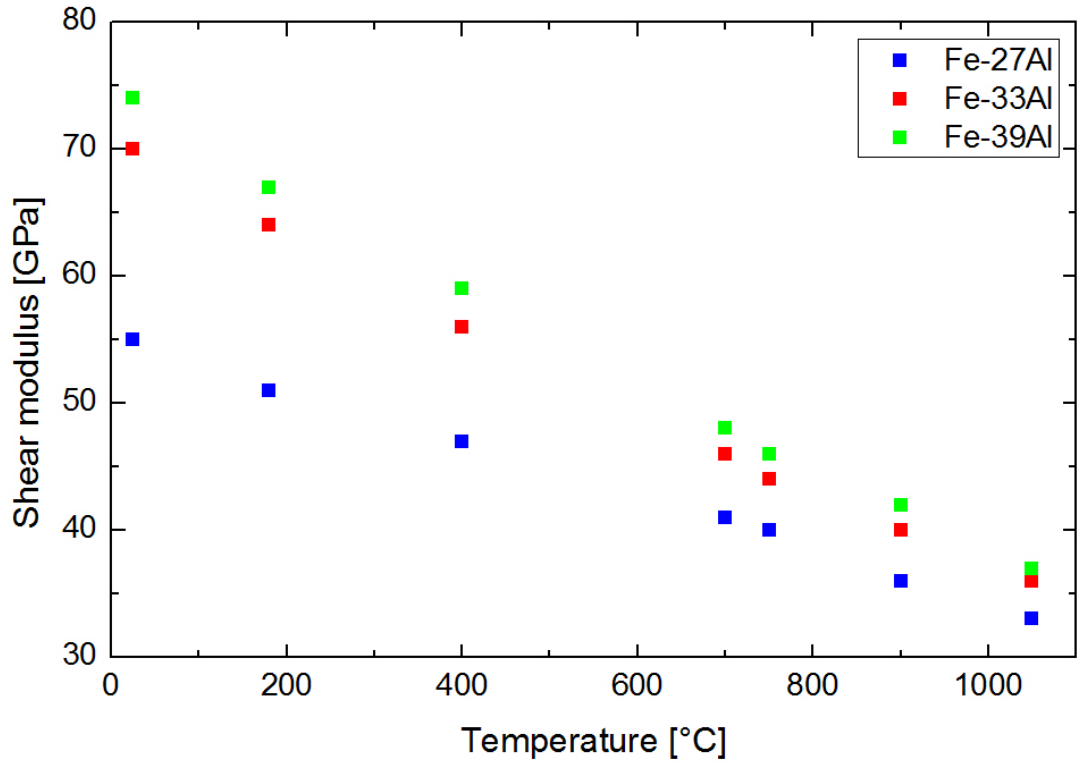

Figure 6.4: Shear modulus vs. temperature of investigated alloys.

This also benefits class A behavior of Fe-27Al, as the inverse shear modulus increases the probability of glide controlled creep by the power of three (see Equation 6.9). An influence is also given by the APB energy as discussed above. The APB energy is the energy increase per unit area traversed by the dislocation, due to the replacement of right bonds by wrong bonds and can be estimated by the product of shear modulus and ordering parameter [156]. Therefore a higher ordering parameter might be estimated for Fe-39Al as discussed in the previous subsection i). However, exact values of APB energies related to the investigated alloys are not available. In contrast to the variables discussed above, the higher Poisson's ratio of Fe-39Al (0.32 at 650 °C) compared to Fe-27Al (0.22 at 650 °C) does promote class A behavior for Fe-39Al. However, the influence of the Poisson's ratio in Equation 6.9 is rather small. The values of *e* and *b* are assumed to be equal for both alloys as the lattice constant for binary iron aluminides is almost invariant over the composition range of 27 – 39 at.% Al [12]. All alloy specific influencing factors in Equation 6.9 discussed above and the shape of the creep curves in Figure 6.3 lead to the conclusion that Fe-27Al can be treated as class A alloy, whereas Fe-39Al shows the characteristics of class M metals. The effect of class M/A behavior on the stress exponent is not clear yet. This will be discussed next with the aim of a Norton plot of the investigated alloys (see Figure 6.5).

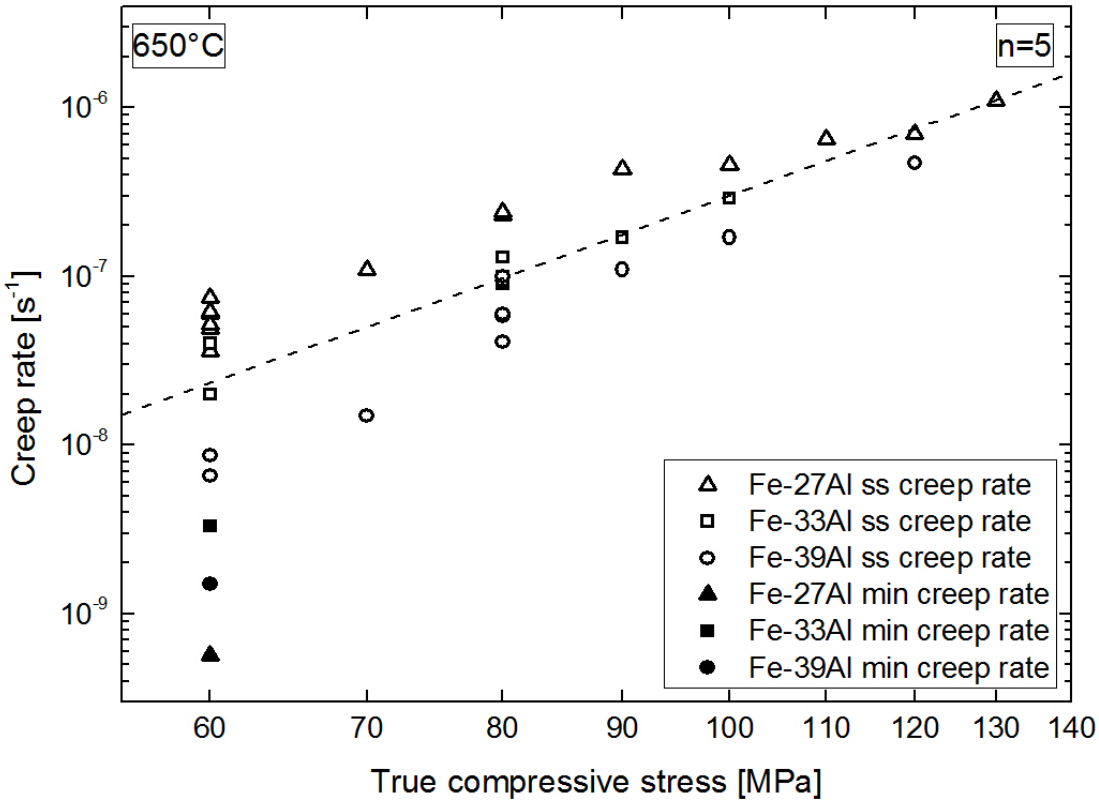

Figure 6.5: Norton plot for steady-state (ss) and minimum (min) creep rates at 650 °C.

The minimum creep rates collected in the very early stages of creep of the as-cast samples (see Figure 6.5) are indicated by full symbols. They will be discussed separately in Chapter 6.4.3. Most of the data points were collected at 60 MPa, which was used as reference stress level as described in the previous Chapter. Taking into account the moderate scatter of the data points at 60 MPa, the average stress exponent for all alloys is $n \approx 5$. This stress exponent indicates first, that dislocation creep is the rate determining process, which was expected due to the values of $T_H \approx 0.5$ and $\sigma/G \approx 10^{-3}$. Literature data on binary and ternary FeAl with the nearly the same Al contents also exhibits values of stress exponent within this range [93][207][211][227]. The general tendency of lower creep rates at higher aluminum contents are a result of the higher ordering with increasing Al content, which results in a higher value of shear modulus as shown in Figure 6.4. Moreover the self-diffusion coefficients decrease slightly at higher aluminum contents within the B2-ordered region [228]. The other factors (Burgers vector, grain size, grain size exponent, and stress exponent) influencing the steady-state creep rate given in Equation 6.6 can be assumed to be equal in the investigated alloys. Second, class M behavior is often attributed to n=5 and class A to n=3 in literature [195][197][225]. However, Blum found strong deviations from this rule [186]. In Al, a clear effect of purity has been established, with n increasing strongly with impurity content [186].

A stress exponent of n=3 has been found in high purity LiF single crystals and has been confirmed by stress change tests on individual specimens [204]. A trend regarding values of stress exponent related to class A/M behavior was not found in this work (as described above).

Finally, the steady-state creep rates obtained in this study were compared to those of binary iron aluminides in Figure 6.6. It can be concluded that micro-alloying of the investigated alloys result in creep rates, which are on a lower level by one order of magnitude compared to binary FeAl (see Figure 6.6).

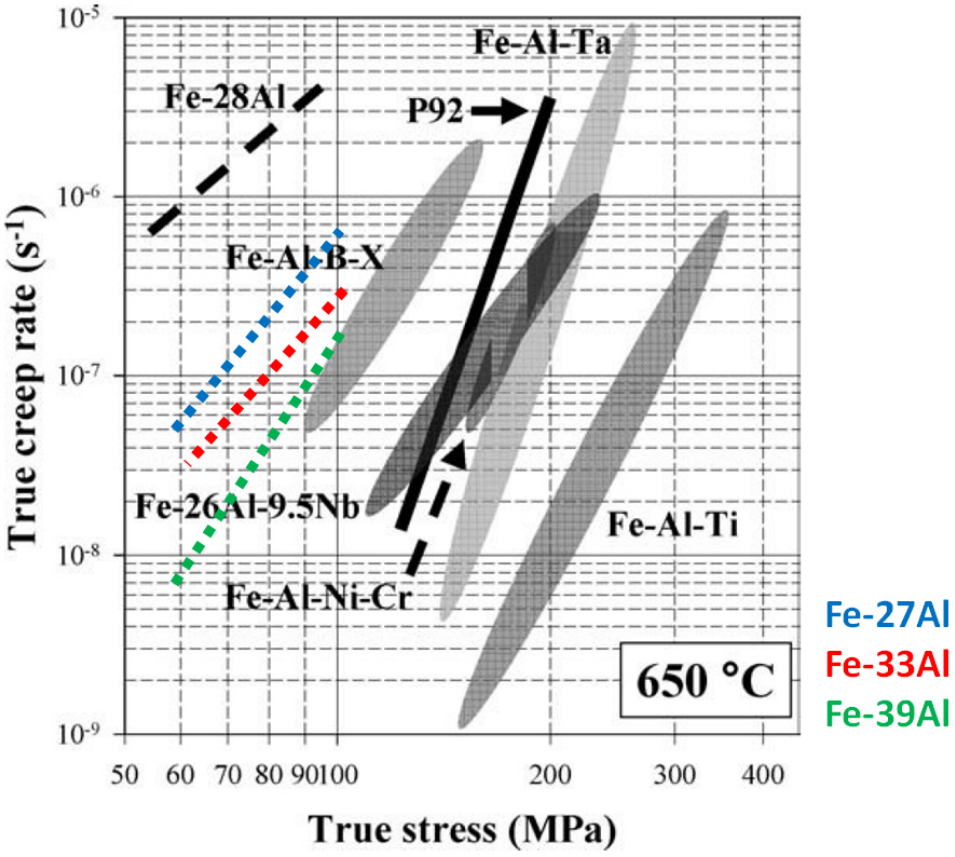

Figure 6.6: Comparison of the secondary creep rates of the various Fe-Al-X alloys with those of binary Fe-28Al [62] and P92 [229] at 650 °C [4][76]. Own data are plotted in blue, red and green colors, respectively.

In addition, our creep data were compared to those of other multiphase FeAl alloys as well as to high temperature steels. The creep rates of the investigated alloys are in good agreement to other micro-alloyed FeAl alloys containing borides. Whereas higher alloyed FeAl alloys exhibit a higher creep resistance, same as P92. P92 is a martensitic/ferritic 9-wt.% Cr steel which is mainly strengthened by carbide precipitates and which is considered as one of the most advanced ferritic creep resistant steels for steam turbine applications [229]. The best

performance (lowest minimum creep rates) is shown by Ti-rich FeAl alloys with a $L2_1$-ordered microstructure investigated by Heilmaier et al. [76]. However, these alloys are rather brittle and exhibit BDTT's ≥775 °C [76].

6.4.2. Effect of temperature

The effect of creep temperature in the range of 625 – 700 °C on the steady-state creep rates was investigated similarly by alternating the temperature during creep experiments at a constant stress level of 80 MPa during the creep experiments. The log $\dot{\varepsilon}_{ss} - \varepsilon$ plots for Fe-27Al and Fe-39Al are shown in Figure 6.7a and b in the range of 625 – 700 °C at 80 MPa, respectively.

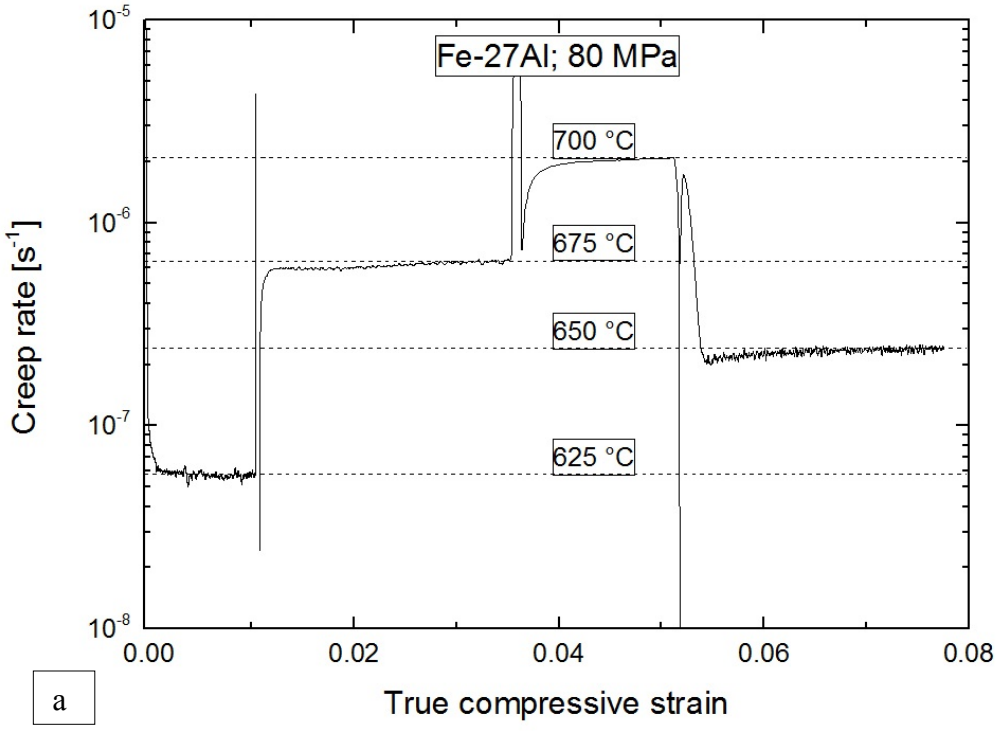

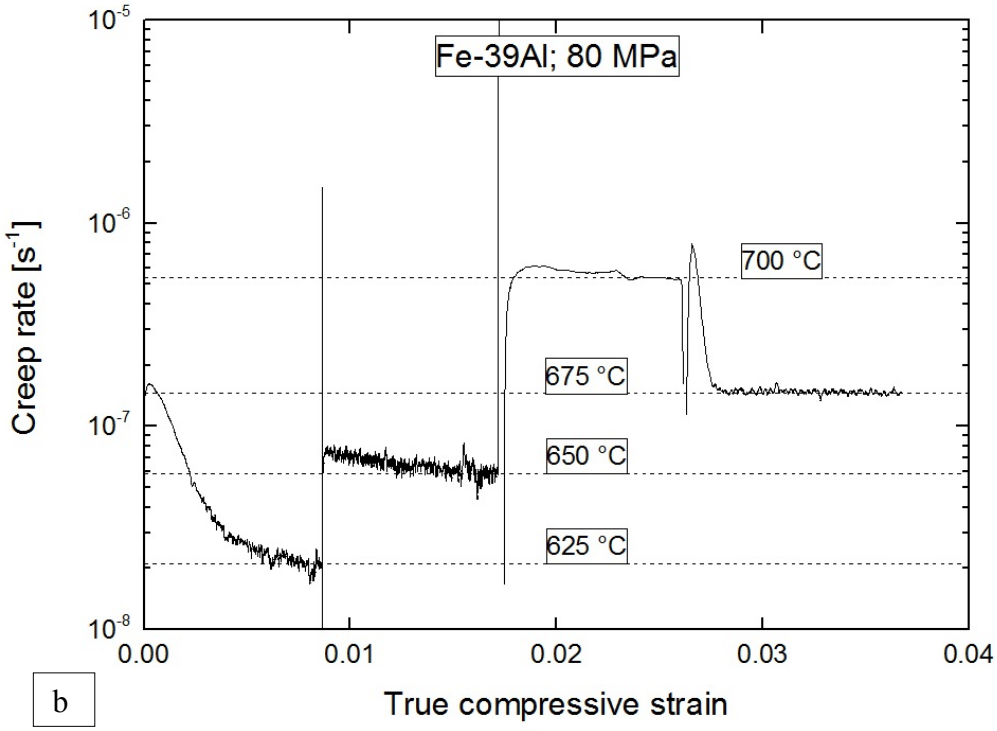

Figure 6.7: Half-logarithmic plot of creep rates as a function of strain at 80 MPa for alternating temperatures a) Fe-27Al b) Fe-39Al.

Dashed lines for a given temperature again mark the steady-state creep rates. The alloys show again the class M and A behavior in the transient creep regime after a change in temperature as discussed in the previous Chapter. Regarding Equation 6.10 it is convenient to plot $ln(\dot{\varepsilon}_{ss})$ against *1/T*, thus, fitting the creep rate to an Arrhenius law to determine the activation energy for creep:

$$\dot{\varepsilon}_{ss} \propto e^{\left(-\frac{Q}{RT}\right)} \tag{6.10}$$

where Q is proportional to the slope of the $ln(\dot{\varepsilon}_{ss})$ against $1/T$ plot. Over the range of temperature and strain rate in Figure 6.8 a single mechanism of creep seems to prevail with similar activation energies (Q_{ss}), which is indicated by the straight line for each alloy.

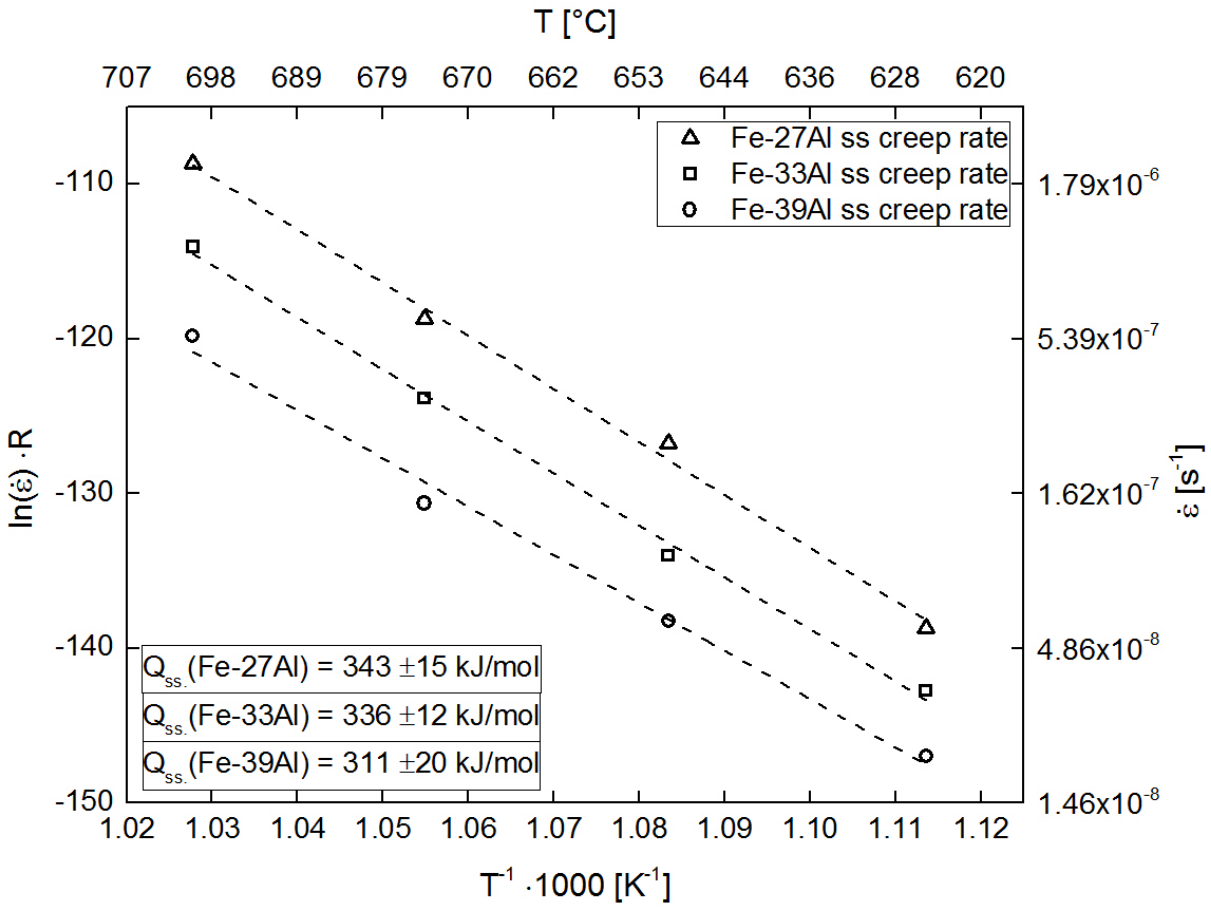

Figure 6.8: Arrhenius plot and corresponding activation energies in the steady-state creep rate regimes determined for an applied stress of 80 MPa.

The activation energies are within the range for B2-ordered iron aluminides in literature [93][156][205][207][227][230]. The activation energies for self-diffusion of ^{59}Fe in B2-ordered iron aluminides with the same aluminum contents are on a lower level of 230 –

250 kJ/mol [228]. Higher activation energy for creep in contrast to self-diffusion energy of iron might be related to the fact that the alloys are two-phase alloys, which is known to increase the activation energy for creep [202]. Moreover, the microstructure of iron aluminides (in terms of defect structures, density of vacancies, and state of order of the FeAl matrix phase) which influences the creep behavior is known to be a sensitive function of cooling conditions and heat treatments as described in Chapter 3.1.1. This might explain larger deviations of activation energies found in literature [211].

6.4.3. Kinetics of the as-cast state

Alloys creep tested in the as-cast state showed an unexpected behavior during the transition from stage I into stage II before the first steady-state creep rate is established. Between stage I and II a distinct minimum creep rate is observed, which can last up to several 100 hours but the achieved strains in this regime are far below 1.5 % and, therefore, these creep rates are not considered steady-state creep rates (see Figure 6.9a and b).

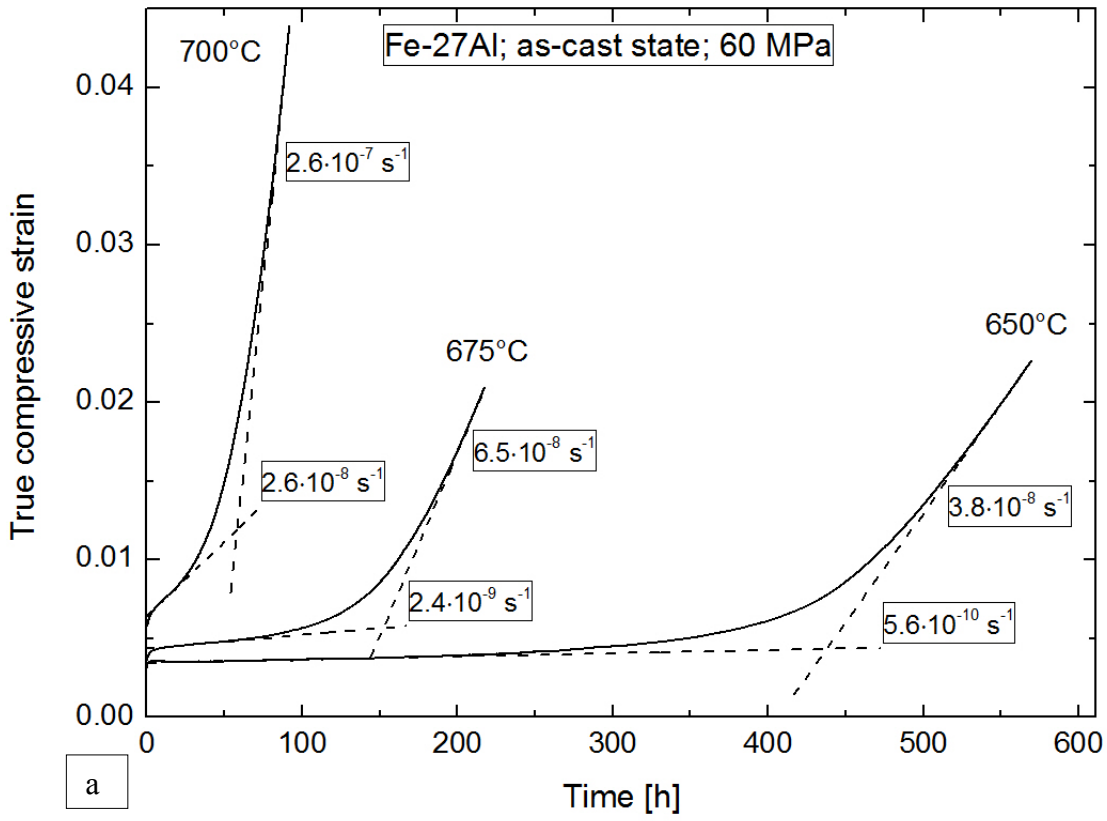

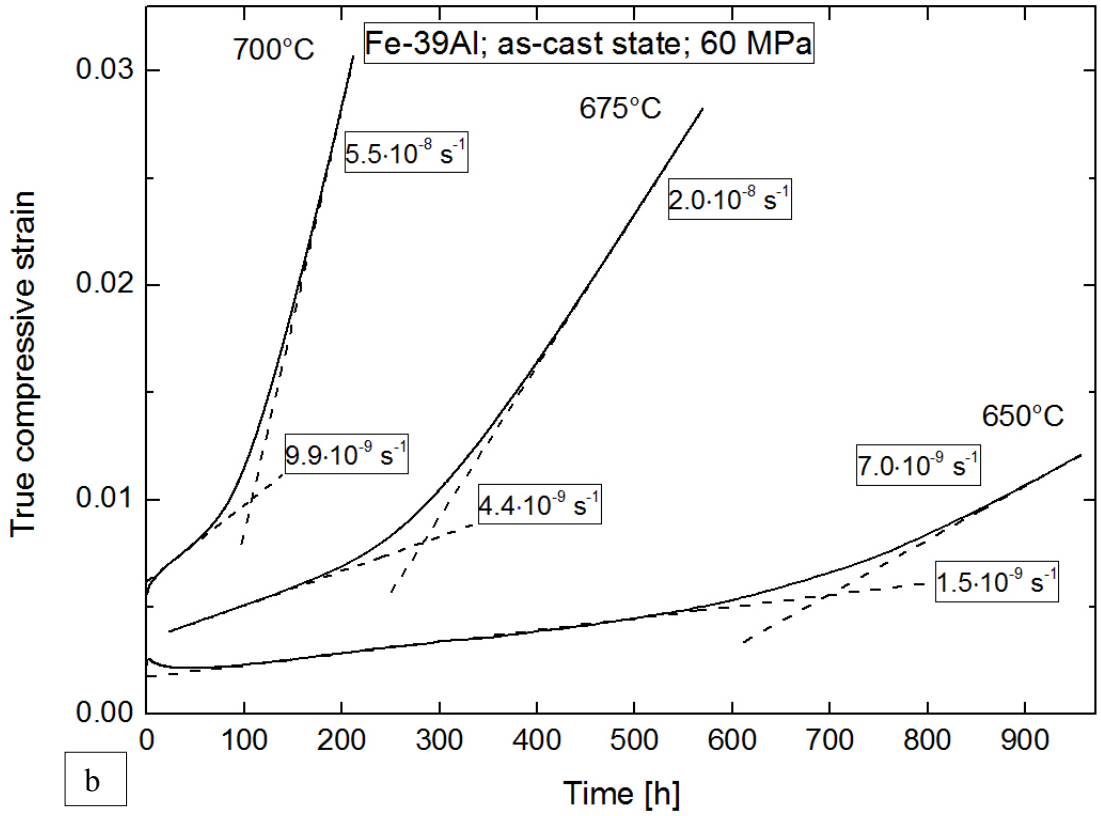

Figure 6.9: ε-t plots in the range of 650 – 700 °C and 60 MPa labeled with corresponding creep rates for alloys in the "as-cast" state; a) Fe-27Al b) Fe-39Al.

The duration within this minimum creep rate regime is decreasing at higher temperatures and is in general shorter for Fe-27Al as compared to Fe-39Al. Apart from the test parameters already mentioned, the dislocation density and structure needs to be constant to achieve a steady-state creep rate. There are many possibilities of kinetically delayed microstructural changes that can result in a nonlinear shape of the creep curve after region I, especially in complex alloys. The reasons may be: phase transitions, precipitation or dissolution of phases, processes driven by the minimization of interfacial energies (grain growth, Ostwald ripening, morphology changes of phases), formation of sub-grains, and so on. All these possibilities have in common that the present microstructure during creep is not in thermodynamic equilibrium state but approaching it with time. Therefore, kinetics are faster at higher temperatures and thermodynamic equilibrium is achieved earlier. Regarding Equation 6.1 the microstructural changes might be stress, strain, or temperature induced. A previous heat treatment of the alloys before creep testing for durations until a steady-state creep rate is established at corresponding creep temperatures resulted in an absence of the distinct minimum creep rate and the steady-state creep rate was established immediately (compare Figure 6.10a and b).

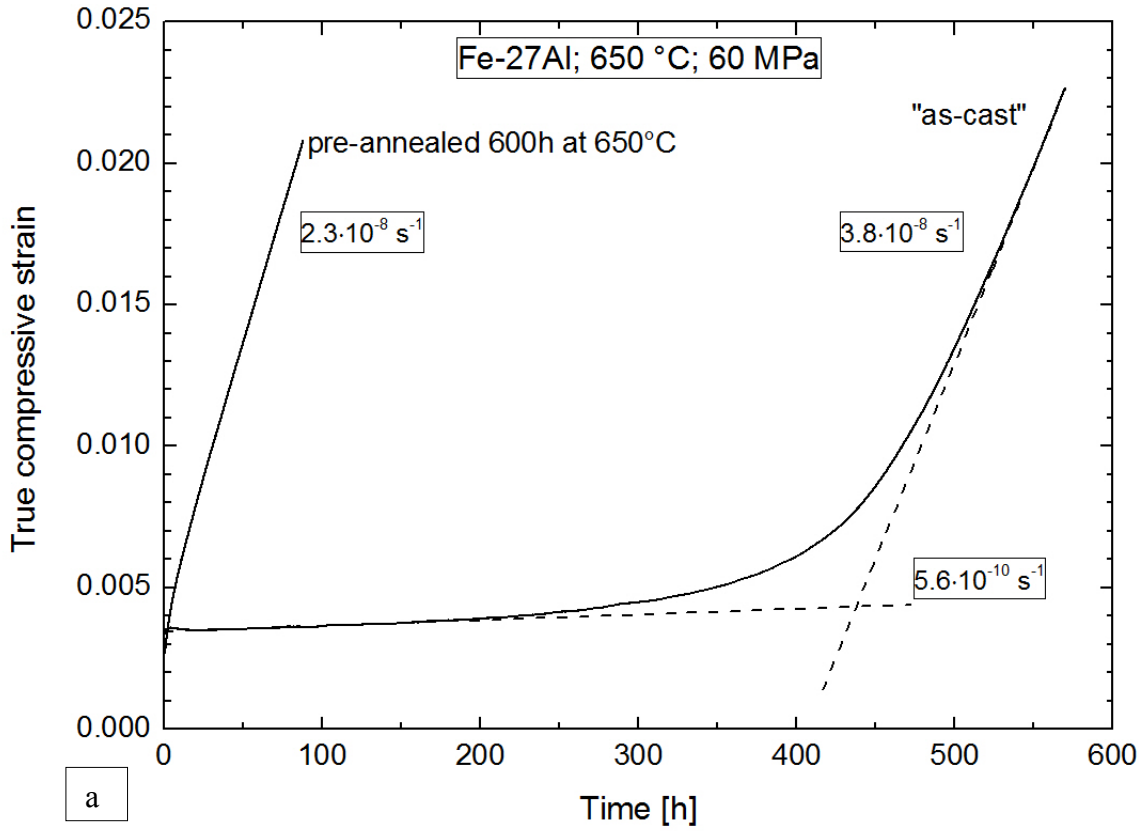

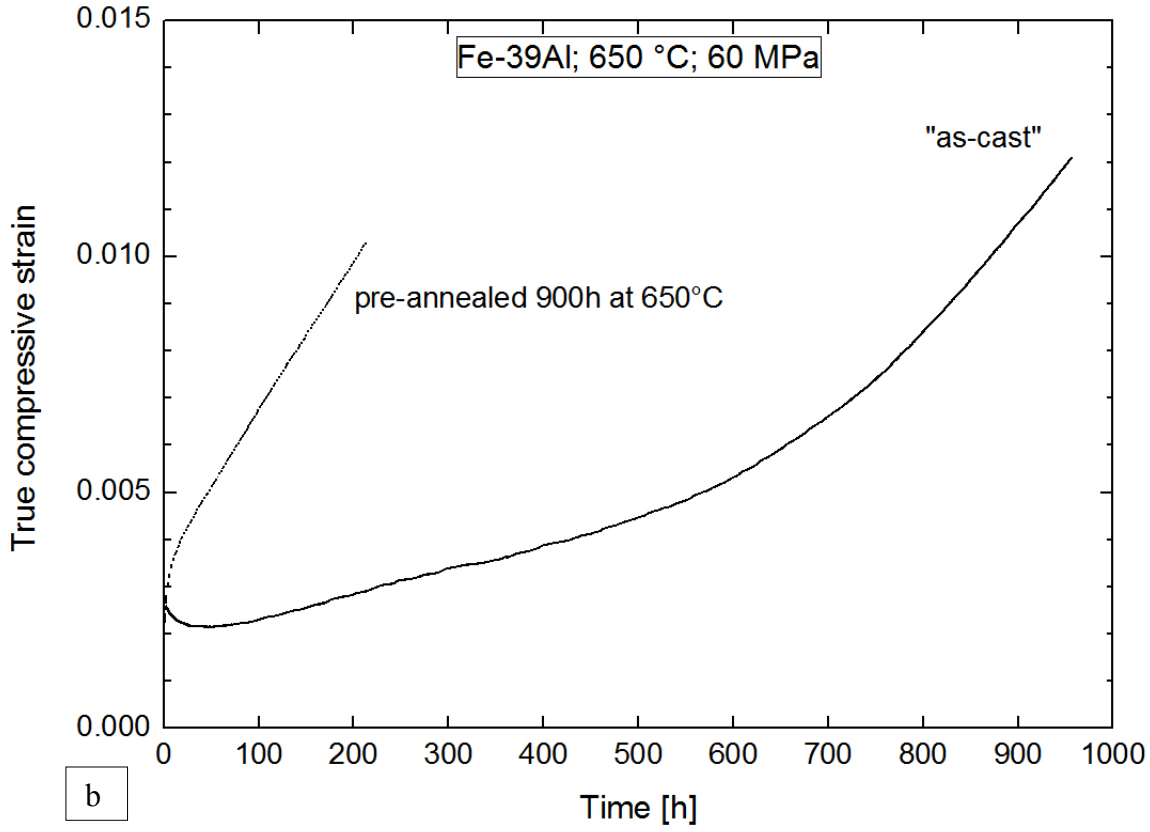

Figure 6.10: ε-t plots at 650 °C and 60 MPa for a) Fe-27Al in the „as-cast" state and pre-annealed at 650 °C for 600 h b) Fe-39Al in the „as-cast" state and pre-annealed at 650 °C for 900 h.

This indicates that the transition from minimum to steady-state creep rate is neither stress nor strain induced, but a function of time at high temperature exposure. Microstructural investigations of dendrite arm spacing and distribution of precipitates on a macroscopic scale did not reveal any discrepancies for Fe-27Al in the as-cast state in contrast to cross-sections of a crept sample in the steady-state creep rate regime (compare Figure 6.11a and b). The grain boundaries are pinned by thermodynamically stable precipitates and the dendrites did not show any coarsening effects.

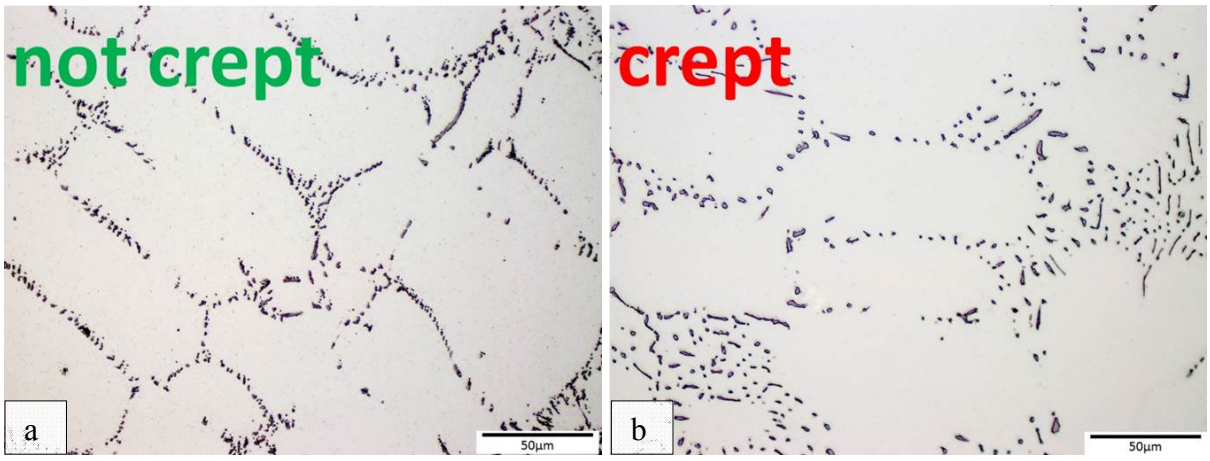

Figure 6.11: Microstructure of Fe-27Al (imaged by light microscopy) a) in the "as-cast" state without prior deformation b) crept at 650 °C for 800 h and a total achieved strain of 0.13.

As the microstructure on a macroscopic scale showed no differences, TEM investigations on the micro-scale were exemplarily carried out inside the dendrites of Fe-39Al. Two crept samples were analyzed by TEM: One creep experiment was stopped after 100 h (650 °C and 60 MPa) in the minimum creep rate regime. The other creep experiment was stopped after 1220 h in the steady-state creep rate regime at the same conditions. In the minimum creep-rate regime the formation of Moire fringes was observed indicating the early stage of precipitation (see highlighted area in Figure 6.12a). The superposition of 2 lattices (rotated to each other) produces Moire fringes of the coincident site lattice.

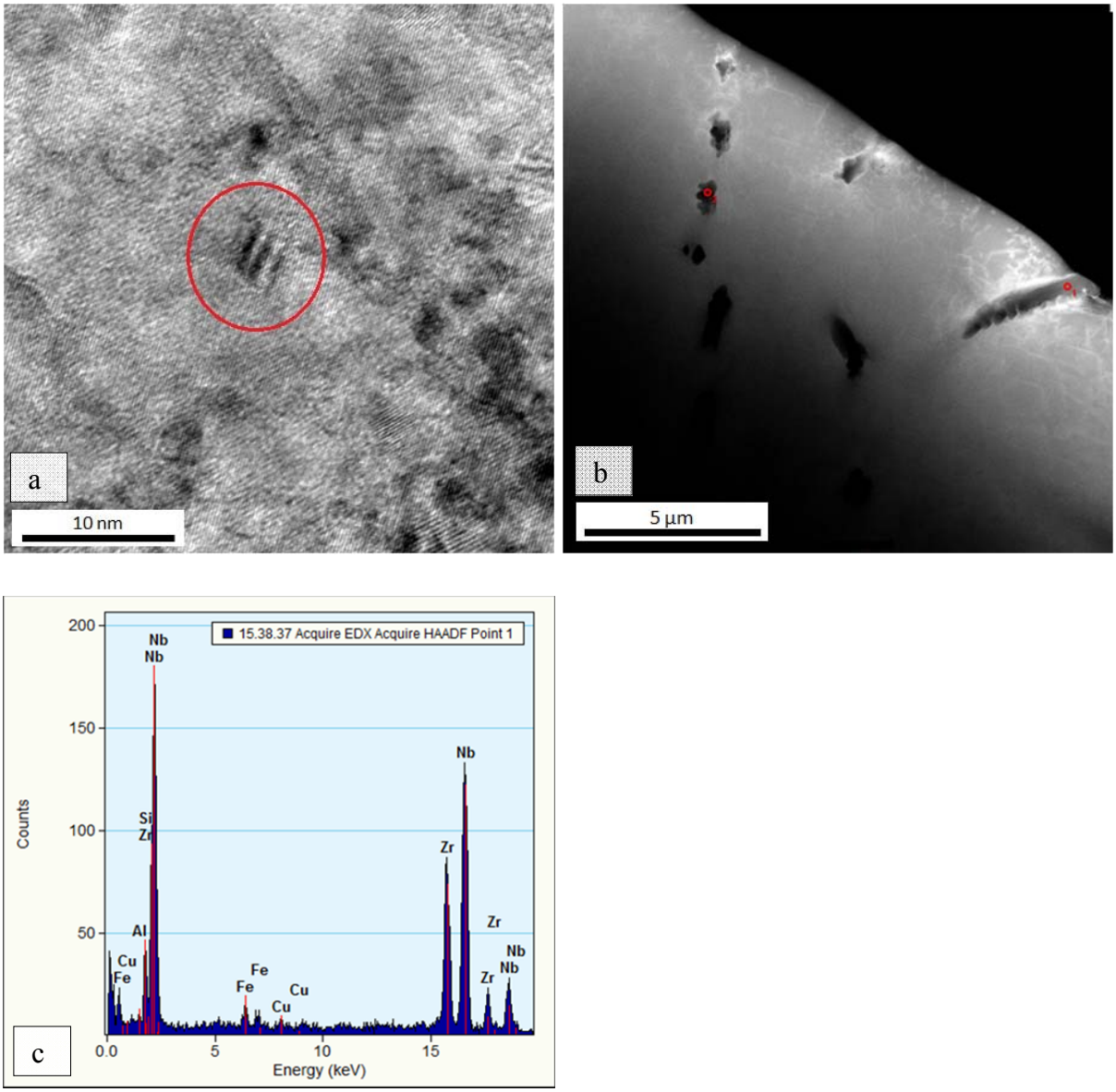

Figure 6.12: Microstructural observations by TEM of crept Fe-39Al after creep testing at 650 °C and 60 MPa true stress in the "as-cast" condition a) after 100 h (in the minimum creep rate regime) showing Moire fringes (imaged by HRTEM) b) after 1220 h (in the steady-state creep rate regime) showing coarse precipitates and dislocations (imaged by LAADF). c) EDX-measurement of the precipitates shown in b).

In the steady-state creep rate regime Moire fringes are no longer present, but relatively coarse and unevenly distributed precipitates are visible (see Figure 6.12b). A chemical analysis of these precipitates is given in Figure 6.12c, which indicates that they are chemically akin to those in the interdendritic regions (see Figure 3.11). With respect to the overall creep strength of the alloys it can be concluded that two competing mechanisms take place simultaneously in the as-cast state before a first steady-state creep rate is established: i) the depletion of micro-alloying elements in the FeAl matrix resulting in solid solution softening and ii) the formation

of precipitates resulting in strengthening. An approximation for the increased Orowan stress by precipitation hardening for FeAl alloys is given by the following equation [231]:

$$\sigma_{OR} = \frac{6.3ln(\phi/2b)}{\lambda-\phi} \quad (6.11)$$

σ_{OR}: *Orowan stress*

ϕ: *Strengthening particle size*

λ: *Inter-particle separation*

For reasonable particle strengthening of 100 MPa by the measured particle size of ≈1 µm (see Figure 6.12b) an inter-particle spacing of 1.25 µm (equivalent to a volume fraction of 50 %) is required [231]. The fraction of the precipitates in Figure 6.12b is far below 50 % and moreover unevenly distributed. Thus, the effect of these precipitates on impeding dislocation motion can be considered to be negligible. The coupled depletion of alloying elements inside the FeAl matrix cannot be calculated quantitatively because a certain amount is present in the precipitated state. Further the image section in Figure 6.12b is too small to be considered representative. However, Morris showed that 2 % niobium in Fe-25Al (single-phase alloy) increased the yield strength to 400 MPa at 600 °C in contrast to a binary alloy (100 MPa at 600 °C) [232], indicating the effectiveness of niobium as a solid solution strengthener due to its atomic size misfit with iron (see Figure 3.4). Although the amount of niobium in solid solution is lower in the alloys investigated here, it has been identified as the primarily responsible element for solid solution strengthening beyond zirconium, carbon, and, boron as described in Chapter 3.3. The depletion of alloying elements in the FeAl matrix is therefore considered to be the cause for the observed softening of the alloys, which results in the steady-state creep rate when the equilibrium concentration in the FeAl matrix is established.

However, the creep data yield evidence that there are significant differences in the behavior of the Fe-33Al and Fe-39Al alloys as compared to Fe-27Al. First, the difference between minimum and steady-state creep rate is merely one order of magnitude for Fe-33Al and Fe-39Al, whereas Fe-27Al exhibits a difference of two orders of magnitude at 650 °C (see Figure 6.5). The minimum creep rate of Fe-27Al is even below the minimum creep rate of Fe-39Al, although the steady-state creep rates of Fe-39Al are below those of Fe-27Al. This raises the question where this additional reduction in minimum creep rate (hardening) in Fe-27Al might come from. An indication is given by the activation energies for creep in the minimum creep rate regime. The activation energies for minimum and steady-state creep in Fe-39Al do not vary (compare Figure 6.8 and Figure 6.13, respectively). By contrast, the

activation energy for creep is twice as high for Fe-27Al in the minimum creep rate regime (see Figure 6.13).

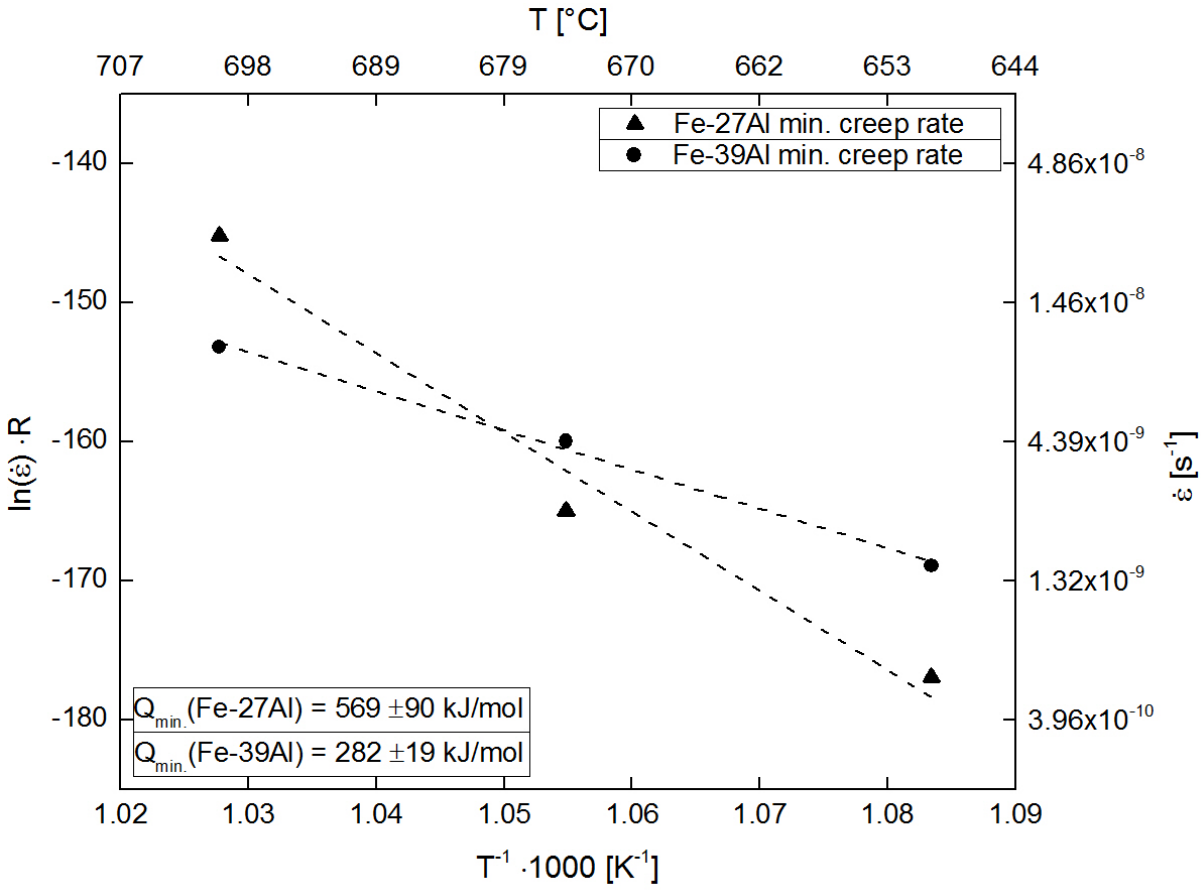

Figure 6.13: Arrhenius plot and corresponding activation energies in the minimum creep rate regimes determined for an applied stress of 60 MPa.

In evaluating these data it should be considered that the activation energies in the steady-state regimes (Figure 6.8) were determined over a larger strain and temperature range than those referring to minimum creep rate regimes. Therefore, the activation energy for creep in the steady-state creep rate regime could be determined with higher precision.

Cahn pointed out that the effect of order on creep resistance of intermetallics might be attributed to two factors [233]: i) the slowing down of self-diffusion when long range order is established and ii) the effect of ordering energy on slowing down viscous motion of dislocations on the slip plane. The ordering energy can be regarded as equivalent to the work needed to convert an ordered alloy into disordered one [233]. The first argument can be ruled out for the investigated Fe-27Al alloy and in general for Fe_3Al alloys, as the activation energy for self-diffusion of Fe in Al is 278 ±5 kJ/mol in the $D0_3$-ordered state [228]. Activation energies for inter-diffusion of Fe and Al in FeAl [234] and Al in Fe [235] are even on a lower

level. Therefore, the second argument seems to be more reasonable as the investigated Fe-27Al alloy shows "class A" behavior where the creep rate is determined by viscous glide of dislocations as discussed in Chapter 6.4.1. The dominating effect of ordering energy on the creep resistance in class A intermetallic alloys may be related to the motion of superdislocations. A gliding dislocation leaves behind an antiphase boundary (APB). An APB is an area in the crystal lattice where the atoms are arranged in the opposite order to those in the perfect ordered lattice [155]. Order is than restored by a second dislocation, which takes the respective atoms back to their original positions in the crystal structure. The ordering energy is then proportional to the separation distance of the partial dislocations within a superdislocation [233]. The latent heat of $D0_3$-ordering is superimposed to B2-ordering as shown in Figure 3.14, which can confirm the trend of higher activation energies if $D0_3$-order is present. The activation energy of almost 600 kJ/mol (see Figure 6.13) is characteristic for the creep of $D0_3$-ordered Fe_3Al as demonstrated by Lawley [156]. The activation energy for creep in $L2_1$-ordered (ternary equivalent of $D0_3$-order) Fe-Al-Ti alloys is also in this range (400 – 600 kJ/mol [75]) confirming the effect of crystallographic order on the activation energy for creep. However, for Fe-27Al the estimated $D0_3$-B2 phase transition temperature $T_C(D0_3\text{-B2})$ of 545 °C by DSC measurements is approximately 100 °C below the temperature of our creep experiments (see Figure 3.14). $T_C(D0_3\text{-B2})$ is defined as the critical temperature where $D0_3$-order disappears completely. Starting from $T_C(D0_3\text{-B2})$ the $D0_3$-order is continuously increasing until temperatures of ≈ 200 °C below $T_C(D0_3\text{-B2})$ (depending on alloy composition) [64]. As imaged by in-situ heating experiments in TEM Morris et al. demonstrated that residual amounts of $D0_3$-ordered domains are present in niobium containing Fe-28Al-(0.8-1)Nb up to 200 °C above $T_C(D0_3\text{-B2})$ (identified by DSC and XRD measurements), by niobium additions remaining on their ordered lattice sites [236]. Morris concluded that this weak degree of $D0_3$-order which is retained at temperatures much higher than the nominal $T_C(D0_3\text{-B2})$ will clearly affect the mechanical properties at high temperatures. Also Hilfrich et al. found $D0_3$-order in Fe_3Al at temperatures up to 1050 K [237] and 1373 K [238] by neutron diffraction, clearly above the established $T_C(D0_3\text{-B2})$ values. A comparable study on β-brass shows a sharp increase of creep resistance close to T_C, where the appearance of small amount of order suffices to enhance the creep resistance by one order of magnitude, within a temperature range of only ≈15 °C [239]. As shown above, the difference in minimum to steady-state creep rate is almost one order of magnitude for Fe-33Al and Fe-39Al, whereas Fe-27Al exhibits a difference of two orders of magnitude at 650 °C (see Figure 6.5). The additional reduction in minimum creep rate in Fe-27Al might,

thus, be attributed to residual $D0_3$-ordering. Direct experimental support is given by Stoloff and Davies who showed already in 1964 in tensile tests at constant strain rate that a slight increase of $D0_3$-order strongly increases the flow stress at higher temperatures in Fe_3Al (see Figure 6.14) [240].

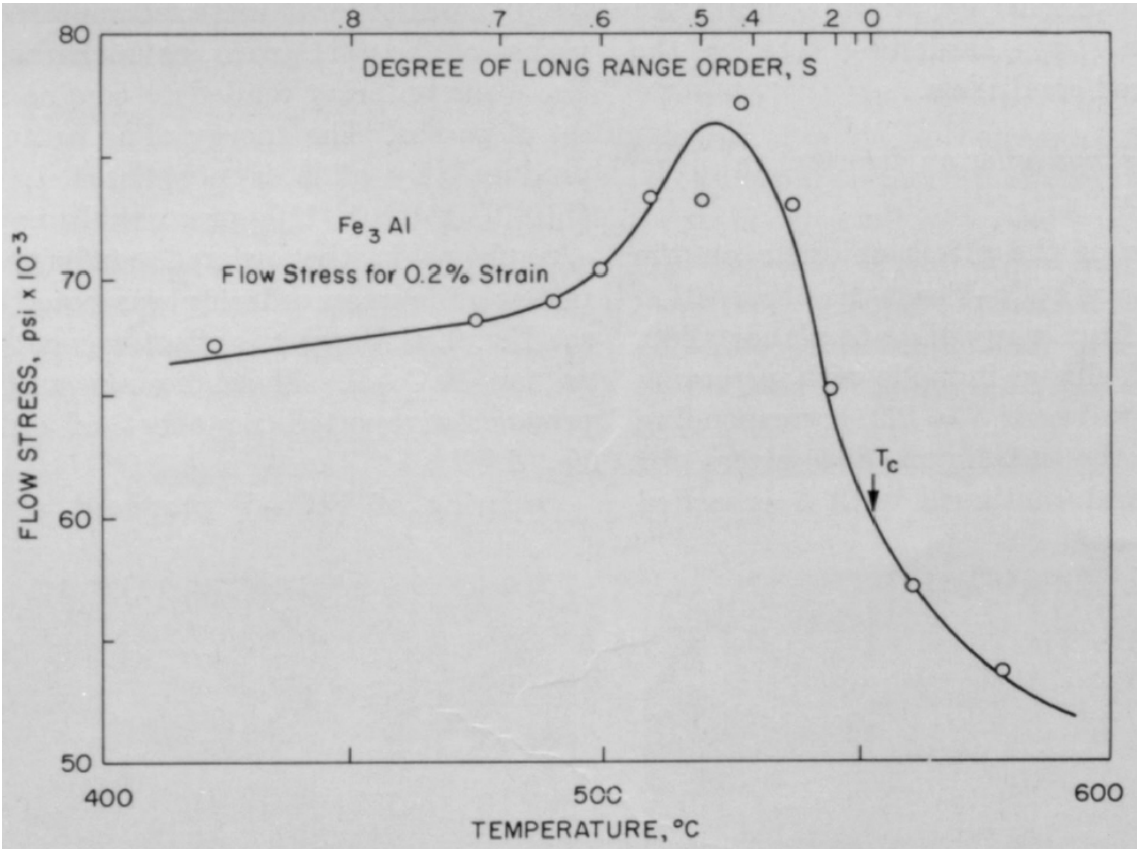

Figure 6.14: Dependence of flow stress of Fe_3Al on test temperature and corresponding degree of long range order (by Stoloff and Davies [240]).

The effect of niobium on residual $D0_3$-order can be rationalized by the creep data and microstructural investigations presented here, too. An antecedent heat treatment for depletion of niobium out of the FeAl matrix phase resulted in the absence of the minimum creep rate (see Figure 6.10a), because niobium is then already present in the precipitated state instead of stabilizing $D0_3$-order of the FeAl matrix phase. Moreover, the difference between minimum and steady-state creep rate at 700 °C is only one order of magnitude, whereas it is two at 650 °C (see Figure 6.9a). Hence, $D0_3$-order diminishes at higher temperatures in agreement with findings of Morris [236]. Cahn and Sauthoff could so far not reveal whether the activation energy for creep of $D0_3$-ordered Fe_3Al is related to self-diffusion or ordering energy, mainly due to lacking information on parameters for self-diffusion [233][241]. However, the result presented here gives clear evidence, that it is related to ordering energy.

6.5. Summary and conclusions

The creep behavior of Fe-27Al, Fe-33Al and Fe-39Al was investigated at temperatures between 625 – 700 °C by compressive creep tests. Fe-27Al showed typical “class A” behavior, whereas Fe-39Al exhibits “class M” characteristics. The steady-state creep rates are in good agreement with other micro-alloyed iron aluminides containing borides and carbides. Nevertheless, a distinct minimum creep rate was observed for alloys tested in the as-cast state before a steady-state creep rate was achieved. Evaluation of creep data and microstructural investigations revealed the mechanisms and kinetics responsible for the observed minimum creep rate. The following more specific results and conclusions were obtained:

The transition from minimum to steady-state creep rate is a result of continuous depletion of micro-alloying elements in the FeAl matrix and the subsequent formation of coarse and unevenly distributed precipitates. This process involves all alloys and results in an increase of creep rate by almost one order of magnitude. The kinetics of precipitation becomes slower as the aluminum content in the FeAl matrix phase increases. In Fe-27Al a second, superimposed effect was observed, which further decreased the minimum creep rate by an additional order of magnitude. This is attributed to residual $D0_3$-order that is promoted by the presence of niobium in the FeAl matrix phase. As high temperature in-situ TEM studies failed in this study because of technical reasons, only indirect evidence is presented for this theory:

I) The activation energy for creep is doubled in the minimum creep rate regime to almost 600 kJ/mol, which is characteristic for creep in $D0_3$-ordered Fe_3Al [156].

II) In general, the activation energy for creep is correlated to self-diffusion, whereas it is correlated to ordering energy for Fe-27Al in the minimum creep rate regime

III) The higher the creep temperature was the lower was the difference between minimum and steady-state creep rate as result of the lower amount of $D0_3$-ordered domains at higher temperatures.

IV) An antecedent heat-treatment for depletion of niobium out of the FeAl matrix phase resulted in the absence of the minimum creep rate.

A possible candidate for increased creep resistance could be a single-phase Fe-Al-Nb alloy, with niobium content close to the solubility limit. McKamey showed already, that a ternary Fe-28Al-1Nb (with a grain size of 80 µm) at 650 °C at 70 MPa exhibits a steady-state creep rate of $4.2 \cdot 10^{-7}$ s^{-1} [205], which is slightly higher than the value of $1.1 \cdot 10^{-7}$ s^{-1} for the Fe-27Al investigated here. The precipitate particles prevent grain coarsening during creep experiments

and exhibit only slight effect on ductility, which appears promising for future alloy developments. This was also demonstrated by Krein for akin microstructures in iron aluminides [109]. Based on the results presented here and information provided in the literature, a promising approach for a higher creep resistant Fe_3Al based alloy would be to maintain the amount of micro-alloying elements but to increase niobium content ≤2 at.%, to increase the amount of solid solution strengthening.

7. Summary and Outlook

The overall objective of this work was to contribute to an assessment of iron aluminides for structural applications within the context of turbochargers. Therefore micro-alloyed iron aluminides containing 27, 33, and 39 at.% aluminum were investigated in terms of oxidation behavior and mechanical properties. In order to make the different alloys as comparable as possible the micro-alloying elements (niobium, zirconium, carbon, and boron) were added in same concentrations. The oxidation behavior was characterized under cyclic conditions in the range of 700 – 1050 °C in air. Mechanical properties were investigated in creep experiments in the range of 625 – 700 °C and at room temperature as a function of strain rate (10^{-4} – 10^{3} s^{-1}). Summaries from a purely scientific point of view are given in more detail at the end of each corresponding Chapters 4, 5, and 6, respectively. The impact of the investigations on the BMWi-founded turbocharger project, which was introduced in the introduction, is given here.

On the turbine side of a turbocharger several components such as guide vanes, housings, and various attachments are exposed to high temperatures. Therefore the oxidation behavior was investigated under cyclic conditions. The oxidation behavior is strongly influenced by the micro-alloying elements. On one hand micro-alloying elements in the precipitated state deteriorate the oxidation by acting as starting points for internal oxidation. On the other hand micro-alloying elements in the FeAl matrix were beneficial to promote the formation of protective α-Al_2O_3 scales at lower temperatures instead of faster growing θ-Al_2O_3. The additional oxidation of a ternary Fe-Al-Nb alloy with notable amounts of Nb proofed that niobium promotes the formation of α-Al_2O_3 at temperatures below 900 °C. Further research is necessary to evaluate whether the proposed $Nb_2Fe_4Al_9$ is formed in the early stages of oxidation and acts as nucleation site for the growth of α-Al_2O_3. Therefore FIB target preparation and subsequent TEM analysis would be recommended. However, based on these results in can be concluded that certain turbocharger components can be made out of single-phase Fe-Al-Nb alloys, provided they are exposed to high temperatures without being subjected to too high mechanical stresses. Especially frequently moving parts such as guide vanes can ideally be substituted by Fe-Al-Nb alloys to reduce the probability of jamming by the formation of oxides on the surface. Here, the slow growing α-Al_2O_3 clearly superior to the faster growing and more voluminous chromium and titanium oxides.

The high temperature strength of structural parts, which are operated in the vicinity of 650 °C (which is about 0.5 – 0.6 T_H of the investigated alloys), was investigated by creep

experiments. The creep experiments showed an unexpected behavior for all alloys. Before a steady-state creep was established a pronounced minimum creep rate was observed. The transition from minimum to steady-state creep rate is accompanied by a loss in solid-solution hardening. Thereby niobium forms coarse and unevenly distributed coarse precipitates. In Fe-27Al this effect is superimposed by a continuous transition of $D0_3$-ordered domains into B2-ordered domains, which results in additional softening. A proof of the existence of these remanent $D0_3$-ordered domains at high temperatures was given indirectly. Additional attempts are needed for a direct proof of this theory by in-situ heating experiments in the TEM as described in Chapter 6. For structural parts it has to be considered that alloys in the "as-cast" state do suffer in strength at high temperatures after a certain period of time due to microstructural changes. The steady-state creep rates are much higher compared to state of the art nickel-based superalloys and γ-TiAl alloys. Hence, the combined stress and temperature conditions (T_H is beyond 0.7) of a turbine wheel are very likely too high for iron aluminides. The objectives for the compressor wheel in terms of strength (which were set by the project partners) were attained after marginal optimization of the original alloy composition. Therefore the niobium content was increased to 2 %, just below the solubility limit, for an additional amount of solid-solution hardening without making the alloy more complex, as previously recommended in Chapter 6.5 for increasing the creep strength.

For a housing of a turbocharger a high capability of energy absorption during impact is important, if a turbine or compressor wheel fails. Therefore the mechanical response was investigated over a wide range of strain rates between 10^{-4} and 10^{3} s^{-1} at room temperature. The stress-strain response did not vary at low strain rates in range of 10^{-4} – 10^{-1} s^{-1}. A further increase in strain rate towards dynamic loading resulted in a continuous increase in yield strength. A change in work hardening rates was not observed at low (≤0.1 s^{-1}) and intermediate strain rates (120 s^{-1}), but considerably lower work hardening rates were observed at highest strain rates of 10^{3} s^{-1}. In conjunction with the lowered work hardening rates at high strain rates twinning and shear localization were found as additional modes of plastic deformation in $D0_3$-ordered Fe-27Al. The detrimental effect of high strain rates on the work hardening rates of B2-ordered Fe-33Al and Fe-39Al are not fully clear yet. Post deformation analysis of the microstructure such as dislocation configuration by TEM and the possible occurrence of cracks investigated by X-ray tomography could clarify this task. However, calculations based on experimental results of density, specific heat, and stress-strain response showed that adiabatic heating could be excluded to be responsible for softening. The area below a stress-strain curve corresponds to the energy than can be transferred into heat by

plastic deformation. A ranking amongst the alloys with respect to the capability energy absorption cannot be given easily as the stress strain curves are seemingly different, related to the state of order of the FeAl matrix phase. The energy absorption capacity is larger in Fe-27Al at strains below 15 %. The capability for energy absorption of Fe-33Al and Fe-39Al alloys at larger strains is higher. Therefore impact experiments of projectiles and subsequent simulations are necessary to determine the local degree of strains, which appear during deformation of the turbocharger housing. For evaluation whether the housing on the turbine side could be made of iron aluminides, the temperatures occurring there must be determined and subsequent high-strain rate experiments at high temperatures are needed.

The research activities in the framework of the BMWi founded project have provided new knowledge according to FeAl alloys and their potential capabilities for turbochargers. Also recommendations of alloy compositions for several components of the turbocharger could be given. Further, our work resulted in three alloy-specific patents according to components of turbochargers [242-244].

8. References

[1] http://www.evsroll.com/History_of_crude_oil_prices.html, (2014).

[2] N.S. Stoloff, C.T. Liu, S.C. Deevi, Emerging applications of intermetallics, Intermetallics. 8 (2000) 1313–1320. doi:10.1016/S0966-9795(00)00077-7.

[3] M. Palm, Fe-Al materials for structural applications at high temperatures: Current research at MPIE, Int. J. Mater. Res. 100 (2009) 277–287.

[4] M. Palm, R. Krein, S. Milenkovic, G. Sauthoff, D. Risanti, C. Stallybrass, et al., Strengthening mechanisms for Fe-Al-based alloys with increased creep resistance at high temperatures, in: Adv. Intermet.-Based Alloy. Symp. Proc. Ser. Vol. 980, 2007: pp. 3–14.

[5] M. Heilmaier, D. Janda, Annex (TUD) - of the ZIM project: FeAl-Basislegierungen – Werkstoff, Giessprozess und Abgasturbolader, 2010.

[6] IMechE, 10th International Conference on Turbochargers and Turbocharging, Elsevier, 2012.

[7] A.S. Leĭzerovich, Steam Turbines for Modern Fossil-fuel Power Plants, The Fairmont Press, Inc., 2008.

[8] Personal communication of project partners, presented on a discussion meeting in Darmstadt, (2011).

[9] J.R. Davis, Heat-resistant Materials, ASM International, 1997.

[10] B. Fultz, J. Howe, Transmission Electron Microscopy and Diffractometry of Materials, Springer, 2007.

[11] ASM International Handbook Committee, ASM Handbook, Vol. 8, High Strain Rate Testing, 2000.

[12] U.R. Kattner, B.P. Burton, Phase diagrams of binary iron alloys, ASM International, 1993.

[13] M. Hansen, K. Anderko, Constitution of binary alloys, McGraw-Hill, 1965.

[14] O. Kubaschewski, Iron - Binary Phase Diagrams, Springer-Verlag, Berlin, 1982.

[15] M. Tb, O. H, S. PR, Binary Alloy Phase Diagrams, 2nd Edition, ASM Intl, Materials Park, Ohio, 1990.

[16] F. Stein, M. Palm, Re-determination of transition temperatures in the Fe-Al system by differential thermal analysis, Int. J. Mater. Res. 98 (2007) 580–588. doi:10.3139/146.101512.

[17] B. Köhler, J. Wolff, M. Franz, A. Broska, T. Hehenkamp, Investigation of point defect migration in Fe-Al alloys by means of fast Doppler broadening technique, Intermetallics. 7 (1999) 269–276. doi:10.1016/S0966-9795(98)00103-4.

[18] H. Thomas, Ueber Den Elektrischen Widerstand Von Heizleiterlegierungen Aus Eisen-Chrom-Aluminium, Z. Met. 41 (1950) 185–190.

[19] T. Hehenkamp, P. Scholz, B. Köhler, R. Kerl, Vacancy Formation and Diffusion in FeAl-Alloys, Defect Diffus. Forum. 194-199 (2001) 389–396. doi:10.4028/www.scientific.net/DDF.194-199.389.

[20] J.L. Jordan, S.C. Deevi, Vacancy formation and effects in FeAl, Intermetallics. 11 (2003) 507–528. doi:10.1016/S0966-9795(03)00027-X.

[21] C.G. McKamey, J.H. DeVan, P.F. Tortorelli, V.K. Sikka, A Review of Recent Developments in Fe3Al-Based Alloys, J. Mater. Res. 6 (1991) 1779–1805.

[22] C.T. Liu, E.P. George, P.J. Maziasz, J.H. Schneibel, Recent advances in B2 iron aluminide alloys: deformation, fracture and alloy design, Mater. Sci. Eng. A. 258 (1998) 84–98. doi:10.1016/S0921-5093(98)00921-6.

[23] H.-E. Schaefer, B. Damson, M. Weller, E. Arzt, E.P. George, Thermal Vacancies and High-Temperature Mechanical Properties of FeAl, Phys. Status Solidi A. 160 (1997) 531–540. doi:10.1002/1521-396X(199704)160:2<531::AID-PSSA531>3.0.CO;2-7.

[24] V.K. Sikka, S. Viswanathan, C.G. McKamey, Development and commercialization status of Fe3Al-based intermetallic alloys, in: Int. Symp. Struct. Intermet., TMS, 1993: pp. 483–491.

[25] A. Taylor, R.M. Jones, Constitution and magnetic properties of iron-rich iron-aluminum alloys, J. Phys. Chem. Solids. 6 (1958) 16–37. doi:10.1016/0022-3697(58)90213-0.

[26] H. Clemens, H. Kestler, Processing and Applications of Intermetallic γ-TiAl-Based Alloys, Adv. Eng. Mater. 2 (2000) 551–570. doi:10.1002/1527-2648(200009)2:9<551::AID-ADEM551>3.0.CO;2-U.

[27] N.S. Stoloff, Iron aluminides: present status and future prospects, Mater. Sci. Eng. A. 258 (1998) 1–14. doi:10.1016/S0921-5093(98)00909-5.

[28] D.G. Morris, M.A. Morris, Strengthening at intermediate temperatures in iron aluminides, Mater. Sci. Eng. A. 239-240 (1997) 23–38. doi:10.1016/S0921-5093(97)00557-1.

[29] D.G. Morris, Possibilities for high-temperature strengthening in iron aluminides, Intermetallics. 6 (1998) 753–758. doi:10.1016/S0966-9795(98)00028-4.

[30] A. Bahadur, Enhancement of high temperature strength and room temperature ductility of iron aluminides by alloying, Mater. Sci. Technol. 19 (2003) 1627–1634. doi:10.1179/026708303225008266.

[31] A. Castagna, N.S. Stoloff, Hydrogen embrittlement of Fe3Al alloys, Mater. Sci. Eng. A. 192–193, Part 1 (1995) 399–406. doi:10.1016/0921-5093(94)03240-8.

[32] C.T. Liu, E.H. Lee, C.G. McKamey, An environmental effect as the major cause for room-temperature embrittlement in FeAl, Scr. Metall. 23 (1989) 875–880.

[33] S.C. Deevi, V.K. Sikka, C.T. Liu, Processing, properties, and applications of nickel and iron aluminides, Prog. Mater. Sci. 42 (1997) 177–192.

[34] D.G. Morris, M.A. Muñoz-Morris, Recent Developments Toward the Application of Iron Aluminides in Fossil Fuel Technologies, Adv. Eng. Mater. 13 (2011) 43–47. doi:10.1002/adem.201000210.

[35] C.G. McKamey, V.K. Sikka, G.M. Goodwin, Development of ductile Fe3Al-based aluminides, in: Conf. 7 Annu. Conf. Foss. Energy Mater. Oak Ridge TN U. S. 11-13 May 1993, 1993.

[36] D.G. Morris, M.A. Muñoz-Morris, J. Chao, Development of high strength, high ductility and high creep resistant iron aluminide, Intermetallics. 12 (2004) 821–826. doi:10.1016/j.intermet.2004.02.032.

[37] A. Howard Cottrell, The mechanical properties of matter, Wiley, 1964.

[38] N.S. Stoloff, C.T. Liu, Environmental embrittlement of iron aluminides, Intermetallics. 2 (1994) 75–87. doi:10.1016/0966-9795(94)90001-9.

[39] D.G. Morris, M.A. Morris-Muñoz, The influence of microstructure on the ductility of iron aluminides, Intermetallics. 7 (1999) 1121–1129. doi:10.1016/S0966-9795(99)00038-2.

[40] J. Chao, D.G. Morris, M.A. Muñoz-Morris, J.L. Gonzalez-Carrasco, The influence of some microstructural and test parameters on the tensile behaviour and the ductility of a mechanically-alloyed Fe–40Al alloy, Intermetallics. 9 (2001) 299–308. doi:10.1016/S0966-9795(01)00005-X.

[41] D.G. Morris, S. Gunther, Strength and ductility of Fe-40Al alloy prepared by mechanical alloying, Mater. Sci. Eng. A. 208 (1996) 7–19. doi:10.1016/0921-5093(95)10041-5.

[42] N. Hansen, Hall–Petch relation and boundary strengthening, Scr. Mater. 51 (2004) 801–806. doi:10.1016/j.scriptamat.2004.06.002.

[43] M. Palm, Concepts derived from phase diagram studies for the strengthening of Fe-Al-based alloys, Intermetallics. 13 (2005) 1286–1295. doi:10.1016/j.intermet.2004.10.015.

[44] M. Palm, A. Schneider, F. Stein, G. Sauthoff, Strengthening of iron aluminide alloys for high-temperature applications, in: Mater. Res. Soc. Symp. Proc., 2005: p. 3.

[45] R.L. Fleischer, Solution hardening, Acta Metall. 9 (1961) 996–1000. doi:10.1016/0001-6160(61)90242-5.

[46] R.L. Fleischer, Substitutional solution hardening, Acta Metall. 11 (1963) 203–209. doi:10.1016/0001-6160(63)90213-X.

[47] J.H. Schneibel, E.D. Specht, W.A. Simpson, Solid solution strengthening in ternary B2 iron aluminides containing 3d transition elements, Intermetallics. 4 (1996) 581–583. doi:10.1016/0966-9795(96)00041-6.

[48] E.P. George, I. Baker, A model for the yield strength anomaly of Fe—Al, Philos. Mag. A. 77 (1998) 737–750.

[49] R. Würschum, C. Grupp, H.-E. Schaefer, Simultaneous Study of Vacancy Formation and Migration at High Temperatures in B2-Type Fe Aluminides, Phys. Rev. Lett. 75 (1995) 97. doi:10.1103/PhysRevLett.75.97.

[50] C. Garcia Oca, D.G. Morris, M.A. Muñoz-Morris, The role of carbon and vacancies in the quench hardening and age softening of a Fe-40Al-C alloy, Scr. Mater. 44 (2001) 561–568. doi:10.1016/S1359-6462(00)00637-0.

[51] M.A. Morris, D.G. Morris, Quenching and Ageing Effects on Defects and Their Structures in FeAl Alloys, and the Influence on Hardening and Softening, Scr. Mater. 38 (1998) 509–516. doi:10.1016/S1359-6462(97)00468-5.

[52] K. Yoshimi, S. Hanada, The strength properties of iron aluminides, JOM. 49 (1997) 46–49. doi:10.1007/BF02914403.

[53] J. Wolff, M. Franz, A. Broska, R. Kerl, M. Weinhagen, B. Köhler, et al., Point defects and their properties in FeAl and FeSi alloys, Intermetallics. 7 (1999) 289–300. doi:10.1016/S0966-9795(98)00105-8.

[54] T. Haraguchi, K. Yoshimi, M.H. Yoo, H. Kato, S. Hanada, A. Inoue, Vacancy clustering and relaxation behavior in rapidly solidified B2 FeAl ribbons, Acta Mater. 53 (2005) 3751–3764. doi:10.1016/j.actamat.2005.04.027.

[55] M. Kogachi, T. Haraguchi, Quenched-in vacancies in B2-structured intermetallic compound FeAl, Mater. Sci. Eng. A. 230 (1997) 124–131. doi:10.1016/S0921-5093(97)00016-6.

[56] Y.A. Chang, L.M. Pike, C.T. Liu, A.R. Bilbrey, D.S. Stone, Correlation of the hardness and vacancy concentration in FeAl, Intermetallics. 1 (1993) 107–115. doi:10.1016/0966-9795(93)90028-T.

[57] C.H. Kong, P.R. Munroe, The effect of ternary additions on the vacancy hardening of FeAl, Scr. Metall. Mater. 30 (1994) 1079–1083. doi:10.1016/0956-716X(94)90559-2.

[58] C.G. McKamey, J.A. Horton, C.T. Liu, Effect of chromium on properties of Fe3Al, J Mater Res. 4 (1989) 1157.

[59] O. Klein, I. Baker, Effect of chromium on the environmental sensitivity of FeAl at room temperature, Scr. Metall. Mater. 27 (1992) 1823–1828. doi:10.1016/0956-716X(92)90027-C.

[60] C.G. McKamey, C.T. Liu, Chromium addition and environmental embrittlement in Fe3Al, Scr. Met. 24 (1990) 2119–2122.

[61] D.G. Morris, M.M. Dadras, M.A. Morris, The influence of Cr addition on the ordered microstructure and deformation and fracture behaviour of a Fe-28%Al intermetallic, Acta Metall. Mater. 41 (1993) 97–111. doi:10.1016/0956-7151(93)90342-P.

[62] R.S. Sundar, T.R.G. Kutty, D.H. Sastry, Hot hardness and creep of Fe3Al-based alloys, Intermetallics. 8 (2000) 427–437. doi:10.1016/S0966-9795(99)00118-1.

[63] P.R. Munroe, I. Baker, Room temperature deformation modes in DO3-structured Fe-34Al and Fe-28Al-6Cr, J. Mater. Sci. 28 (1993) 2299–2303. doi:10.1007/BF01151656.

[64] S.M. Kim, D.G. Morris, Long range order and vacancy properties in Al-rich Fe3Al and Fe3Al(Cr) alloys, Acta Mater. 46 (1998) 2587–2602. doi:10.1016/S1359-6454(97)00464-3.

[65] G. Hasemann, J.H. Schneibel, E.P. George, Dependence of the yield stress of Fe3Al on heat treatment, Intermetallics. 21 (2012) 56–61. doi:10.1016/j.intermet.2011.09.005.

[66] P.R. Munroe, I. Baker, Microstructure and mechanical properties of Fe-40Al+Cr alloys, Scr. Metall. Mater. 24 (1990) 2273–2278. doi:10.1016/0956-716X(90)90078-U.

[67] L.O.U. Baiyang, X.B. Zhang, L.I.U. Maosen, Z. Zhang, Effects of Mn on fracture behaviour of DO3 Fe3Al-based intermetallic alloy, J. Mater. Sci. 33 (1998) 1481–1486. doi:10.1023/A:1004347709024.

[68] D.G. Morris, M.A. Muñoz-Morris, C. Baudin, The high-temperature strength of some Fe3Al alloys, Acta Mater. 52 (2004) 2827–2836. doi:10.1016/j.actamat.2004.02.031.

[69] M. Palm, G. Sauthoff, Deformation behaviour and oxidation resistance of single-phase and two-phase L21-ordered Fe-Al-Ti alloys, Intermetallics. 12 (2004) 1345–1359. doi:10.1016/j.intermet.2004.03.017.

[70] R.T. Fortnum, D.E. Mikkola, Effects of molybdenum, titanium and silicon additions on the Do3 ⇄ B2 transition temperature for alloys near Fe3Al, Mater. Sci. Eng. 91 (1987) 223–231. doi:10.1016/0025-5416(87)90301-6.

[71] F. Stein, A. Schneider, G. Frommeyer, Flow stress anomaly and order–disorder transitions in Fe3Al-based Fe–Al–Ti–X alloys with X=V, Cr, Nb, or Mo, Intermetallics. 11 (2003) 71–82. doi:10.1016/S0966-9795(02)00187-5.

[72] P. Villars, L.D. Calvert, Pearson's Handbook of Crystallographic Data for Intermetallic Phases, 2nd ed., ASM International, 1991.

[73] W.B. Pearson, The crystal chemistry and physics of metals and alloys, Wiley-Interscience, 1972.

[74] I. Ohnuma, C.G. Schön, R. Kainuma, G. Inden, K. Ishida, Ordering and phase separation in the b.c.c. phase of the Fe-Al-Ti system, Acta Mater. 46 (1998) 2083–2094. doi:10.1016/S1359-6454(97)00376-5.

[75] U. Prakash, G. Sauthoff, Structure and properties of Fe–Al–Ti intermetallic alloys, Intermetallics. 9 (2001) 107–112. doi:10.1016/S0966-9795(00)00101-1.

[76] R. Krein, M. Palm, M. Heilmaier, Characterization of microstructures, mechanical properties, and oxidation behavior of coherent A2+ L21 Fe-Al-Ti, J. Mater. Res. 24 (2009) 3412–3421.

[77] R. Diehm, D. Mikkola, Composition and Temperature-Dependent Deformation-Behavior of Iron Aluminides Alloyed with Mo and or Ti, J. Met. 39 (1987) A55–A55.

[78] A. Gorzel, M. Palm, G. Sauthoff, Constitution-based alloy selection for the screening of intermetallic Ti-Al-Fe alloys, Z. Met. 90 (1999) 64–70.

[79] S.M. Zhu, K. Sakamoto, M. Tamura, K. Iwasaki, A comparative study of the high temperature deformation behavior of Fe-25Al and Fe-25Al-10Ti alloys, Scr. Mater. 42 (2000) 905–910. doi:10.1016/S1359-6462(00)00312-2.

[80] S.M. Zhu, K. Sakamoto, M. Tamura, K. Iwasaki, Effects of titanium addition on the microstructure and mechanical behavior of iron aluminide Fe3Al, Mater. Trans. 42 (2001) 484–490. doi:10.2320/matertrans.42.484.

[81] F. Dobeš, P. Kratochvíl, K. Milička, Creep of cast Fe–36Al–2Ti alloy, Intermetallics. 14 (2006) 1199–1203. doi:10.1016/j.intermet.2005.11.017.

[82] R. Krein, M. Palm, The influence of Cr and B additions on the mechanical properties and oxidation behaviour of L21-ordered Fe–Al–Ti-based alloys at high temperatures, Acta Mater. 56 (2008) 2400–2405. doi:10.1016/j.actamat.2008.01.053.

[83] D. Li, D. Lin (T.L. Lin), Microstructure evolution and activation energy during superplastic deformation of FeAl based intermetallics, Scr. Mater. 36 (1997) 1289–1294. doi:10.1016/S1359-6462(97)00021-3.

[84] O. Prymak, F. Stein, Solidification and high-temperature phase equilibria in the Fe-Al-rich part of the Fe-Al-Nb system, Intermetallics. 18 (2010) 1322–1326. doi:10.1016/j.intermet.2009.12.022.

[85] D.G. Morris, S. Gunther, Order-disorder changes in Fe3Al based alloys and the development of an iron-base α-α″ superalloy, Acta Mater. 44 (1996) 2847–2859. doi:10.1016/1359-6454(95)00382-7.

[86] D.G. Morris, S. Gunther, Room and high temperature mechanical behaviour of a Fe3Al-based alloy with α-α″ microstructure, Acta Mater. 45 (1997) 811–822. doi:10.1016/S1359-6454(96)00178-4.

[87] F. Stein, M. Palm, G. Sauthoff, Mechanical properties and oxidation behaviour of two-phase iron aluminium alloys with Zr(Fe,Al)2 Laves phase or Zr(Fe,Al)12 [tau]1 phase, Intermetallics. 13 (2005) 1275–1285. doi:10.1016/j.intermet.2004.08.013.

[88] A. Schneider, G. Sauthoff, Iron aluminium alloys with strengthening carbides and intermetallic phases for high-temperature applications, Steel Res. Int. 75 (2004) 55–61.

[89] C. Stallybrass, A. Schneider, G. Sauthoff, The strengthening effect of (Ni,Fe)Al precipitates on the mechanical properties at high temperatures of ferritic Fe–Al–Ni–Cr alloys, Intermetallics. 13 (2005) 1263–1268. doi:10.1016/j.intermet.2004.07.048.

[90] C. Stallybrass, G. Sauthoff, Ferritic Fe–Al–Ni–Cr alloys with coherent precipitates for high-temperature applications, Mater. Sci. Eng. A. 387–389 (2004) 985–990. doi:10.1016/j.msea.2004.01.108.

[91] A. Kellou, J.M. Raulot, T. Grosdidier, Structural and thermal properties of Fe3Al, Fe3AlC and hypothetical Fe3AlX (X = H, B, N, O) compounds: Ab initio and quasi-harmonic Debye modelling, Intermetallics. 18 (2010) 1293–1296. doi:10.1016/j.intermet.2010.02.013.

[92] W.F. Gale, T.C. Totemeier, Smithells Metals Reference Book, Butterworth-Heinemann, 2003.

[93] F. Dobeš, P. Kratochvíl, V. Vodičková, The effect of carbon and silicon additions on the creep properties of Fe-40 at. % Al type alloys at elevated temperatures, Intermetallics. 19 (2011) 1526–1532. doi:10.1016/j.intermet.2011.05.024.

[94] A. Schneider, L. Falat, G. Sauthoff, G. Frommeyer, Microstructures and mechanical properties of Fe3Al-based Fe–Al–C alloys, Intermetallics. 13 (2005) 1322–1331. doi:10.1016/j.intermet.2005.01.013.

[95] A. Schneider, L. Falat, G. Sauthoff, G. Frommeyer, Constitution and microstructures of Fe–Al–M–C (M=Ti, V, Nb, Ta) alloys with carbides and Laves phase, Intermetallics. 11 (2003) 443–450. doi:10.1016/S0966-9795(03)00018-9.

[96] L. Falat, A. Schneider, G. Sauthoff, G. Frommeyer, Mechanical properties of Fe–Al–M–C (M=Ti, V, Nb, Ta) alloys with strengthening carbides and Laves phase, Intermetallics. 13 (2005) 1256–1262. doi:10.1016/j.intermet.2004.05.010.

[97] D.G. Morris, M.A. Muñoz-Morris, I. Gutierrez-Urrutia, L.M. Requejo, Precipitation in ductile Fe–18Al–5Cr alloys with additions of Mo, W and C and effects on high-temperature strength, Intermetallics. 17 (2009) 404–413. doi:10.1016/j.intermet.2008.11.015.

[98] S. Kobayashi, A. Schneider, S. Zaefferer, G. Frommeyer, D. Raabe, Phase equilibria among [alpha]-Fe(Al, Cr, Ti), liquid and TiC and the formation of TiC in Fe3Al-based alloys, Acta Mater. 53 (2005) 3961–3970. doi:10.1016/j.actamat.2005.04.044.

[99] S. Kobayashi, S. Zaefferer, Creation of a fine-grained and deformed structure with fine carbide particles in a Fe3Al–Cr–Mo–C alloy, Intermetallics. 14 (2006) 1252–1256. doi:10.1016/j.intermet.2005.11.034.

[100] S. Kobayashi, S. Zaefferer, A. Schneider, D. Raabe, G. Frommeyer, Optimisation of precipitation for controlling recrystallisation of wrought Fe3Al based alloys, Intermetallics. 13 (2005) 1296–1303. doi:10.1016/j.intermet.2004.10.016.

[101] V.S. Rao, Fe3Al-Fe3AlC intermetallics for high temperature applications: An assessment, J. Mater. Sci. 39 (2004) 4193–4198.

[102] A. Radhakrishna, R.G. Baligidad, D.S. Sarma, Effect of carbon on structure and properties of FeAl based intermetallic alloy, Scr. Mater. 45 (2001) 1077–1082. doi:10.1016/S1359-6462(01)01142-3.

[103] V.K. Sikka, D. Wilkening, J. Liebetrau, B. Mackey, Melting and casting of FeAl-based cast alloy, Mater. Sci. Eng. A. 258 (1998) 229–235. doi:10.1016/S0921-5093(98)00938-1.

[104] D.M. Dimiduk, M.G. Mendiratta, D. Banerjee, H.A. Lipsitt, A structural study of ordered precipitates in an ordered matrix within the Fe-Al-Nb system, Acta Metall. 36 (1988) 2947–2958. doi:10.1016/0001-6160(88)90177-0.

[105] F. Stein, G. Sauthoff, M. Palm, Phases and phase equilibria in the Fe-Al-Zr system, Z. Fuer Met. 95 (2004) 469–485.

[106] J.W. Cohron, Y. Lin, R.H. Zee, E.P. George, Room-temperature mechanical behavior of FeAl: effects of stoichiometry, environment, and boron addition, Acta Mater. 46 (1998) 6245–6256. doi:16/S1359-6454(98)00254-7.

[107] D.G. Morris, M.A. Muñoz-Morris, L.M. Requejo, Work hardening in Fe-Al alloys, Mater. Sci. Eng. A. 460-461 (2007) 163–173. doi:10.1016/j.msea.2007.01.014.

[108] L. Pang, K.S. Kumar, On the impact toughness of Fe-40Al-based B2 aluminides, Intermetallics. 8 (2000) 157–163. doi:16/S0966-9795(99)00083-7.

[109] R. Krein, A. Schneider, G. Sauthoff, G. Frommeyer, Microstructure and mechanical properties of Fe3Al-based alloys with strengthening boride precipitates, Intermetallics. 15 (2007) 1172–1182. doi:10.1016/j.intermet.2007.02.005.

[110] S. Hasse, E. Brunhuber, Giesserei Lexikon, Fachverlag Schiele & Schoen, 2001.

[111] H.E. Exner, H.P. Hougardy, Einführung in die quantitative Gefügeanalyse, DGM-Informationsges. Verlag, 1986.

[112] J.W. Edington, Practical electron microscopy in materials science, Van Nostrand Reinhold Co., 1976.

[113] J. Herrmann, Thesis, RWTH Aachen, 2000.

[114] R. Bürgel, H.J. Maier, T. Niendorf, Hochtemperaturkorrosion, in: Handb. Hochtemp.-Werkst., Vieweg+Teubner, 2011: pp. 260–339. http://link.springer.com/chapter/10.1007/978-3-8348-9907-1_5 (accessed July 22, 2013).

[115] G.Y. Lai, High-Temperature Corrosion and Materials Applications, ASM International, 2007.

[116] C.E. Mortimer, U. Müller, Chemie: das Basiswissen der Chemie ; 126 Tabellen, Georg Thieme Verlag, 2007.

[117] A.S. Khanna, Introduction to High Temperature Oxidation and Corrosion, ASM International, 2002.

[118] C. Wagner, Z Phys Chem. 21 (1933) 25.

[119] N. Birks, G.H. Meier, F.S. Pettit, Introduction to the High Temperature Oxidation of Metals, Cambridge University Press, 2006.

[120] C. Xu, W. Gao, Pilling-Bedworth ratio for oxidation of alloys, Mater. Res. Innov. 3 (2000) 231–235. doi:10.1007/s100190050008.

[121] J.P.S. Pringle, The anodic oxidation of superimposed niobium and tantalum layers: theory, Electrochimica Acta. 25 (1980) 1403–1421. doi:10.1016/0013-4686(80)87156-8.

[122] J.H. DeVan, P.F. Tortorelli, The oxidation-sulfidation behavior of iron alloys containing 16-40 AT% aluminum, Corros. Sci. 35 (1993) 1065–1071. doi:10.1016/0010-938X(93)90325-B.

[123] J.L. Smialek, J. Doychak, D.J. Gaydosh, Oxidation behavior of FeAl+Hf, Zr, B, Oxid. Met. 34 (1990) 259–275. doi:10.1007/BF00665018.

[124] H.J. Grabke, Oxidation of NiAl and FeAl, Intermetallics. 7 (1999) 1153–1158. doi:10.1016/S0966-9795(99)00037-0.

[125] C.H. Xu, W. Gao, H. Gong, Oxidation behaviour of FeAl intermetallics.The effects of Y and/or Zr on isothermal oxidation kinetics, Intermetallics. 8 (2000) 769–779. doi:16/S0966-9795(00)00007-8.

[126] R. Prescott, M.J. Graham, The oxidation of iron-aluminum alloys, Oxid. Met. 38 (1992) 73–87. doi:10.1007/BF00665045.

[127] N. Ziegler, Trans AIME. (1932) 267.

[128] C. Sykes, J. W. Bampfylde, J Iron Steel Inst. (1934) 389–410.

[129] P. Tomaszewicz, G.R. Wallwork, Observations of nodule growth during the oxidation of pure binary iron-aluminum alloys, Oxid. Met. 19 (1983) 165–185. doi:10.1007/BF00666643.

[130] R. Prescott, M.J. Graham, The formation of aluminum oxide scales on high-temperature alloys, Oxid. Met. 38 (1992) 233–254. doi:10.1007/BF00666913.

[131] J.W. Newsome, H.W. Heiser, A.S. Russell, H.C. Stumpf, Alumina Properties, Aloca Alum. Co Am Res. Lab Tech Oaoer No 10 Second Revis. (1960) 88 pp.

[132] H. Saalfeld, Einkristalluntersuchungen zum Problem der Hydrargillit-Entwässerung, Z. Für Krist. 112 (1959) 88–96. doi:10.1524/zkri.1959.112.1-6.88.

[133] K. Natesan, Corrosion performance of iron aluminides in mixed-oxidant environments, Mater. Sci. Eng. A. 258 (1998) 126–134. doi:10.1016/S0921-5093(98)00925-3.

[134] A. Mignone, S. Frangini, A.L. Barbera, O. Tassa, High temperature corrosion of b2 iron aluminides, Corros. Sci. 40 (1998) 1331–1347. doi:10.1016/S0010-938X(98)00014-6.

[135] W. Hagel, Oxidation of Iron Nickel and Cobalt-Base Alloys Containing Aluminum, Corrosion. 21 (1965) 316–&.

[136] I. Rommerskirchen, B. Eltester, H.J. Grabke, Oxidation of β-FeAl and Fe-Al alloys, Mater. Corros. Korros. 47 (1996) 646–649. doi:10.1002/maco.19960471109.

[137] Y. Kitajima, S. Hayashi, T. Nishimoto, T. Narita, S. Ukai, Rapid Formation of alpha-Al2O3 Scale on an Fe-Al Alloy by Pure-Metal Coatings at 900 A degrees C, Oxid. Met. 73 (2010) 375–388. doi:10.1007/s11085-009-9184-8.

[138] S. Chevalier, P. Juzon, G. Borchardt, A. Galerie, K. Przybylski, J.P. Larpin, High-Temperature Oxidation of Fe3Al and Fe3Al–Zr Intermetallics, Oxid. Met. 73 (2009) 43–64. doi:10.1007/s11085-009-9168-8.

[139] K. Wambach, J. Peters, H.J. Grabke, Behaviour of Al2O3 scales on Fe-Al and Fe-Ni-Al alloys with small additions of titanium, zirconium, niobium and vanadium on thermal cycling and creep in oxidizing and carburizing atmospheres, Mater. Sci. Eng. 88 (1987) 205–212. doi:10.1016/0025-5416(87)90086-3.

[140] E.P. George, I. Baker, Thermal vacancies and the yield anomaly of FeAl, Intermetallics. 6 (1998) 759–763. doi:10.1016/S0966-9795(98)00063-6.

[141] D. Janda, M. Heilmaier, K. von Klinski Wetzel, K.S. Kumar, Effect of strain-rate on the deformation response of D03 and B2 ordered iron aluminides, (in preparation).

[142] H.J. Grabke, Oxidation of aluminides, in: Mater. Sci. Forum, 1997: pp. 149–162.

[143] P.F. Tortorelli, K. Natesan, Critical factors affecting the high-temperature corrosion performance of iron aluminides, Mater. Sci. Eng. A. 258 (1998) 115–125. doi:10.1016/S0921-5093(98)00924-1.

[144] F. Lang, Z. Yu, S. Gedevanishvili, S.C. Deevi, T. Narita, Isothermal oxidation behavior of a sheet alloy of Fe–40at.%Al at temperatures between 1073 and 1473 K, Intermetallics. 11 (2003) 697–705. doi:10.1016/S0966-9795(03)00067-0.

[145] J. Doychak, J. Smialek, T. Mitchell, Transient oxidation of Single-Crystal β-NiAl, Metall. Mater. Trans. A. 20 (1989) 499–518. doi:10.1007/BF02653930.

[146] G.C. Rybicki, J.L. Smialek, Effect of the θ-α-Al2O3 transformation on the oxidation behavior of β-NiAl + Zr, Oxid. Met. 31 (1989) 275–304. doi:10.1007/BF00846690.

[147] K. Hirota, W. Komatsu, Concurrent Measurement of Volume, Grain-Boundary, and Surface Diffusion Coefficients in the System NiO-Al2O3, J. Am. Ceram. Soc. 60 (1977) 105–107. doi:10.1111/j.1151-2916.1977.tb15481.x.

[148] M.A. Montealegre, J.L. González-Carrasco, M.A. Muñoz-Morris, Oxidation behaviour of Fe40Al alloy strip, Intermetallics. 9 (2001) 487–492. doi:10.1016/S0966-9795(01)00028-0.

[149] E.F. Bertaut, L. Corliss, F. Forrat, R. Aleonard, R. Pauthenet, Etude de niobates et tantalates de metaux de transition bivalents, J. Phys. Chem. Solids. 21 (1961) 234–251. doi:10.1016/0022-3697(61)90103-2.

[150] J.P. Lin, L.L. Zhao, G.Y. Li, L.Q. Zhang, X.P. Song, F. Ye, et al., Effect of Nb on oxidation behavior of high Nb containing TiAl alloys, Intermetallics. 19 (2011) 131–136. doi:10.1016/j.intermet.2010.08.029.

[151] H. Jiang, M. Hirohasi, Y. Lu, H. Imanari, Effect of Nb on the high temperature oxidation of Ti-(0-50 at.%)Al, Scr. Mater. 46 (2002) 639–643. doi:10.1016/S1359-6462(02)00042-8.

[152] B.A. Pint, J.R. Martin, L.W. Hobbs, 18O/SIMS characterization of the growth mechanism of doped and undoped α-Al2O3, Oxid. Met. 39 (1993) 167–195. doi:10.1007/BF00665610.

[153] M. Martinez, B. Viguier, P. Maugis, J. Lacaze, Relation between composition, microstructure and oxidation in iron aluminides, Intermetallics. 14 (2006) 1214–1220. doi:10.1016/j.intermet.2005.11.018.

[154] D. Hull, D.J. Bacon, Introduction to Dislocations, Butterworth-Heinemann, Oxford, 2011.

[155] G. Gottstein, Physikalische Grundlagen der Materialkunde, Springer Berlin Heidelberg, 2007. http://link.springer.com/chapter/10.1007/978-3-540-71105-6_6 (accessed July 1, 2014).

[156] A. Lawley, J.A. Coll, R.W. Cahn, Influence of Crystallographic Order on Creep of Iron-Aluminum Solid Solutions, Trans. Metall. Soc. AIME. 218 (1960) 166–176.

[157] A. Lawley, E.A. Vidoz, R.W. Cahn, The dependence of the flow stress of Fe3Al on crystallographic order, Acta Metall. 9 (1961) 287–296. doi:10.1016/0001-6160(61)90221-8.

[158] R.W. Cahn, J.A. Coll, Twinning in iron-aluminium alloys, Acta Metall. 9 (1961) 138–148. doi:10.1016/0001-6160(61)90058-X.

[159] Y. Yang, I. Baker, G.. Gray III, C. Cady, The yield stress anomaly in stoichiometric FeAl at high strain rate, Scr. Mater. 40 (1999) 403–408. doi:10.1016/S1359-6462(98)00448-5.

[160] R.T. Gray, Influence of high-strain rate and temperature on the mechanical behavior of Nl-, Fe-, and Ti- based aluminides, in: Deform. Fract. Ordered Intermet. Mater. III, TMS, 1997: pp. 57–73.

[161] R. Carleton, E.P. George, R.H. Zee, Effects of deviations from stoichiometry on the strength anomaly and fracture behavior of B-doped FeAl, Intermetallics. 3 (1995) 433–441. doi:10.1016/0966-9795(94)00041-I.

[162] K.T. Ramesh, Springer Handbook of Experimental Solid Mechanics, Vol. 33 High Strain Rate and Impact Experiments, 2008. http://www.springer.com/materials/mechanics/book/978-0-387-26883-5 (accessed December 17, 2013).

[163] J. Herrmann, G. Inden, G. Sauthoff, Deformation behaviour of iron-rich iron-aluminum alloys at low temperatures, Acta Mater. 51 (2003) 2847–2857. doi:10.1016/S1359-6454(03)00089-2.

[164] P. Ludwik, Elemente der technologischen Mechanik, Springer, 1909.

[165] H.J. Leamy, F.X. Kayser, The Compressive Deformation Behavior of Long Range Ordered Polycrystalline iron—aluminum Alloys, Phys. Status Solidi B. 34 (1969) 765–780. doi:10.1002/pssb.19690340240.

[166] D. Wu, I. Baker, The effect of environment and strain rate on the room temperature tensile properties of FeAl single crystals, Intermetallics. 9 (2001) 57–65. doi:16/S0966-9795(00)00097-2.

[167] I. Baker, H. Xiao, O. Klein, C. Nelson, J.D. Whittenberger, The effect of temperature and Fe: Al ratio on the flow and fracture of FeAl, Acta Metall. Mater. 43 (1995) 1723–1730. doi:10.1016/0956-7151(94)00369-S.

[168] D. Wu, I. Baker, P.R. Munroe, E.P. George, The yield strength anomaly of single-slip-oriented Fe-Al single crystals, Intermetallics. 15 (2007) 103–107. doi:10.1016/j.intermet.2006.03.007.

[169] W.F. Hosford, Mechanical Behavior of Materials, 2nd ed., Cambridge University Press, Cambridge, 2009. http://ebooks.cambridge.org/ref/id/CBO9780511810923 (accessed June 15, 2013).

[170] L.E. Murr, K.P. Staudhammer, M.A. Meyers, Metallurgical Applications of Shock-Wave and High-Strain Rate Phenomena, CRC Press, 1986.

[171] M. Kass, C.R. Brooks, D. Falcon, D. Basak, The formation of defects in Fe–Al alloys: electrical resistivity and specific heat measurements, Intermetallics. 10 (2002) 951–966. doi:10.1016/S0966-9795(02)00115-2.

[172] C. Efstathiou, H. Sehitoglu, Strain hardening and heterogeneous deformation during twinning in Hadfield steel, Acta Mater. 58 (2010) 1479–1488. doi:10.1016/j.actamat.2009.10.054.

[173] F.J. Humphreys, Y. Huang, I. Brough, C. Harris, Electron backscatter diffraction of grain and subgrain structures — resolution considerations, J. Microsc. 195 (1999) 212–216. doi:10.1046/j.1365-2818.1999.00579.x.

[174] H.J. Leamy, E.D. Gibson, F.X. Kayser, The elastic stiffness coefficients of iron-aluminum alloys—I experimental results and thermodynamic analysis, Acta Metall. 15 (1967) 1827–1838. doi:10.1016/0001-6160(67)90047-8.

[175] D.G. Morris, S. Gunther, Influence of strain rate on yield stress and stress anomaly in an alloy based on Fe3Al, Mater. Sci. Eng. A. 211 (1996) 23–32. doi:10.1016/0921-5093(96)10180-5.

[176] D.G. Morris, D. Peguiron, M. Nazmy, Yield stress and stress anomaly in an Fe3Al alloy, Philos. Mag. A. 71 (1995) 441–463.

[177] S. Shim, H. Bei, M.K. Miller, G.M. Pharr, E.P. George, Effects of focused ion beam milling on the compressive behavior of directionally solidified micropillars and the nanoindentation response of an electropolished surface, Acta Mater. 57 (2009) 503–510. doi:10.1016/j.actamat.2008.09.033.

[178] M.J. Marcinkowski, R.M. Fisher, Theoretical Analysis of Plastic Deformation in Superlattices Based on the Body-Centered Cubic Structure, J. Appl. Phys. 34 (1963) 2135–2145. doi:doi:10.1063/1.1702703.

[179] J.Y. Guedou, J. Rieu, Twinning and pseudoelasticity in single crystal Fe-Al alloys, Scr. Metall. 12 (1978) 927–930. doi:10.1016/0036-9748(78)90183-7.

[180] K.T. Park, E. Goo, Deformation twinning in D03-ordered Fe3Al alloys, Acta Metall. Mater. 39 (1991) 3027–3035. doi:10.1016/0956-7151(91)90035-Y.

[181] J.W. Christian, D.E. Laughlin, Twinning in derivative structures of BCC and FCC, Scr. Metall. 21 (1987) 1131–1135. doi:10.1016/0036-9748(87)90264-X.

[182] J.W. Christian, D.E. Laughlin, Overview no. 67 The deformation twinning of superlattice structures derived from disordered B.C.C. or F.C.C. solid solutions, Acta Metall. 36 (1988) 1617–1642. doi:10.1016/0001-6160(88)90230-1.

[183] M. Bevis, A.G. Crocker, Twinning Modes in Lattices, Proc. R. Soc. Lond. Math. Phys. Sci. 313 (1969) 509 –529. doi:10.1098/rspa.1969.0208.

[184] H.Y. Yasuda, T. Kishimoto, Y. Umakoshi, Temperature Dependence of Twinning Pseudoelasticity in Fe3Ga Single Crystals, Mater. Trans. 51 (2010) 2196–2200.

[185] F. Laves, What is a twin and what is a “twin”?, Acta Metall. 14 (1966) 58. doi:10.1016/0001-6160(66)90273-2.

[186] W. Blum, P. Eisenlohr, F. Breutinger, Understanding creep—a review, Metall. Mater. Trans. A. 33 (2002) 291–303. doi:10.1007/s11661-002-0090-9.

[187] B. Ilschner, Hochtemperatur-Plastizität: Warmfestigkeit u. Warmverformbarkeit metall. u. nichtmetall. Werkstoffe, Springer, 1973.

[188] E.N. da C. Andrade, On the Viscous Flow in Metals, and Allied Phenomena, Proc R Soc A. 84 (1910) 1–12.

[189] E.N. da C. Andrade, The flow in metals under large constant stresses, Proc R Soc A. 90 (1914) 329.

[190] Mechanische Eigenschaften, in: Phys. Grundlagen Mater., Springer Berlin Heidelberg, 2007: pp. 197–301. http://link.springer.com/chapter/10.1007/978-3-540-71105-6_6 (accessed May 12, 2014).

[191] A. Fuchs, B. Ilschner, An Analysis of Creep Behaviour of Iron-Molybdenum Solid Solutions, Acta Metall. 17 (1969) 701–&. doi:10.1016/0001-6160(69)90076-5.

[192] R.R. Vandervoort, W. Barmore, High-Temperature Plastic Deformation of Polycrystalline Rhenium, Trans. Metall. Soc. Aime. 245 (1969) 825–&.

[193] R.R. Vandervoort, Creep Behavior of W-5-Re, Metall. Trans. 1 (1970) 857–&.

[194] J. Rösler, H. Harders, M. Bäker, Mechanisches Verhalten Der Werkstoffe, Springer DE, 2008.

[195] J.-P. Poirier, Creep of Crystals: High-Temperature Deformation Processes in Metals, Ceramics and Minerals, Cambridge University Press, 1985.

[196] J.D. Whittenberger, R.V. Krishnan, A simple application of the Bailey-Orowan creep model to Fe-39.8 at % AI and γ/γ′-α, J. Mater. Sci. 19 (1984) 509–517. doi:10.1007/BF00553575.

[197] F.R.N. Nabarro, F. de Villiers, Physics Of Creep And Creep-Resistant Alloys, CRC Press, 1995.

[198] R. Bürgel, Handbuch Hochtemperatur-Werkstofftechnik, Vieweg, Wiesbaden, 2006.

[199] Mukherje.ak, J. Bird, J. Dorn, Experimental Correlations for High-Temperature Creep, Asm Trans. Q. 62 (1969) 155–&.

[200] P. Yavari, T. Langdon, An Examination of the Breakdown in Creep by Viscous Glide in Solid-Solution Alloys at High Stress Levels, Acta Metall. 30 (1982) 2181–2196. doi:10.1016/0001-6160(82)90139-0.

[201] S. Straub, W. Blum, Does the “natural” third power law of steady state creep hold for pure aluminium?, Scr. Metall. Mater. 24 (1990) 1837–1842. doi:10.1016/0956-716X(90)90036-G.

[202] O.D. Sherby, P.M. Burke, Mechanical behavior of crystalline solids at elevated temperature, Prog. Mater. Sci. 13 (1968) 323–390. doi:10.1016/0079-6425(68)90024-8.

[203] J. Weertman, Dislocation Climb Theory of Steady-State Creep, Asm Trans. Q. 61 (1968) 681–&.

[204] M. Biberger, W. Blum, On the natural law of steady state creep, Scr. Metall. 23 (1989) 1419–1424. doi:10.1016/0036-9748(89)90070-7.

[205] C. g. McKamey, P. j. Maziasz, J. w. Jones, Effect of addition of molybdenum or niobium on creep-rupture properties of Fe3Al, J. Mater. Res. 7 (1992) 2089–2106. doi:10.1557/JMR.1992.2089.

[206] J.D. Whittenberger, Influence of thermomechanical processing on elevated temperature slow plastic flow properties of B2 aluminide Fe-39.8at.%Al, Mater. Sci. Eng. 57 (1983) 77–85. doi:16/0025-5416(83)90029-0.

[207] J.A. Jimenez, G. Frommeyer, Creep behavior of intermetallic FeAl and FeAlCr alloys, Mater. Sci. Eng. A. 220 (1996) 93–99. doi:10.1016/S0921-5093(96)10480-9.

[208] R. Davies, Steady State Creep in Iron - 15 to 20 at. Pct Aluminum Alloys, Trans. Metall. Soc. Aime. 227 (1963) 22–&.

[209] S.C. Deevi, V.K. Sikka, Nickel and iron aluminides: an overview on properties, processing, and applications, Intermetallics. 4 (1996) 357–375. doi:10.1016/0966-9795(95)00056-9.

[210] D.G. Morris, M. Nazmy, C. Noseda, Creep resistance in a new alloy based on Fe3Al, Scr. Metall. Mater. 31 (1994) 173–178. doi:10.1016/0956-716X(94)90170-8.

[211] F. Dobeš, P. Kratochvíl, K. Milička, Compressive creep of Fe3Al-type iron aluminide with Zr additions, Strength Mater. 40 (2008) 106–109. doi:10.1007/s11223-008-0028-6.

[212] R. Krein, M. Palm, Two-fold flow stress anomaly in L21-ordered Fe-Al-Ti-based alloys, Mater. Sci. Eng. A. 460-461 (2007) 174–179. doi:10.1016/j.msea.2007.01.020.

[213] R. Krein, M. Palm, The influence of Cr and B additions on the mechanical properties and oxidation behaviour of L21-ordered Fe-Al-Ti-based alloys at high temperatures, Acta Mater. 56 (2008) 2400–2405. doi:10.1016/j.actamat.2008.01.053.

[214] M.G. Mendiratta, S.K. Ehlers, H.A. Lipsitt, D03-B2-α phase relations in Fe-Al-Ti alloys, Metall. Trans. A. 18 (1987) 509–518. doi:10.1007/BF02649468.

[215] S. Milenkovic, M. Palm, Microstructure and mechanical properties of directionally solidified Fe–Al–Nb eutectic, Intermetallics. 16 (2008) 1212–1218. doi:10.1016/j.intermet.2008.07.007.

[216] M.A. Muñoz-Morris, C. Garcia Oca, D.G. Morris, Microstructure and room temperature strength of Fe-40Al containing nanocrystalline oxide particles, Acta Mater. 51 (2003) 5187–5197. doi:10.1016/S1359-6454(03)00382-3.

[217] M.A. Morris, D.G. Morris, Dispersoid additions and their effect on high temperature deformation of Fe-Al, Acta Metall. Mater. 38 (1990) 551–559. doi:10.1016/0956-7151(90)90209-Y.

[218] M.E. Kassner, M.-T. Perez-Prado, Fundamentals of Creep in Metals and Alloys, Elsevier Science Ltd, 2004.

[219] P. Yavari, F.A. Mohamed, T.G. Langdon, Creep and substructure formation in an Al-5% Mg solid solution alloy, Acta Metall. 29 (1981) 1495–1507. doi:10.1016/0001-6160(81)90184-X.

[220] M. Mills, J. Gibeling, W. Nix, A Dislocation Loop Model for Creep of Solid-Solutions Based on the Steady-State and Transient Creep-Properties of a1-5.5 at Percent-Mg, Acta Metall. 33 (1985) 1503–1514. doi:10.1016/0001-6160(85)90051-3.

[221] R. Horiuchi, M. Otsuka, Mechanism of High-Temperature Creep of Aluminum-Magnesium Solid-Solution Alloys, Trans. Jpn. Inst. Met. 13 (1972) 284–&.

[222] O. Sherby, R. Anderson, J. Dorn, Effect of Alloying Elements on the Elevated Temperature Plastic Properties of Alpha Solid Solutions of Aluminum, Trans. Am. Inst. Min. Metall. Eng. 191 (1951) 643–652.

[223] W. Blum, Creep of crystalline materials: experimental basis, mechanisms and models, Mater. Sci. Eng. A. 319–321 (2001) 8–15. doi:10.1016/S0921-5093(00)02010-4.

[224] A. Cottrell, M. Jaswon, Distribution of Solute Atoms Round a Slow Dislocation, Proc. R. Soc. Lond. Ser. -Math. Phys. Sci. 199 (1949) 104–114. doi:10.1098/rspa.1949.0128.

[225] F. Mohamed, T. Langdon, Transition from Dislocation Climb to Viscous Glide in Creep of Solid-Solution Alloys, Acta Metall. 22 (1974) 779–788. doi:10.1016/0001-6160(74)90088-1.

[226] Y. Umakoshi, M. Yamaguchi, Deformation of FeAl single crystals at high temperatures, Philos. Mag. A. 41 (1980) 573–588.

[227] G. Sharma, R.V. Ramanujan, T.R.G. Kutty, G.P. Tiwari, Hot hardness and indentation creep studies of a Fe-28Al-3Cr-0.2C alloy, Mater. Sci. Eng. A. 278 (1999) 106–112. doi:10.1016/S0921-5093(99)00590-0.

[228] M. Eggersmann, H. Mehrer, Diffusion in intermetallic phases of the Fe-Al system, Philos. Mag. A. 80 (2000) 1219–1244.

[229] V. Knezevic, G. Sauthoff, J. Vilk, G. Inden, A. Schneider, R. Agamennone, et al., Martensitic/Ferritic Super Heat-resistant 650°C Steels - Design and Testing of Model Alloys, ISIJ Int. 42 (2002) 1505–1514. doi:10.2355/isijinternational.42.1505.

[230] D.G. Morris, I. Gutierrez-Urrutia, M.A. Muñoz-Morris, High temperature creep behaviour of an FeAl intermetallic strengthened by nanoscale oxide particles, Int. J. Plast. 24 (2008) 1205–1223. doi:16/j.ijplas.2007.09.001.

[231] D.G. Morris, M.A. Muñoz-Morris, Development of creep-resistant iron aluminides, Mater. Sci. Eng. A. 462 (2007) 45–52. doi:10.1016/j.msea.2005.10.083.

[232] D.G. Morris, M.A. Muñoz-Morris, L.M. Requejo, C. Baudin, Strengthening at high temperatures by precipitates in Fe–Al–Nb alloys, Intermetallics. 14 (2006) 1204–1207. doi:10.1016/j.intermet.2005.10.015.

[233] R.W. Cahn, How does long-range order affect creep of alloys?, Mater. Sci. Eng. A. 324 (2002) 1–4. doi:10.1016/S0921-5093(01)01273-4.

[234] H.C. Akuezue, D.P. Whittle, Interdiffusion in Fe–Al system: aluminizing, Met. Sci. 17 (1983) 27–31. doi:10.1179/msc.1983.17.1.27.

[235] I. Akimova, V. Mironov, A. Pokoyev, Aluminum Diffusion in Iron, Fiz. Met. Metalloved. 56 (1983) 1225–1227.

[236] D.G. Morris, M. Leboeuf, S. Gunther, M. Nazmy, Disordering behaviour of alloys based on Fe3Al, Philos. Mag. A. 70 (1994) 1067. doi:10.1080/01418619408242950.

[237] K. Hilfrich, W. Petry, O. Schärpf, E. Nembach, Phase diagram, superlattices and antiphase domains of Fe3Alx, $0.75 \leqslant x \leqslant 1.3$, investigated by neutron scattering, Acta Metall. Mater. 42 (1994) 731–741. doi:10.1016/0956-7151(94)90270-4.

[238] K. Hilfrich, T. Ebel, W. Petry, O. Schärpf, E. Nembach, Order in iron − 30 at.% aluminium investigated by neutron scattering, Scr. Metall. Mater. 25 (1991) 1857–1862. doi:10.1016/0956-716X(91)90317-T.

[239] M. Herman, N. Brown, Influence of Order-Disorder on Creep of Beta Brass, Trans. Am. Inst. Min. Metall. Eng. 206 (1956) 604–606.

[240] N.S. Stoloff, R.G. Davies, The plastic deformation of ordered FeCo and Fe3Al alloys, Acta Metall. 12 (1964) 473–485. doi:10.1016/0001-6160(64)90019-7.

[241] J.H. Westbrook, R.L. Fleischer, Intermetallic Compounds: Principles, Wiley, 1995.

[242] J. Alejandro, M. Wagner, T. Wolf, R. Volkmann, M. Heilmaier, D. Janda, et al., Exhaust gas traversed by component, preferably housing or exhaust gas circulating component, which is positioned within exhaust gas stream, preferably exhaust gas turbocharger, and is partially prepared from alloy comprising e.g. aluminum, DE102011110484 A1, 2013.

[243] J. Alejandro, M. Wagner, T. Wolf, R. Volkmann, M. Heilmaier, D. Janda, et al., Exhaust gas flow component, preferably housing, which is positioned within e.g. exhaust gas turbocharger and partly made of alloy comprising aluminum, boron, carbon, niobium, zirconium, titanium, tungsten, tantalum, silicon and vanadium, DE102011110481 A1, 2013.

[244] J. Alejandro, M. Wagner, T. Wolf, R. Volkmann, M. Heilmaier, D. Janda, et al., Abgasumströmtes Bauteil oder frischluftbeaufschlagtes Bauteil, teilweise aus einer Legierung hergestellt sowie Verwendung einer Legierung zur Herstellung eines solchen Bauteils, DE102011110482 A1, 2013.

Danksagung

Mein Dank gilt in erster Linie Prof. Dr. Martin Heilmaier für die fachliche Betreuung und Unterstützung während meiner Zeit als Doktorand. Er gab mir viel Freiraum, damit ich meine eigenen Ideen entwickeln konnte, um diese anschließend ausgiebig mit mir zu diskutieren und mir dadurch vermittelte, was es bedeutet wissenschaftlich zu arbeiten. Gleichzeitig gab er mir aber auch stets eine Richtung vor, die mir eine wichtige Orientierung und Halt bei meiner Arbeit gab.

Prof. Dr. Sharvan Kumar möchte ich für seine Arbeit als Zweitgutachter danken. Des Weiteren danke ich ihm für sein reges Interesse an meiner Arbeit und dafür, dass er sich sehr viel Zeit genommen hat, um mich während meines Forschungsaufenthaltes in seiner Arbeitsgruppe zu unterstützen.

Dem Bundesministerium für Wirtschaft und Technologie (BMWi) möchte ich für die Förderung unter dem Förderkennzeichen KF2593003CK0 danken sowie allen beteiligten Projektpartnern.

Für die Unterstützung meiner Kollegen am IAM-WK (insbesondere der physikalischen Metallkunde), INT (Abteilung für Elektronenmikroskopie und Spektroskopie) sowie meiner ehemaligen Kollegen von der TU Darmstadt aus der Abteilung „Physikalische Metallkunde“ möchte ich mich bedanken. Es war eine schöne Zeit, die wir gemeinsam verbracht haben.

Danken möchte ich auch allen Studenten (Katrin Barth, Ralph Dachauer, Anke Scherf, Markus Schulze, Jari Uhde), die im Laufe ihres Studiums in Form von Abschlussarbeiten, Praktika oder Hiwi-Tätigkeiten zu meiner Doktorarbeit beigetragen haben.

Es gibt zahlreiche Menschen, die ich außerhalb der Universität kennengelernt habe und die mir, sei es durch Diskussionen oder Messungen, geholfen haben. Auch diesen Personen gilt mein Dank. Insbesondere möchte ich mich bei Dr. Palm und Dr. Stein vom MPIE, Dr. Galetz von der Dechema und Dr. Hockauf (damals noch bei der TU Chemnitz) bedanken.

Last but not least möchte ich mich bei meiner Familie bedanken, auf die ich immer zählen kann.